

THESIS

GALAXY-DARK MATTER STRUCTURE RELATIONS
IN THE STANDARD COSMOLOGICAL MODEL

SHOGO MASAKI

*Division of Particle and Astrophysical Science
Graduate School of Science
Nagoya University*

MARCH, 2013

Dedicated to My Dear Mother with Sincere Gratitude

Abstract

Recent galaxy redshift surveys have provided us with large data of the galaxy distribution in the Universe. Such data enables us to measure various statistics including two-point statistics even for subsamples of galaxies classified by galactic properties. The observational results give us valuable clues to unveil galaxy formation and evolution through the cosmic time. Also the underlying dark matter distribution which contains wealth of cosmological information can be inferred from the observed galaxy distribution in the large-scale. Together with other cosmological observations, e.g., the cosmic microwave background measurements and the supernovae surveys, we can put tight constraints on cosmological parameters and make the the Λ -dominated, cold dark matter (Λ CDM) cosmological model more precise. Thus the galaxy redshift surveys play an important role in the field of cosmology.

The well-established Λ CDM model gives us a clear way to generate initial conditions of the dark matter (DM) distribution at sufficiently early epochs of the Universe. Using numerical simulations based on the Λ CDM cosmology, we can predict evolution of the DM distribution and properties of DM structures which are called halos and believed to host galaxies in the real Universe. However the relationships between the real galaxies and the simulated DM structures are still unclear and stand as a major uncertainty for cosmological interpretation of galaxy clustering measurements. To make use of the full potential of current data and larger data from upcoming deeper and wider-area surveys, it is clearly required to model the galaxy-halo connection accurately. Simultaneously, examining the galaxy-dark matter halo connection would be a key to explore the galaxy formation and evolution history since observed *snapshots* of the galaxy distribution in different epochs can be connected within the cosmological simulations.

This thesis is aimed at studying the relationships between the real galaxies and the simulated DM distribution and halos in the standard Λ CDM cosmological model. In the first part (chapters 2 and 3), we address the distribution of material around galaxies. We show that the Λ CDM model based-cosmological simulations well recover an observed average mass distribution around galaxies obtained through the gravitational lensing technique. We further employ simulation data to explore the mass distribution beyond the halos' virial radius and show DM halos do not have definite edges. We also study amount of mass beyond the virial radius of galactic halos to discuss the “missing dark matter problem”. And then, we extend the discussion for the mass distribution to the dust distribution. We develop a simple

analytic model for the dust density profile and the halo-dust mass ratio. We also develop a formulation to calculate the galaxy-dust cross correlation functions. We employ a fitting parameter which denotes the extent of dust around galaxies in the model dust density profile. By fitting the model predictions to the observed dust distribution around galaxies obtained through background quasar reddening, it is suggested that the dust extent around galaxies reaches up to a few times of the typical galactic halo virial radius.

In the latter part of this thesis (chapters 4 and 5), we examine methods to create realistic mock catalogs of galaxies. First, we develop a method to assign galaxy color to simulated DM halos in addition to luminosity using high-resolution cosmological simulations. We discuss what halo property can be a proxy for galaxy color. We rank halos by such proxy property to divide a halo catalog into two groups which correspond to red and blue galaxy samples, respectively. We compare the model predictions for color dependences of the two-point correlation functions and the galaxy-mass cross correlation functions with the observational results. We show that a model with the local DM density around halos is able to well reproduce both of the measurements simultaneously. Second, we develop a method to create a mock catalog of a particular type of galaxies, luminous red galaxies (LRGs), using large cosmological simulations. Based on the observational fact that LRGs are massive and passively evolving populations, we select most massive halos as progenitors of LRG-host halos at an earlier epoch than the epoch they are observed today. We track the assembly histories of the progenitor halos and define their descendants at the observed epoch of LRGs as the LRG-host halos. We show that our mock catalogs well recover various observed statistics of LRGs including clustering measurements. Using the mock catalogs, we also study the spatial and velocity distribution of satellite LRGs in their parent halos and discuss implications for cosmological interpretation of LRGs clustering measurements.

Contents

1	Introduction	7
1.1	The Friedmann universe	7
1.2	Cosmological parameters	9
1.3	Equation of state and time evolution	10
1.4	Linear perturbation theory	11
1.5	Two-point statistics	12
1.5.1	Two-point correlation functions	12
1.5.2	Power spectra	13
1.5.3	Initial condition, time evolution and normalization	13
1.6	Dark matter structure	14
1.6.1	Spherical collapse	15
1.6.2	The Press-Schechter formalism for the halo mass function	16
1.6.3	Cosmological N -body simulations and dark matter halos	18
1.7	Gravitational lensing	22
1.7.1	The lensing geometry and the deflection angle	22
1.7.2	The lens equation	24
1.7.3	Convergence, shear and magnification	24
1.8	Phenomenological methods for the galaxy-dark matter halo connections	26
1.9	Outline	27
2	Distribution of Mass around Galaxies	29
2.1	Introduction	29
2.2	Method	31
2.2.1	Cosmological N -body simulations	31
2.2.2	Halo identification	31
2.3	Mean surface density profiles around halos	33
2.3.1	Comparisons with MSFR	33
2.3.2	The effect of the mass range	35
2.3.3	NFW vs. SIS	38
2.4	Mass distribution beyond the virial radius	40
2.5	Summary	44

3	Distribution of Dust around Galaxies	45
3.1	Introduction	45
3.2	The model	46
3.2.1	Halo approach	46
3.2.2	Dust distribution profile	47
3.3	Results	52
3.4	Summary and discussion	54
4	Modeling Color-Dependent Galaxy Clustering	57
4.1	Introduction	57
4.2	Setup	59
4.2.1	Cosmological N -body simulations	59
4.2.2	Identification of halos, tracking assembly history and construction of subhalo catalog	60
4.2.3	Application of SHAM	60
4.3	Method for color assignment	62
4.3.1	Models for a proxy of galaxy color	62
4.4	Results	65
4.4.1	Color dependence of projected correlation functions	65
4.4.2	Color dependence of lensing profile	71
4.5	Summary and discussion	77
5	Understanding the Nature of Luminous Red Galaxies	79
5.1	Introduction	79
5.2	Methods	81
5.2.1	Cosmological N -body simulations	81
5.2.2	Mock catalogs of LRGs: connecting halos at $z = 2$ to central and satellite subhalos at $z = 0.3$	82
5.3	Results: comparisons with the SDSS LRG measurements	87
5.3.1	Halo occupation distribution	87
5.3.2	Projected correlation function	89
5.3.3	LRG-galaxy weak lensing	91
5.4	Properties of satellite LRGs and the FoG effect	94
5.4.1	Redshift-space power spectrum of LRGs	101
5.5	Discussion and conclusion	104
6	Concluding Remarks	109
6.1	Summary	109
6.2	Future prospects	110
	Acknowledgement	113

Chapter 1

Introduction

1.1 The Friedmann universe

The most important force in cosmology should be a long-range force, i.e., gravity, since not only the Universe itself but also its main components such as galaxies and galaxy clusters are simply huge objects. It means that, to describe an expanding universe, one needs to introduce general relativity. The electromagnetic force, of course, is a long-range force. However we expect the gravity plays a dominant role in cosmology since the electromagnetic charge would be neutral in sufficiently large scales.

First, we assume the so-called cosmological principle, *the Universe is homogeneous and isotropic at very large scales*. The isotropy principle can be justified with observations, such as the isotropy of the cosmic microwave background (CMB, see Figure 1.1¹) and the galaxy distribution in very large scales. In principle, the homogeneity cannot be verified observationally. The homogeneity can be taken by urging not only us but also observers at all the other places in the Universe to have isotropy.

Using the spherical coordinate of (ct, r, θ, ϕ) , the metric of space-time, which satisfies the cosmological principle, is given as

$$ds^2 = g_{\mu\nu} dx^\mu dx^\nu = -c^2 dt^2 + a^2(t) \left[\frac{dr^2}{1 - Kr^2} + r^2(d\theta^2 + \sin^2 \theta d\phi^2) \right], \quad (1.1)$$

$$g_{\mu\nu} = \begin{pmatrix} -1 & 0 & 0 & 0 \\ 0 & \frac{a^2(t)}{1-Kr^2} & 0 & 0 \\ 0 & 0 & a^2(t)r^2 & 0 \\ 0 & 0 & 0 & a^2(t)r^2 \sin^2 \theta \end{pmatrix}, \quad (1.2)$$

where $g_{\mu\nu}$ is the metric tensor, c is the speed of light, $a(t)$ is the scale factor and K is the curvature of the Universe. The metric is called as the Friedmann-Lemaître-Robertson-Walker (FLRW) metric. The scale factor is normalized to be unity $a(t) =$

¹This figure is taken from <http://map.gsfc.nasa.gov/>.

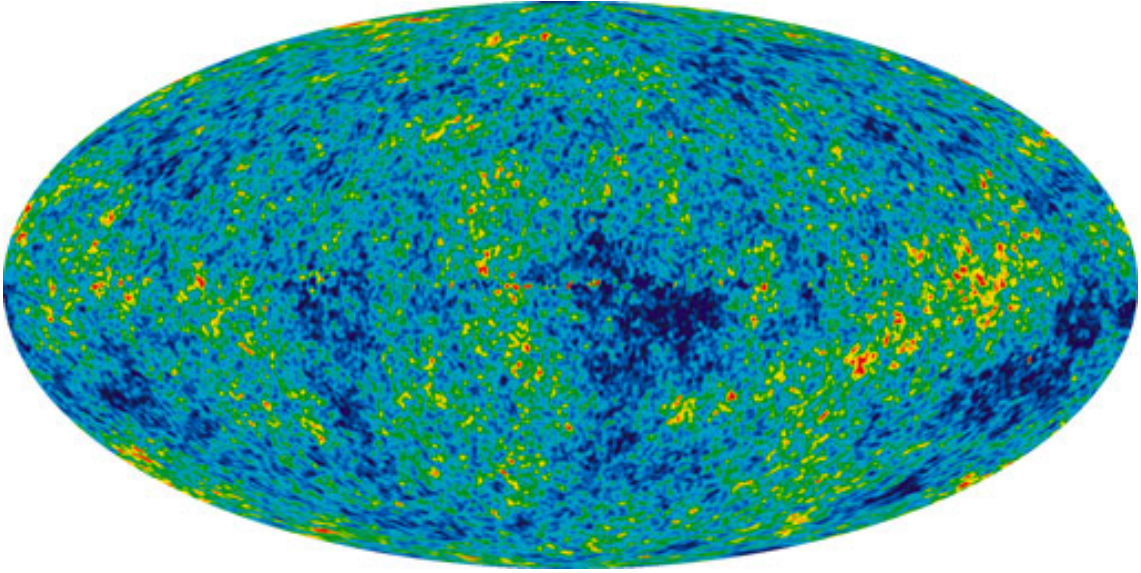


Figure 1.1: The all-sky CMB map from the seven-year results of *Wilkinson Microwave Anisotropy Probe* (WMAP). The color scale stands for deviations from the average temperature of 2.7 K. The amplitude of deviations is up to order of 10^{-4} K. Hence it can be said that CMB is almost isotropic.

1 at the present time. The sign of the curvature K corresponds to the geometry of the Universe as $K < 0$: open, $K = 0$: flat and $K > 0$: closed.

The Einstein equation

$$G_{\mu\nu} \equiv R_{\mu\nu} - \frac{1}{2}g_{\mu\nu}R = \frac{8\pi G}{c^4}T_{\mu\nu} + \Lambda\delta_{\mu\nu} \quad (1.3)$$

describes the evolution of the Universe, where $G_{\mu\nu}$ is the Einstein tensor, $R_{\mu\nu}$ is the Ricci tensor, R is the Ricci scalar, $T_{\mu\nu}$ is the energy-momentum tensor, Λ is assumed to be the cosmological constant and G is the gravitational constant. The Einstein equation relates the structure of the space-time in the left hand side to the energy content in the Universe in the right hand side.

The energy-momentum tensor of a perfect fluid is given as

$$T^\mu{}_\nu = \begin{pmatrix} -\rho & 0 & 0 & 0 \\ 0 & p & 0 & 0 \\ 0 & 0 & p & 0 \\ 0 & 0 & 0 & p \end{pmatrix}, \quad (1.4)$$

where ρ is the energy density and p is the pressure. Substituting the FLRW metric

tensor into the Einstein equation, we have

$$\left(\frac{\dot{a}}{a}\right)^2 = \frac{8\pi G}{3c^2}\rho - \frac{c^2 K}{a^2} + \frac{c^2 \Lambda}{3}, \quad (1.5)$$

$$\frac{\ddot{a}}{a} = -\frac{4\pi G}{3c^2}(\rho + 3p) + \frac{c^2 \Lambda}{3}, \quad (1.6)$$

where $\dot{a} = da/dt$ and $\ddot{a} = d^2a/dt^2$. Equation (1.5) is called the Friedmann equation.

In addition, from the conservation law, we have

$$\dot{\rho} + 3\frac{\dot{a}}{a}(\rho + p) = 0. \quad (1.7)$$

Together with the equation of state $p = p(\rho)$, one can describe the time evolution of the energy density.

1.2 Cosmological parameters

For given two positions, the comoving distance r and the physical distance x are related to each other with the scale factor $a(t)$ at that time as

$$x = a(t)r, \quad (1.8)$$

i.e., $r = x$ at the present time. The physical relative velocity of the two points due to the expansion of an Universe is

$$v = \frac{dx}{dt} = \frac{da}{dt}r = \frac{\dot{a}}{a}x. \quad (1.9)$$

This equation is simply the Hubble law at the present time. Hence the Hubble constant $H(t)$ at the arbitrary time t can be defined as

$$H(t) \equiv \frac{\dot{a}(t)}{a(t)}. \quad (1.10)$$

In particular, the value at the present time $t = t_0$ is expressed with the non-dimensional parameter h as

$$H(t = t_0) \equiv H_0 = 100h \text{ km s}^{-1} \text{ Mpc}^{-1}. \quad (1.11)$$

Then the Friedmann equation is expressed as

$$H^2 = \frac{8\pi G}{3c^2}\rho - \frac{c^2 K}{a^2} + \frac{c^2 \Lambda}{3}. \quad (1.12)$$

The critical density

$$\rho_{\text{cr}} = \frac{3c^2 H^2}{8\pi G} \quad (1.13)$$

corresponds to the density of a flat Universe with $\Lambda = 0$. The non-dimensional density parameter is defined to be the ratio of ρ to ρ_{cr} as

$$\Omega \equiv \frac{\rho}{\rho_{\text{cr}}} = \frac{\rho}{3c^2 H^2 / 8\pi G}. \quad (1.14)$$

In a similar manner, the parameter for the curvature and the cosmological constant are

$$\Omega_K \equiv -\frac{c^2 K}{a^2 H^2}, \quad \Omega_\Lambda \equiv \frac{c^2 \Lambda}{3H^2}. \quad (1.15)$$

With these three parameters, the Friedmann equation is reduced as

$$1 = \Omega + \Omega_K + \Omega_\Lambda. \quad (1.16)$$

1.3 Equation of state and time evolution

Non-relativistic matter (*matter*, e.g., cold dark matter and baryon) satisfies $p \ll \rho c^2$. Therefore the equation of state for matter is $p = 0$. Then Equation (1.7) leads

$$\rho_{\text{m}} \propto 1/a^3. \quad (1.17)$$

This means that the number density of matter decreases as $1/\text{Volume}$ due to expansion of the universe.

Relativistic matter (*radiation*, e.g., CMB photon) has kinetic energy much higher than rest mass energy. The equation of state for radiation is $p = \rho/3$. Hence Equation (1.7) leads

$$\rho_{\text{r}} \propto 1/a^4. \quad (1.18)$$

The scale factor dependence is steeper than matter. The extra power of -1 means that radiation lose its energy as wave length becomes longer due to expansion of the Universe.

Here we define the density parameters for matter and radiation as

$$\Omega_{\text{m}} \equiv \frac{\rho_{\text{m}}}{\rho_{\text{cr}}}, \quad \Omega_{\text{r}} \equiv \frac{\rho_{\text{r}}}{\rho_{\text{cr}}}. \quad (1.19)$$

The Friedmann equation can be rewritten as

$$H^2(a) = H_0^2 \left(\frac{\Omega_{\text{m}0}}{a^3} + \frac{\Omega_{\text{r}0}}{a^4} - \frac{\Omega_{K0}}{a^2} + \Omega_{\Lambda 0} \right), \quad (1.20)$$

$$\dot{a}^2(t) = H_0^2 \left(\frac{\Omega_{\text{m}0}}{a} + \frac{\Omega_{\text{r}0}}{a^2} - \Omega_{K0} + \Omega_{\Lambda 0} a^2 \right), \quad (1.21)$$

where the subscript notation of 0 denotes the values at the present time. Hence we can describe the expansion of the Universe with the density parameters at the present time. Also Equation (1.21) means that the Universe is dominated by radiation

component in the early Universe and by pressure-less matter in the local Universe.

Although we used a variable t and the scale factor $a(t)$ as proxies for cosmic time so far, redshift z of light emitted by an object is convenient to know when the object emitted or *how far the object exists from us*. Due to expansion of the Universe, the wave length of light from an object is stretched between the object and us. Considering the null geodesic, we obtain

$$\frac{a(t = t_{\text{obs}} = t_0)}{a(t_{\text{emit}})} = \frac{1}{a(t_{\text{emit}})} = \frac{\lambda_{\text{obs}}}{\lambda_{\text{emit}}} \equiv 1 + z, \quad (1.22)$$

where t_{emit} is the time when the object emitted, $a(t_{\text{emit}})$ is the scale factor at that time. λ_{emit} and λ_{obs} are the wave lengths at the emission time and the observation time, i.e., the present time, respectively.

1.4 Linear perturbation theory

So far we have seen the evolution of the *smooth* universe. However today we can see rich structures such as galaxies, galaxy clusters and the large-scale structure in the Universe. In the paradigm of the CDM cosmologies, the structures are believed to be formed through assembly of material, the so-called hierarchical clustering structure formation.

The seed of today's large-scale structure of the Universe is the tiny matter density fluctuations. We introduce the density fluctuation δ as

$$\delta(t, \mathbf{r}) = \frac{\rho(t, \mathbf{r})}{\bar{\rho}(t)} - 1 \quad (1.23)$$

where \mathbf{r} is the comoving coordinate and $\bar{\rho}$ is the mean density of the Universe at the time t . Using the comoving coordinate, a pressure-less fluid obeys following three equations,

$$\frac{\partial \rho}{\partial t} + 3\frac{\dot{a}}{a}\rho + \frac{1}{a}\nabla_r \cdot (\rho \mathbf{u}) = 0 \quad : \quad \text{continuity Eq.} \quad (1.24)$$

$$\frac{\partial \mathbf{u}}{\partial t} + \frac{1}{a}(\mathbf{u} \cdot \nabla_r)\mathbf{u} + \frac{\dot{a}}{a}\mathbf{u} = -\frac{1}{a}\nabla_r \Phi_r \quad : \quad \text{Euler Eq.} \quad (1.25)$$

$$\nabla_r^2 \Phi_r = 4\pi G a^2 \rho \quad : \quad \text{Poisson Eq.} \quad (1.26)$$

where Φ_r is the gravitational potential and $\mathbf{u} = a\dot{\mathbf{r}}$ is the peculiar velocity.

Considering the very tiny fluctuation $\delta \ll 1$, we linearize the above three equations by neglecting the second order of δ and u . From the three linear equations, we obtain

$$\ddot{\delta} + 2\frac{\dot{a}}{a}\dot{\delta} = 4\pi G \bar{\rho}(t)\delta. \quad (1.27)$$

This equation can be regarded as the equation of motion of the density fluctuation: The Hubble expansion \dot{a}/a is the friction term and the gravitational force is the

source term. Since this equation does not contain the spatial derivative, the solution can be decomposed into the spatial and time dependent component as

$$\delta(t, \mathbf{r}) = D(t)\delta(\mathbf{r}). \quad (1.28)$$

Of course, the growth factor $D(t)$ follows the equation of motion. The special solutions of $D(t)$ are

$$D_+(a) \propto H(a) \int_0^a \frac{da'}{a'^3 H(a')^3}, \quad D_-(a) \propto H(a), \quad (1.29)$$

these are called the growing mode and the decaying mode, respectively.

As we have seen here, the tiny fluctuations in the early Universe have grown up to the present structures through the gravitational instability.

1.5 Two-point statistics

In cosmology and extra galactic astrophysics, two-point statistics are one of the most familiar and important measurements to characterize the large-scale distribution of matter, galaxies and so on.

1.5.1 Two-point correlation functions

We consider two points \mathbf{r}_1 and \mathbf{r}_2 with the density fluctuations δ_1 and δ_2 , respectively. Correlation of the two points can be characterized by the product $\delta_1\delta_2$. In a represented volume, therefore, the two-point correlation function ξ is defined as

$$\xi(r_{12}) \equiv \langle \delta(\mathbf{r}_1)\delta(\mathbf{r}_2) \rangle, \quad (1.30)$$

where $r_{12} = |\mathbf{r}_1 - \mathbf{r}_2|$ and $\langle \rangle$ denotes the ensemble averaging in the represented volume. Using $\delta(\mathbf{r}) = \rho(\mathbf{r})/\bar{\rho} - 1$, ξ is related to the density field as

$$\langle \rho(\mathbf{r}_1)\rho(\mathbf{r}_2) \rangle = \bar{\rho}^2[1 + \xi(r_{12})]. \quad (1.31)$$

If the density field is random, the ensemble average in the left hand side should be $\bar{\rho}^2$. Hence the two-point correlation function ξ stands for the scale dependence of deviation from the random density field.

In the case that we treat a discrete density field, such as galaxy distribution, rather than a continuous field, the two-point correlation functions can be obtained from the pair number counting. One can easily count the number of galaxies $dN(r)$ within $\mathbf{r} \sim \mathbf{r} + d\mathbf{r}$ from a galaxy, where $r = |\mathbf{r}|$. Repeating this procedure for all galaxies, the average number of galaxies $\bar{dN}(r)$ is obtained. \bar{dN} is related to the

two-point correlation function as

$$d\bar{N}(r) = 4\pi\bar{n}r^2dr[1 + \xi(r)], \quad (1.32)$$

where \bar{n} is the number density of galaxies in the represented volume.

1.5.2 Power spectra

Power spectra describe the two-point statistics of fluctuations in the Fourier space while the two-point correlation functions are in the real space. The density fluctuation $\delta(\mathbf{r})$ is Fourier transformed as

$$\tilde{\delta}(\mathbf{k}) = \int d^3r \exp(-i\mathbf{k} \cdot \mathbf{r})\delta(\mathbf{r}). \quad (1.33)$$

In a similar way of the two-point correlation functions, the correlation in the Fourier space is defined as

$$\langle \tilde{\delta}(\mathbf{k})\tilde{\delta}^*(\mathbf{k}') \rangle = \int d^3r_1 d^3r_2 \exp(-i\mathbf{k} \cdot \mathbf{r}_1 + i\mathbf{k}' \cdot \mathbf{r}_2)\xi(r_{12}). \quad (1.34)$$

Having $\mathbf{r}_1 = \mathbf{r} + \mathbf{r}_2$ and the Dirac delta function δ_D , we define the power spectrum $P(k)$ as

$$\langle \tilde{\delta}(\mathbf{k})\tilde{\delta}^*(\mathbf{k}') \rangle = (2\pi)^3 \delta_D(\mathbf{k} - \mathbf{k}') \int d^3r \exp(-i\mathbf{k}' \cdot \mathbf{r})\xi(r) \quad (1.35)$$

$$\equiv (2\pi)^3 \delta_D(\mathbf{k} - \mathbf{k}')P(k). \quad (1.36)$$

Power spectra and two-point correlation functions can be related through as following

$$P(k) = 4\pi \int_0^\infty dr r^2 \xi(r) \frac{\sin(kr)}{kr}, \quad \xi(r) = \int_0^\infty dk \frac{k^2}{2\pi^2} P(k) \frac{\sin(kr)}{kr}. \quad (1.37)$$

1.5.3 Initial condition, time evolution and normalization

Assuming that there are no typical scale in the sufficiently early Universe, the power spectrum should have a power-law form

$$P_{\text{init}}(k) = A_{\text{init}} k^{n_s}, \quad (1.38)$$

where the spectral index n_s is one of the most important cosmological parameters.

While the growth of the fluctuations in the matter-dominated era is described by the growth factor, the fluctuations that enter the horizon in the radiation-dominated era grow depending on the wave number k . The dependence is described with the

transfer function $T(k)$ as

$$\tilde{\delta}(k, t) = T(k, t) \frac{D_+(t)}{D_{\text{init}}} \tilde{\delta}_{\text{init}}(k). \quad (1.39)$$

Then the power spectrum at the time t is related with the initial spectrum via the transfer function as

$$P(k, t) = T^2(k, t) \frac{D_+^2(t)}{D_{\text{init}}^2} P_{\text{init}}(k). \quad (1.40)$$

The commonly used quantity for the normalization of power spectra is σ_8 . This factor is defined as

$$\sigma_8 \equiv \int \frac{d^3k}{(2\pi)^3} P(k, t=0) \tilde{W}_k^2(R=8 h^{-1} \text{Mpc}) \quad (1.41)$$

$$= \int \frac{d^3k}{(2\pi)^3} A_{\text{init}} k^{n_s} T^2(k, t=0) \frac{D^2(t=0)}{D_{\text{init}}^2} \tilde{W}_k^2(R=8 h^{-1} \text{Mpc}), \quad (1.42)$$

where \tilde{W}_k is the window function in Fourier space. The top-hat windows in the real and Fourier spaces are given by

$$W(R) = \begin{cases} 1 & (r \leq R) \\ 0 & (r > R) \end{cases}, \quad (1.43)$$

$$\tilde{W}_k(R) = 4\pi R^3 \left[\frac{\sin(kR)}{(kR)^3} - \frac{\cos(kR)}{(kR)^2} \right]. \quad (1.44)$$

Therefore σ_8 is the variance of the present fluctuation smoothed in the sphere of $8 h^{-1} \text{Mpc}$ and related with A_{init} as

$$A_{\text{init}} = \frac{\sigma_8}{\int \frac{d^3k}{(2\pi)^3} k^{n_s} T_0^2(k) (D_0^2/D_{\text{init}}^2) \tilde{W}_k^2(R=8 h^{-1} \text{Mpc})}. \quad (1.45)$$

1.6 Dark matter structure

Nearly uniform distribution of matter in the early Universe as seen in the CMB map grows up to the large-scale structure in the Universe. Figure 1.2 shows not only filamentary structures but also voids in the galaxy distribution. Galaxies and galaxy clusters are believed to trace the underlying dark matter distribution and to be surrounded or *hosted* by the virialized dark matter objects, *halos*. To explore the connection between galaxies and halos, dark matter structures must be studied in details.

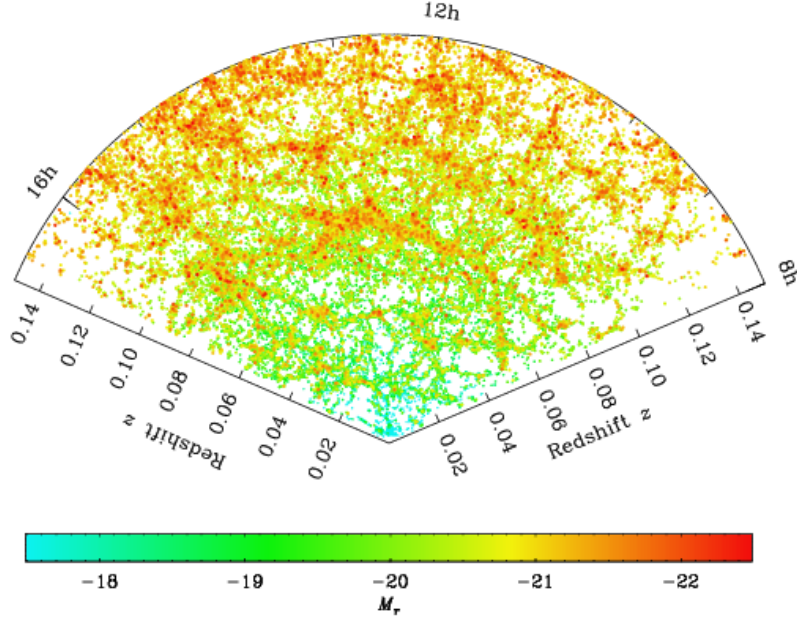


Figure 1.2: Galaxy distributions in the large-scale (Zehavi et al. 2011). This is a slice in the Sloan Digital Sky Survey (SDSS, York et al. 2000) main galaxy sample. The dots color-coded by absolute magnitude correspond to galaxies. Redder color denotes brighter galaxies.

1.6.1 Spherical collapse

We study the gravitational collapse of a spherical region with a radius of $r(t)$ and a total mass of M . The equation of motion and its time integration are given as

$$\frac{d^2r}{dt^2} = -\frac{GM}{r^2}, \quad \left(\frac{dr}{dt}\right)^2 = \frac{2GM}{r} + \text{const.} \quad (1.46)$$

We consider the case of the constant < 0 . The solution is expressed with a variable θ and a constant C as

$$r = \frac{GM}{C}(1 - \cos \theta), \quad t = \frac{GM}{C^{3/2}}(\theta - \sin \theta). \quad (1.47)$$

These solutions mean that the sphere reaches the maximum radius $r_{\text{max}} = 2GM/C$ at $\theta = \pi$ and $t \equiv t_{\text{ta}} = \pi GM/C^{3/2}$, and collapse at $\theta = 2\pi$ and $t \equiv t_{\text{coll}} = 2t_{\text{ta}} = 2\pi GM/C^{3/2}$.

The mean density of the sphere in the case of $\theta \ll 1$, i.e., $r \sim 0$, is

$$\rho(t) = \frac{3M}{4\pi r^3(t)} = \frac{1}{6\pi G t^2} \left[1 + \frac{3C}{20} \left(\frac{6t}{GM} \right)^{2/3} + \dots \right]. \quad (1.48)$$

In the case of $\Omega_m = 1$, $\Omega_K = 0$, the cosmic matter density $\bar{\rho}(t)$ is identical to

$1/6\pi Gt^2$. Hence the second term in the right hand side corresponds to the density fluctuation of the collapsed region:

$$\delta(t) = \frac{3C}{20} \left(\frac{6t}{GM} \right)^{2/3}. \quad (1.49)$$

At the collapse time t_{coll} , the density fluctuation is

$$\delta(t_{\text{coll}}) \equiv \delta_c = \frac{3}{20} (12\pi)^{2/3} \simeq 1.69. \quad (1.50)$$

From the energy conservation and the virial theorem as

$$\frac{1}{2} \left(\frac{dr}{dt} \right)^2 - \frac{GM}{r_{\text{vir}}} = -\frac{GM}{r_{\text{max}}}, \quad \left(\frac{dr}{dt} \right)^2 - \frac{GM}{r_{\text{vir}}} = 0, \quad (1.51)$$

the virial radius is obtained as $r_{\text{vir}} = r_{\text{max}}/2 = GM/C$. Assuming that the sphere is in the virial equilibrium at $\theta = 2\pi$ and $t = t_{\text{coll}}$, the density ratio between the background and the sphere is

$$\frac{\rho(t_{\text{coll}})}{\bar{\rho}(t_{\text{coll}})} = \frac{M/(4\pi r_{\text{vir}}^3/3)}{1/6\pi Gt_{\text{coll}}^2} = 18\pi^2 \simeq 178. \quad (1.52)$$

As we have seen here, the density fluctuation of the collapsed object is about 1.7 and the mean density is about 200 times higher than the background density. These values are very important and used commonly in the studies of structure formation.

1.6.2 The Press-Schechter formalism for the halo mass function

The halo mass function denotes the abundance of dark matter halos in the Universe as a function of the halo mass, and is very fundamental quantity. The halo mass function has been studied analytically and numerically.

The most important formalism was given by Press & Schechter (1974) and called as the PS formalism. The PS formalism begins with the random Gaussian field of density fluctuations. Let δ_R be the fluctuation smoothed in the sphere of R . The probability distribution function of δ_R is

$$p(\delta_R, t) = \frac{1}{\sqrt{2\pi}\sigma(R, t)} \exp \left[-\frac{\delta_R^2}{2\sigma^2(R, t)} \right], \quad (1.53)$$

where

$$\sigma^2(R, t) = \int \frac{d^3k}{(2\pi)^3} P(k, t) \tilde{W}_k^2(R). \quad (1.54)$$

The halo mass and the comoving smoothing scale are related with the present day average density $\bar{\rho}_0$ as $M = 4\pi\bar{\rho}_0 R^3/3$. The PS formalism assumes that the density

fluctuation above a threshold collapse. The threshold value at time is given as

$$\delta_c(t) \equiv \frac{\delta_c}{D(t)}. \quad (1.55)$$

From the integration of the above probability function in the range of $\delta_R > \delta_c(t)$, we obtain the PS halo mass function as

$$\frac{dn(M, t)}{dM} = \sqrt{\frac{2}{\pi}} \frac{\bar{\rho}_0}{M} \frac{\delta_c(t)}{\sigma^2(M)} \left| \frac{d\sigma(M)}{dM} \right| \exp \left[-\frac{\delta_c^2(t)}{2\sigma^2(M)} \right]. \quad (1.56)$$

Here the factor of two is multiplied under the assumption that all the matter is included in a halo. Hence given the present matter power spectrum $P(k)$, one can predict the halo mass function.

It is known that the PS halo mass function agrees with results from cosmological N -body simulations qualitatively well. A number of following works used larger simulations to get better agreements. For comparison between models, the following function is convenient (Jenkins et al. 2001)

$$f(\sigma) \equiv \frac{M}{\bar{\rho}(z)} \frac{dn(M, z)}{d \ln[\sigma^{-1}(M, z)]}. \quad (1.57)$$

For the PS halo mass function,

$$f_{\text{PS}}(\sigma, z) = \sqrt{\frac{2}{\pi}} \frac{\delta_c}{\sigma} \exp \left(-\frac{\delta_c^2}{2\sigma^2} \right). \quad (1.58)$$

Here we give a few examples of more sophisticated works:

- Sheth & Tormen (1999, ST):

$$f_{\text{ST}}(\sigma, z) = A \sqrt{\frac{2a}{\pi}} \left[1 + \left(\frac{\sigma^2}{a\delta_c^2} \right)^p \right] \frac{\delta_c}{\sigma} \exp \left(-\frac{a\delta_c^2}{2\sigma^2} \right),$$

with $A = 0.322$, $a = 0.707$, $p = 0.3$. (1.59)

- Crocce et al. (2010, MICE)

$$f_{\text{MICE}}(\sigma, z) = A(z) [\sigma^{-a(z)} + b(z)] \exp \left[-\frac{c(z)}{\sigma^2} \right],$$

with $A(z) = 0.58(1+z)^{-0.13}$, $a(z) = 1.37(1+z)^{-0.15}$,
 $b(z) = 0.3(1+z)^{-0.084}$, $c(z) = 1.036(1+z)^{-0.024}$. (1.60)

- Bhattacharya et al. (2011, Coyote)

$$\begin{aligned}
 f_{\text{Coyote}}(\sigma, z) &= \tilde{A}(z) \sqrt{\frac{2}{\pi}} \left[1 + \left\{ \frac{\sigma^2}{\tilde{a}(z)\delta_c^2} \right\}^{\tilde{p}} \right] \left[\frac{\delta_c \sqrt{\tilde{a}(z)}}{\sigma} \right]^{\tilde{q}} \exp \left[-\frac{\tilde{a}(z)\delta_c^2}{2\sigma^2} \right], \\
 \text{with } \tilde{A}(z) &= 0.333(1+z)^{-0.11}, \quad \tilde{a}(z) = 0.788(1+z)^{-0.01}, \\
 \tilde{p} &= 0.807, \quad \tilde{q} = 1.795.
 \end{aligned} \tag{1.61}$$

1.6.3 Cosmological N -body simulations and dark matter halos

In cosmological N -body simulations, the continuous matter distribution is replaced with a discrete particle distribution. Given one cosmological parameter set, initial conditions for simulations are generated at the sufficiently early epoch at which perturbation theories work well. The initial redshift should depend on the simulation specifications such as the box size the total number of employed particles and be chosen carefully (see e.g., Lukić et al. 2007). For thus generated discrete particle distribution, the gravitational many-body problem is solved by computing the Newtonian gravitational force numerically. In practice, the equation of motion of a particle is expressed as

$$\frac{d^2 \mathbf{x}_i}{dt^2} = \sum_{j \neq i}^N G m_j \frac{\mathbf{x}_j - \mathbf{x}_i}{(|\mathbf{x}_j - \mathbf{x}_i|^2 + \epsilon^2)^{3/2}}, \tag{1.62}$$

where ϵ is the so-called softening parameter which avoids the divergence of the gravitational force at $|\mathbf{x}_j - \mathbf{x}_i| \simeq 0$ and corresponds to the spatial resolution. Thanks to the increasing computer power, now we can carry out larger and finer simulations than before. Figure 1.3 shows the dark matter distribution taken from a cosmological N -body simulation². As well as the large-scale structure in the Universe as shown in Figure 1.2, filamentary structures and voids can be seen in the figure. Density peaks in filaments and their connections would be identified as halos.

Since the halo formation is a very non-linear phenomenon, cosmological N -body simulations are useful to study dark matter halo properties. Not only the mass function but also other properties including the bias factor, the density profile, the subhalo abundance and so on can be calibrated.

Halo identification and mass

Identification of halos in cosmological simulations is not a trivial task. There are some conventional methods. We give two examples of them. The first one is the friends-of-friends (FoF) algorithm (Davis et al. 1985). The FoF algorithm defines halos as structures whose particles are separated by distances less than a percolation

²The figure is taken from <http://www.ipmu.jp/node/1221>.

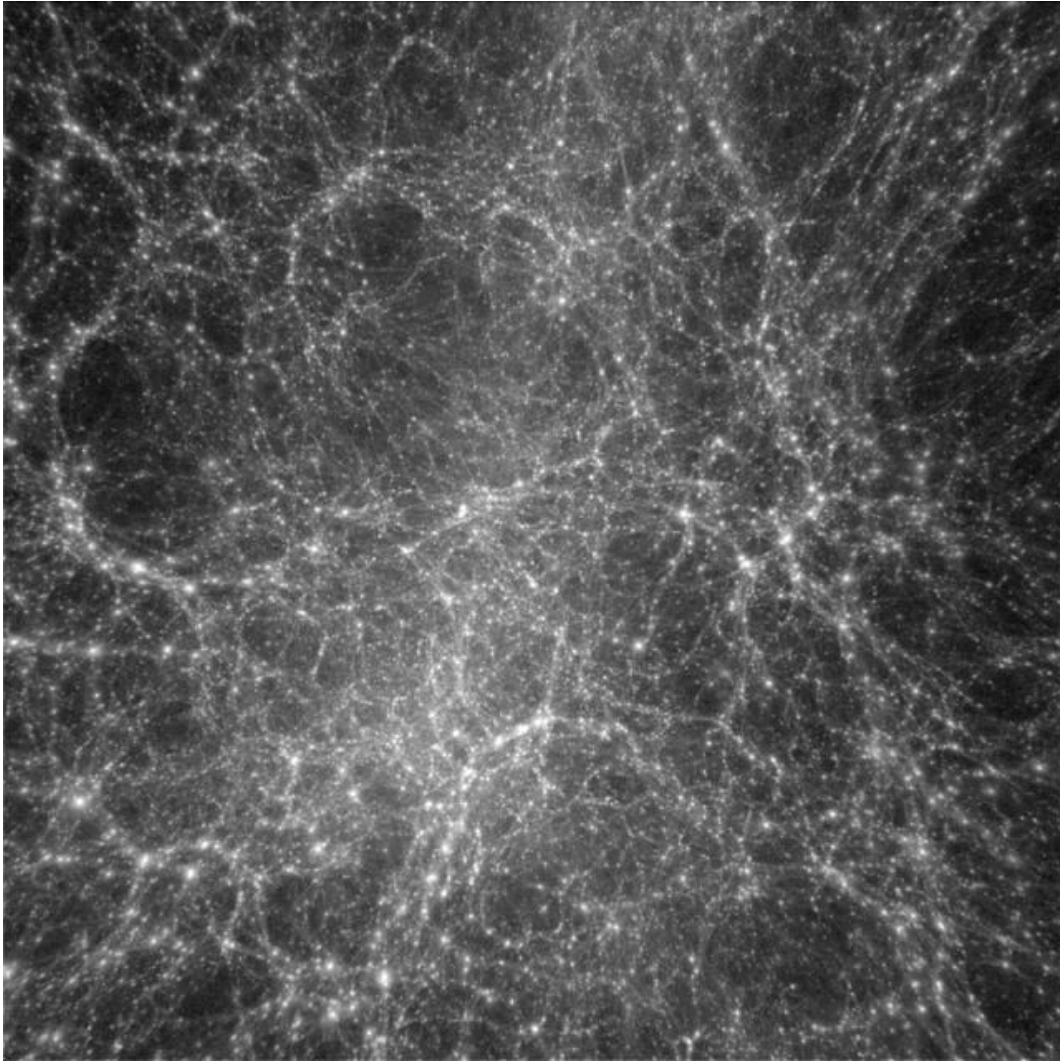


Figure 1.3: The dark matter distribution taken from a cosmological N -body simulation. The box size is about one hundred million light year on a side. The paler (deeper) color stands for the higher (lower) density regions.

parameter, the linking length b_{link} . A conventional value of the linking length b_{link} is 0.2 in units of the mean interparticle separation. If all particle separations in a structure is 0.2 in units of the mean interparticle separation, the mean density of the structure is about $0.2^{-3} = 125$ times higher than the background density. The advantage of the FoF is that the algorithm does not assume the priori shape of halos.

To estimate the size of halos, i.e., the virial radius, the spherical overdensity (SO) method is suitable rather than the FoF. As we have seen in Section 1.6.1, the mean density of the collapsed spherical region is about 200 times higher than the background density. Hence the SO defines halos as regions in which the mean internal density is Δ times higher than the background density or the critical density. The commonly used values for Δ are 200 and 180 (see Section 1.6.1). Also Bryan & Norman (1998) gave the fitting function of $\Delta = \Delta_{\text{vir}}$ for the arbitrary cosmology and redshift. The total mass and size of thus identified structure is called as the virial mass and radius.

Halo bias

Since dark halos are formed at peaks of the matter density field, the halo distribution is *biased* tracer of the matter distribution. The halo bias b is defined as

$$b \equiv \sqrt{\frac{\xi_{\text{halo}}}{\xi_{\text{matter}}}} \quad \text{or} \quad b \equiv \frac{\xi_{\text{halo-matter}}}{\xi_{\text{matter}}}, \quad (1.63)$$

where ξ_{halo} is the halo autocorrelation function, ξ_{matter} is the matter autocorrelation function and $\xi_{\text{halo-matter}}$ is the halo-matter cross correlation function. Equivalently, the galaxy bias can be defined in the same way. Simulation studies have shown that more massive, i.e., rarer, halos have larger bias than less massive ones. The halo bias depends on not only the halo mass but also other halo properties (see e.g., Gao et al. 2005; Gao & White 2007). Also the halo bias can have a scale dependence.

Density profile

How matter is distributed around galaxies is one of the fundamental questions in cosmology. Theoretical predictions can be made using cosmological N -body simulations. Navarro et al. (1997) advocated the so-called NFW profile which works well in the CDM cosmological models

$$\rho(r) \propto \frac{1}{(r/r_s)(1 + r/r_s)^2}, \quad (1.64)$$

where r_s is the scale length. The scale length r_s corresponds to the transition scale of the power of the profile. $c = R_{\text{vir}}/r_s$ is called the concentration parameter. The concentration parameter has a weak dependence on the halo mass and redshift. Duffy et al. (2008) presented a fitting function for halos identified using the Bryan

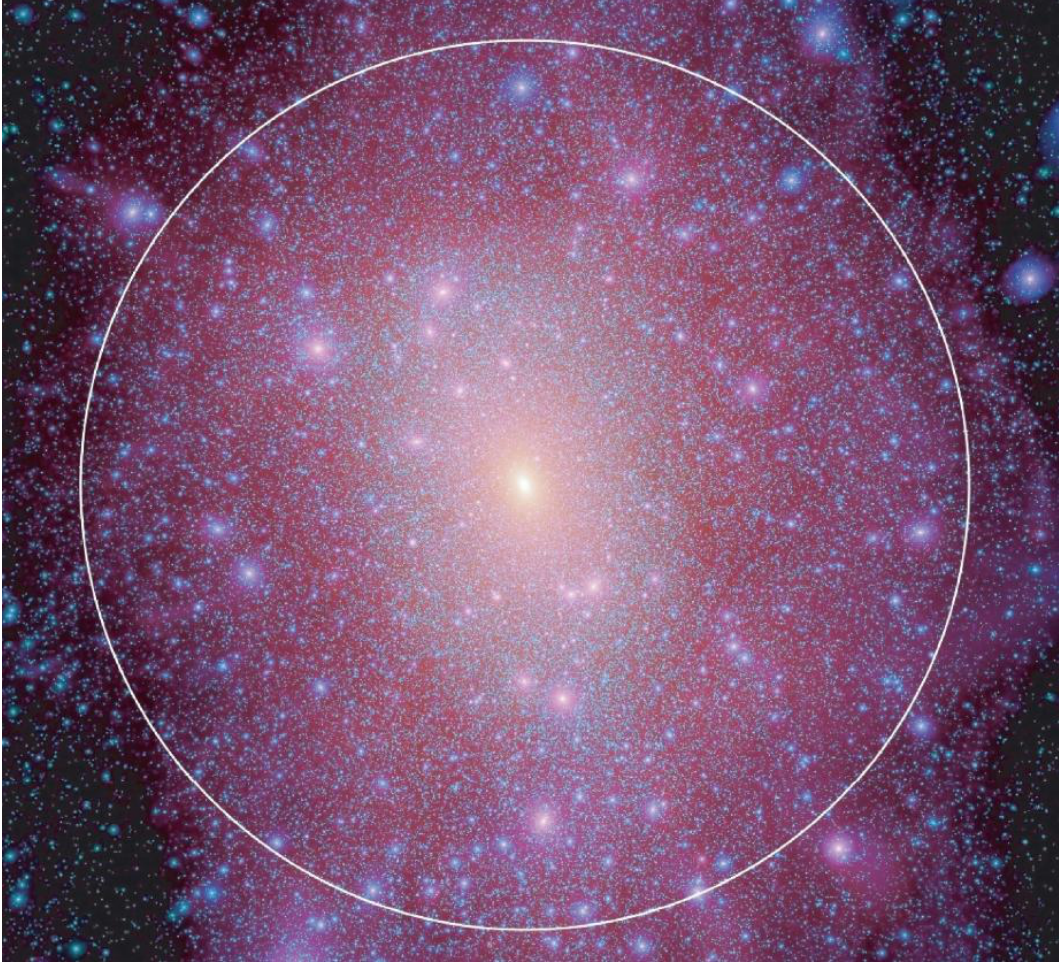


Figure 1.4: The dark matter distribution in and around a Milky Way sized halo (Springel et al. 2008). The circle is their definition for the virial radius of 433 kpc. The paler (deeper) color stands for the higher (lower) density regions.

& Norman (1998) overdensity as

$$c(M_{\text{vir}}, z) = 7.85[M_{\text{vir}}/(2 \times 10^{12} h^{-1} M_{\odot})]^{-0.081}(1+z)^{-0.71}. \quad (1.65)$$

Such fitting formulae are varied for the different halo definitions.

Subhalos in halos

In CDM cosmological models, structure formation proceeds hierarchically. Halos are the assembly of smaller structures. In such hierarchical process, although the building blocks are destroyed due to tidal stripping, their high density cores can remain in the more massive object as local dense clumps. The remnants in structure formation are called subhalos. Figure 1.4 shows the dark matter distribution in and around a Milky Way sized halo (Springel et al. 2008). We can see a number of dense clumps in and around the halo.

For comparison with the real structures, we can make the following two expectations. First, in galactic sized halos, subhalos correspond to dwarf galaxies. Second, in group or cluster sized halos, subhalos correspond to member galaxies. Moore et al. (1999) showed that the former expectation seems to be failed. It is known as the substructure problem and the challenge of the CDM cosmology in the small scale. While the failure of the former expectation, the latter seems works well. Hence to study the galaxy-halo connection, subhalos are a very important element as well as halos.

1.7 Gravitational lensing

In the previous subsection, we have seen that cosmological N -body simulations are a useful theoretical tool to investigate dark matter properties. Observationally, weak gravitational lensing is a powerful tool to explore the distribution of dark matter around galaxies (see Bartelmann & Schneider 2001, for a review). Since lensing is solely sensitive to the gravitational potential, we can *see* the dark matter distribution as well as baryons.

1.7.1 The lensing geometry and the deflection angle

Here we briefly review basics of gravitational lensing (see e.g., Miralda-Escude 1991; Narayan & Bartelmann 1996; Bartelmann & Schneider 2001). Figure 1.5 shows a schematic picture for gravitational lensing. In the figure, D_d , D_s and D_{ds} are angular diameter distances between the observer and the lens object, the observer and the source object, and the lens and the source, respectively. The lens and the source planes are perpendicular to the line-of-sight of the observer. θ and β denote angles between the lens center and the actually seen image, and the lens center and the source, respectively. Although the light path from the source to the observer would be deflected smoothly in reality, it can be approximated that deflection occurs discontinuity if the thickness of the lens is much smaller than D_d and D_s (the *thin lens* approximation). The deflection angle $\hat{\alpha}$ is defined as seen in the Figure 1.5. Also $\boldsymbol{\eta}$ is the position of the source in the source plane and $\boldsymbol{\xi}$ is the impact factor of the deflected light path in the lens plane.

The deflection angle induced by a point mass with mass of m is $\hat{\alpha} = 4Gm/c^2\xi$. Let the lens object be an object with an extended mass distribution with a density profile $\rho(\mathbf{r})$ rather than a point mass. The deflection angle is the linear combination of those induced by mass elements $dm(\mathbf{r}') = \rho(\mathbf{r}')dV'$ as

$$\hat{\alpha}(\boldsymbol{\xi}') = \frac{4G}{c^2} \int d^2\xi' dr'_3 \rho(\xi'_1, \xi'_2, r'_3) \frac{\boldsymbol{\xi} - \boldsymbol{\xi}'}{|\boldsymbol{\xi} - \boldsymbol{\xi}'|^2} \equiv \frac{4G}{c^2} \int d^2\xi' \Sigma(\boldsymbol{\xi}') \frac{\boldsymbol{\xi} - \boldsymbol{\xi}'}{|\boldsymbol{\xi} - \boldsymbol{\xi}'|^2}, \quad (1.66)$$

where $\mathbf{r} = (\xi_1, \xi_2, r_3)$ and r_3 is the line-of-sight direction. The surface mass density

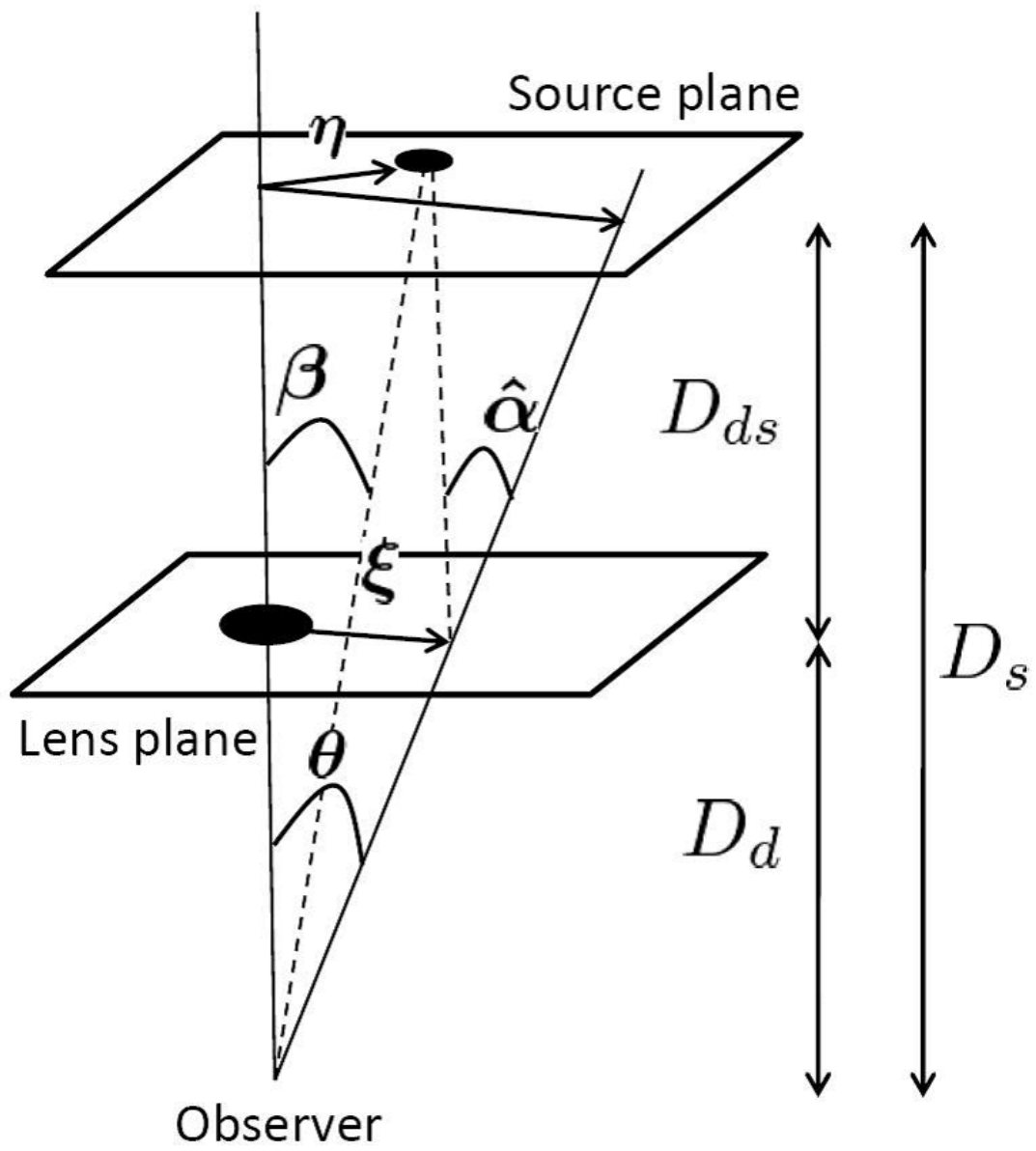


Figure 1.5: A schematic picture for the geometry of gravitational lensing.

profile Σ is defined as

$$\Sigma(\boldsymbol{\xi}) \equiv \int dr_3 \rho(\xi_1, \xi_2, r_3). \quad (1.67)$$

Therefore the deflection angle is determined with the projected density profile of the lens object under the thin lens approximation.

1.7.2 The lens equation

In Figure 1.5, the angles are related as

$$\boldsymbol{\eta} = \frac{D_s}{D_d} \boldsymbol{\xi} - D_{ds} \hat{\boldsymbol{\alpha}}(\boldsymbol{\xi}), \quad \boldsymbol{\eta} = D_s \boldsymbol{\beta} \quad \text{and} \quad \boldsymbol{\xi} = D_d \boldsymbol{\theta}. \quad (1.68)$$

Then we obtain the lens equation

$$\boldsymbol{\beta} = \boldsymbol{\theta} - \frac{D_{ds}}{D_s} \hat{\boldsymbol{\alpha}}(D_d \boldsymbol{\theta}) \equiv \boldsymbol{\theta} - \boldsymbol{\alpha}, \quad (1.69)$$

where the scaled deflection angle $\boldsymbol{\alpha}$ is defined as $\boldsymbol{\alpha} \equiv D_{ds} \hat{\boldsymbol{\alpha}}/D_s$. If more than one solution $\boldsymbol{\theta}$ can be found for a fixed $\boldsymbol{\beta}$, multiple images of the source are appeared.

From equation (1.66), the scaled deflection angle is rewritten as

$$\boldsymbol{\alpha}(\boldsymbol{\theta}) = \frac{1}{\pi} \int d^2 \theta' \kappa(\boldsymbol{\theta}') \frac{\boldsymbol{\theta} - \boldsymbol{\theta}'}{|\boldsymbol{\theta} - \boldsymbol{\theta}'|^2}, \quad (1.70)$$

where $\kappa(\boldsymbol{\theta}) = \Sigma(\boldsymbol{\theta})/\Sigma_{\text{cr}}$ is the convergence and $\Sigma_{\text{cr}} \equiv \frac{c^2}{4\pi G} \frac{D_s}{D_{ds} D_d}$ is the critical surface density. Introducing the deflection potential

$$\psi(\boldsymbol{\theta}) = \frac{1}{\pi} \int d^2 \theta' \kappa(\boldsymbol{\theta}') \ln |\boldsymbol{\theta} - \boldsymbol{\theta}'|, \quad (1.71)$$

we derive

$$\boldsymbol{\alpha} = \nabla_{\boldsymbol{\theta}} \psi(\boldsymbol{\theta}), \quad \nabla_{\boldsymbol{\theta}}^2 \psi(\boldsymbol{\theta}) = 2\kappa(\boldsymbol{\theta}). \quad (1.72)$$

From these equations, we see that ψ is the two-dimensional Newtonian potential and satisfies the Poisson equation.

1.7.3 Convergence, shear and magnification

Gravitational lensing induces the distortion of shape and the flux magnification of the source objects. The distortion of the source image is describe by the Jacobian matrix

$$A(\boldsymbol{\theta}) = \frac{\partial \boldsymbol{\beta}}{\partial \boldsymbol{\theta}} = \delta_{ij} - \frac{\partial^2 \psi(\boldsymbol{\theta})}{\partial \theta_i \partial \theta_j} = \begin{pmatrix} 1 - \kappa - \gamma_1 & -\gamma_2 \\ -\gamma_2 & 1 - \kappa + \gamma_1 \end{pmatrix}, \quad (1.73)$$

where the shear γ is introduced as

$$\begin{aligned}\gamma(\boldsymbol{\theta}) &\equiv \gamma_1(\boldsymbol{\theta}) + i\gamma_2(\boldsymbol{\theta}) = |\gamma(\boldsymbol{\theta})| \exp[2i\phi(\boldsymbol{\theta})], \\ \gamma_1 &= |\gamma| \cos 2\phi, \quad \gamma_2 = |\gamma| \sin 2\phi, \\ \gamma_1 &= (\psi_{,11} - \psi_{,22})/2, \quad \gamma_2 = \psi_{,12}.\end{aligned}\tag{1.74}$$

Using the distortion angle ϕ , the Jacobian matrix is rewritten as

$$A = (1 - \kappa) \begin{pmatrix} 1 & 0 \\ 0 & 1 \end{pmatrix} - |\gamma| \begin{pmatrix} \cos 2\phi & \sin 2\phi \\ \sin 2\phi & -\cos 2\phi \end{pmatrix}\tag{1.75}$$

Hence the convergence κ assembles the light paths isotropically and the shear γ distorts anisotropically images of the source objects. The factor of 2 for the distortion angle ϕ comes from a fact that the period of the distortion angle is 180° .

Gravitational lensing induces magnification of the source flux due to the changes in the solid-angle in addition to the convergence and shear. Lensing does not change the total number of photons, the surface brightness I is conserved, i.e., $I(\boldsymbol{\beta}) = I(\boldsymbol{\theta})$. The magnified ratio μ is given as

$$\mu = \frac{\text{Lensed flux}}{\text{Intrinsic flux}} = \frac{\int d^2\theta I(\boldsymbol{\theta})}{\int d^2\beta I(\boldsymbol{\beta})} = \frac{\int d^2\theta I(\boldsymbol{\theta})}{\int d^2\theta |\det A| I(\boldsymbol{\theta})}.\tag{1.76}$$

Assuming that A is constant, i.e., A does not depend on $\boldsymbol{\theta}$, in the image of the source, we obtain

$$\mu = \frac{1}{|\det A|} = \frac{1}{|(1 - \kappa)^2 - \gamma^2|}.\tag{1.77}$$

We see that magnification comes from the combination of the convergence and shear.

Using galaxy survey data to measure cross correlation between such effects and foreground galaxies, we can estimate the mean surface mass density profile around the foreground galaxies Σ even if the lensing effects are tiny. In the case that the lens object is axisymmetric along the line-of-sight, the distortion angle ϕ is zero. From equations (1.72) and (1.74), therefore, average shear γ is equal to average tangential shear γ_1 and related to Σ as

$$\gamma(R) = \gamma_1(R) = \frac{\bar{\Sigma}(< R) - \Sigma(R)}{\Sigma_{\text{cr}}} \equiv \frac{\Delta\Sigma(R)}{\Sigma_{\text{cr}}},\tag{1.78}$$

where $\bar{\Sigma}(< R)$ is the average surface mass density within R and $\Sigma(R)$ is the azimuthally averaged surface mass density at R . In the weak lensing limit, i.e., $\kappa \ll 1$, $\gamma \ll 1$, from equation (1.77), average magnification μ is related to Σ by the Taylor expansion as

$$\mu(R) \simeq 1 + 2\kappa(R) = 1 + 2\frac{\Sigma(R)}{\Sigma_{\text{cr}}}.\tag{1.79}$$

Where we introduced the projected distance from the center of foreground galaxies R which is the frequently used notation in the rest of this thesis. A number of efforts have been made to measure mass profiles around various types of galaxies (e.g., McKay et al. 2001; Sheldon et al. 2004; Mandelbaum et al. 2006a,b; Ménard et al. 2010b; Mandelbaum et al. 2012; Hikage et al. 2012a)

1.8 Phenomenological methods for the galaxy-dark matter halo connections

Data sets from recent galaxy redshift surveys allow us to measure the various statistics of galaxies, e.g., two-point correlation functions, power spectra, lensing profiles, and so on with a high statistical precision. The dependences of statistical quantities on galaxy properties would be clues to unveil the galaxy formation and evolution.

For the interpretation of the observational results, it is needed to reproduce and/or explain the observational results theoretically. However galaxy formation and evolution is a very complex physical process so that it is very hard to compute from the first principles (see Silk & Mamon 2012, for a recent review). An alternative way to make theoretical predictions is given by phenomenological methods. Using cosmological N -body simulations, one can predict halo and subhalo statistics including the mass function, the two-point statistics and so on. Since the relation between galaxies and halos/subhalos is not trivial, one needs to model in physically-based ways. So far, useful and powerful methods have been developed.

One is the halo occupation distribution (HOD) approach or the halo model approach (see Cooray & Sheth 2002, for a review). In this approach, the average number of central and satellite galaxies per halo, i.e., HOD, as a function of halo mass M is parametrized, where the central galaxy is the galaxy which is located in the center of the halo and the satellite galaxy is the galaxy which is located in the envelope of the halo. For instance, Zheng et al. (2005) used hydrodynamical cosmological simulations and semi-analytic models to propose the HOD functional forms for central and satellite galaxies as

$$N_{\text{central}}(M) = 0.5 \left[1 + \text{erf} \left(\frac{\log_{10}(M/M_{\text{min}})}{\sigma_{\log M}} \right) \right], \quad (1.80)$$

$$N_{\text{satellite}}(M) = \left(\frac{M - M_{\text{cut}}}{M_1} \right)^\alpha, \quad (1.81)$$

where M_{min} , $\sigma_{\log M}$, M_{cut} , M_1 and α are free parameters. Together with the halo mass function, bias and a model for the number density distribution of satellite galaxies in each halo, one can easily calculate two-point correlation functions or power spectra for a given parameter set. The free parameters are determined by fitting the HOD prediction to the observed correlation function. It has been shown that the HOD approach reproduces the observational results very well (e.g., Zehavi

et al. 2005; Blake et al. 2008; Zehavi et al. 2011).

The advantage of the HOD approach is its simpleness so that one can compute a correlation function in a few seconds. Also the approach can be easily extended to predict other measurements rather than the two-point correlation functions (e.g., De Bernardis & Cooray 2012; van den Bosch et al. 2012).

The second one is the so-called the subhalo abundance matching (SHAM, Kravtsov et al. 2004). In SHAM, halos are decomposed into a central subhalo, i.e., the smooth component, and satellite subhalos. SHAM assumes a tight relation between a galaxy and a subhalo properties, e.g., galaxy luminosity and subhalo circular velocity. Then a corresponding subhalo sample for a luminosity-threshold galaxy sample would be constructed by just setting a threshold subhalo circular velocity value such that the number density of subhalos and that of the galaxies of a luminosity threshold sample are matched as

$$n_{\text{subhalo}}(> V_{\text{cir}}) = n_{\text{galaxy}}(> L). \quad (1.82)$$

It has been shown that SHAM predictions are in very good agreements with the observed luminosity dependences of two-point correlation functions (Conroy et al. 2006; Trujillo-Gomez et al. 2011) and lensing profiles (Tasitsiomi et al. 2004). Reddick et al. (2012) showed that SHAM works well for not only the luminosity-threshold galaxy samples but also the stellar mass-threshold ones.

The most attractive feature of SHAM is that it does not have fitting parameters. Its agreement is solely relies on physical adequateness of the assumed tight relation between a galaxy and a subhalo properties. Also the direct use of N -body simulation data allows one to include the non-linear evolution of galaxy and matter clustering accurately.

1.9 Outline

The rest of this thesis is as follows. In chapter 2, we study the mass distribution around galaxies using high resolution cosmological N -body simulations. The results from simulations are compared with the measurement obtained through the lensing techniques. We also discuss the mass distribution at the larger scale than the galactic halos' virial radius. The contents are based on Masaki, Fukugita, & Yoshida (2012a).

In chapter 3, we extend the discussions in chapter 2 for the dust distribution around galaxies. We develop a simple formulation based on the halo model approach to predict the distribution of dust around galaxies. By fitting the model predictions to an observational result, we discuss the extent of dust from galaxies. The contents are based on Masaki & Yoshida (2012).

In chapter 4, we develop a method to assign galaxy color to simulated subhalos in addition to luminosity by extending the subhalo abundance matching method. We examine models for the relation between galaxy color and subhalo properties. We compare the model results with the observed color dependences of the two-point correlation functions and the lensing profiles to discuss the relation between galaxy

color and subhalo properties. The contents are based on Masaki, Lin, & Yoshida (2012c).

In chapter 5, we develop a novel abundance matching method to construct a mock catalog of luminous red galaxies (LRGs) using large cosmological simulations. We compare the model predictions for the two-point correlation functions and the lensing measurements to test our method. Using the constructed mock catalog, we study the properties of satellite LRGs and discuss the implications for the Finger-of-God effect. The contents are based on Masaki, Hikage, Takada, Spergel, & Sugiyama (2012b).

Finally, in chapter 6, we give a summary of this thesis and discuss the future prospects based on the results in this thesis.

Chapter 2

Distribution of Mass around Galaxies: Lensing Measurements and Structures beyond the Virial Radius

2.1 Introduction

Probing the distribution of matter in and around galaxies is one of the primary goals of observational cosmology. Observationally, gravitational lensing provides a powerful method to map the matter distribution at small and large length scales (for a review, see Bartelmann & Schneider 2001). Recent large redshift surveys, such as the Sloan Digital Sky Survey (SDSS; York et al. 2000), have allowed us to explore the mean surface density profile of galaxies and galaxy clusters through weak lensing techniques (e.g., McKay et al. 2001; Sheldon et al. 2004; Mandelbaum et al. 2006a,b; Ménard et al. 2010b; Reyes et al. 2010).

The surface density profile is the projection of the three dimensional density distribution along the line-of-sight,

$$\Sigma(R) = \int d\pi \rho \left(r = \sqrt{R^2 + \pi^2} \right), \quad (2.1)$$

where r is three dimensional distance, π is the line-of-sight, and R is two dimensional distance in the lens plane. The mass surface density of lens objects can be probed through tangential shear γ_t or magnification μ of background objects. In the weak lensing regime, they can be related to the surface density via the following equations:

$$\gamma_t(R) = \frac{\bar{\Sigma}(< R) - \Sigma(R)}{\Sigma_{\text{cr}}} = \frac{\Delta\Sigma(R)}{\Sigma_{\text{cr}}}, \quad (2.2)$$

$$\mu(R) \simeq 1 + 2\kappa(R) = 1 + 2\frac{\Sigma(R)}{\Sigma_{\text{cr}}}, \quad (2.3)$$

where $\bar{\Sigma}(< R)$ is the average of surface density within R , κ is the convergence and Σ_{cr} is the critical surface density (see chapter 1). Using these relation, one can estimate the mean surface density profile of sample galaxies, groups or clusters from the observed average shear or magnification.

Ménard et al. (2010b, hereafter MSFR in this chapter) measured the mean surface density profile of SDSS galaxies with the mean redshift $\langle z \rangle = 0.36$. They calculated the cross correlation function between the number density fluctuation of foreground galaxies and the flux magnification fluctuation of background quasars. The derived $\Sigma(R)$ of MSFR has two interesting features. Firstly, it is well described by a power law $\Sigma \propto R^{-0.8}$. One may naively expect that, if the galactic halos have Navarro-Frenk-White (NFW) density profiles (Navarro et al. 1997), the surface density decreases as $\propto R^{-2}$ at large radii ($\sim 1\text{Mpc}$). The observed power-law does not appear to agree with this expectation. It is clearly important to study if the observed surface density profile is consistent with the matter distribution in the standard Λ cold dark matter (ΛCDM) model. The second interesting feature is that the power law form of the mean surface density profile continues from $\sim 10h^{-1}\text{kpc}$ to $\sim 10h^{-1}\text{Mpc}$. This implies that the galaxy have a very extended dark matter halo, well beyond the typical virial radius of galaxies of about a few $\times 100h^{-1}\text{kpc}$.

There have not been many studies on the magnification signals rather than the shear signals observationally and analytically, with an important exception of MSFR. The lensing tangential shear and magnification signals provide different estimators of the mass surface density (see equations [2.2] and [2.3]). In addition, as shown in MSFR, the magnification measurement enables us to explore the distribution of not only mass but also dust around the lens objects by detecting quasar reddening. Hence, it is important to study the magnification measurements using simulations.

In this chapter, we study the matter distribution in and around galactic halos in the standard cosmological model. We use high-resolution N -body simulations to predict surface density profiles. We compare the predictions with the observed surface density profile obtained from the magnification measurement.

Also we address the “*missing dark matter problem*” (Fukugita & Peebles 2004). One may naively think that matter is borne by galaxies in large part. Amount of such borne matter is estimated by multiplying the luminosity density \mathcal{L} by the average mass-to-light ratio $\langle M/L \rangle$ as $\rho_{\text{m}} = \mathcal{L} \times \langle M/L \rangle$. Using the SDSS results of $\mathcal{L} = 2.2 \pm 0.3 \times 10^8 hL_{\odot}\text{Mpc}^{-3}$ (Blanton et al. 2001, 2003) and $\langle M/L \rangle \simeq (170 \pm 50) hM_{\odot}L_{r\odot}^{-1}$ which is inferred from lensing shear (McKay et al. 2001), we obtain

$$\Omega_{\text{m,galaxy}} = 0.13 \pm 0.05. \quad (2.4)$$

This value is only half of the convincing global matter density of

$$\Omega_{\text{m}} = 0.27 \pm 0.03 \quad (2.5)$$

estimated from cosmological observations (Komatsu et al. 2011). The difference

between these two values raises a question, “*where is the half of matter?*”. We explore matter distributions in outer region of halos to discuss this problem.

2.2 Method

2.2.1 Cosmological N -body simulations

We use the parallelized N -body simulation code *Gadget-2* (Springel et al. 2001b; Springel 2005) in its Tree-PM mode. The cosmological parameters we adopted are, with the standard notations, $\Omega_m = 0.258$, $\Omega_b = 0.0441$, $\Omega_\Lambda = 0.742$, $h = 0.719$, $n_s = 0.963$ and $\sigma_8 = 0.796$. These parameters are consistent with the *WMAP* five-year results (Komatsu et al. 2009). We employ 1024^3 particles in a box of comoving $200h^{-1}\text{Mpc}$ on a side. The mass of a dark matter particle is then $5.34 \times 10^8 h^{-1} M_\odot$. Hence we are able to locate dark halos with mass of a few times $10^{10} h^{-1} M_\odot$ robustly. We set the gravitational softening parameter $\epsilon = 10h^{-1}\text{kpc}$.

We set the initial redshift $z_i = 50$ and generate the initial condition using the second-order Lagrangian perturbation theory (2LPT; Scoccimarro 1998; Nishimichi et al. 2009) rather than the standard Zel’dovich approximation (ZA; Zel’dovich 1970). 2LPT is more accurate to generate initial conditions and has an advantage to allow us to set the initial redshift more later than ZA (Crocce et al. 2006; Jenkins 2010). The initial matter power spectrum at $z = z_i$ is computed by *CAMB* (Lewis et al. 2000) for the adopted cosmological parameters.

2.2.2 Halo identification

Halo identification is done in a two-step manner. First, we select candidate objects using the friends-of-friends (FoF) algorithm (Davis et al. 1985). We set the linking parameter $b = 0.2$. Figure 2.1 shows the mass function of the FoF groups at $z = 1$ and 0.1 . The symbols are from our simulation and the solid lines show the analytic model of Sheth & Tormen (1999). While the simulation and the model agree with each other reasonably well, slight differences are also seen at the low and high mass scales. This is likely due to our use of 2LPT in the generation of the initial condition in our simulation. Similar discrepancies are also reported by Crocce et al. (2010) who have used 2LPT. The dashed lines denote the fitting formula proposed by Crocce et al. (2010), which indeed agree with our simulation.

We apply the spherical over density algorithm to the located FoF groups that contains 200 particles at least. To each FoF group, we assign a mass such that the enclosed mass within the virial radius is $\Delta \times \rho_{\text{crit}}(z)$. Based on the spherical collapse model, Δ is set to 200 (see chapter 1). We set the minimum number of particles in a halo to 100 and have identified 229,805 halos with the masses greater than $5.34 \times 10^{10} h^{-1} M_\odot$ at $z = 0.36$.

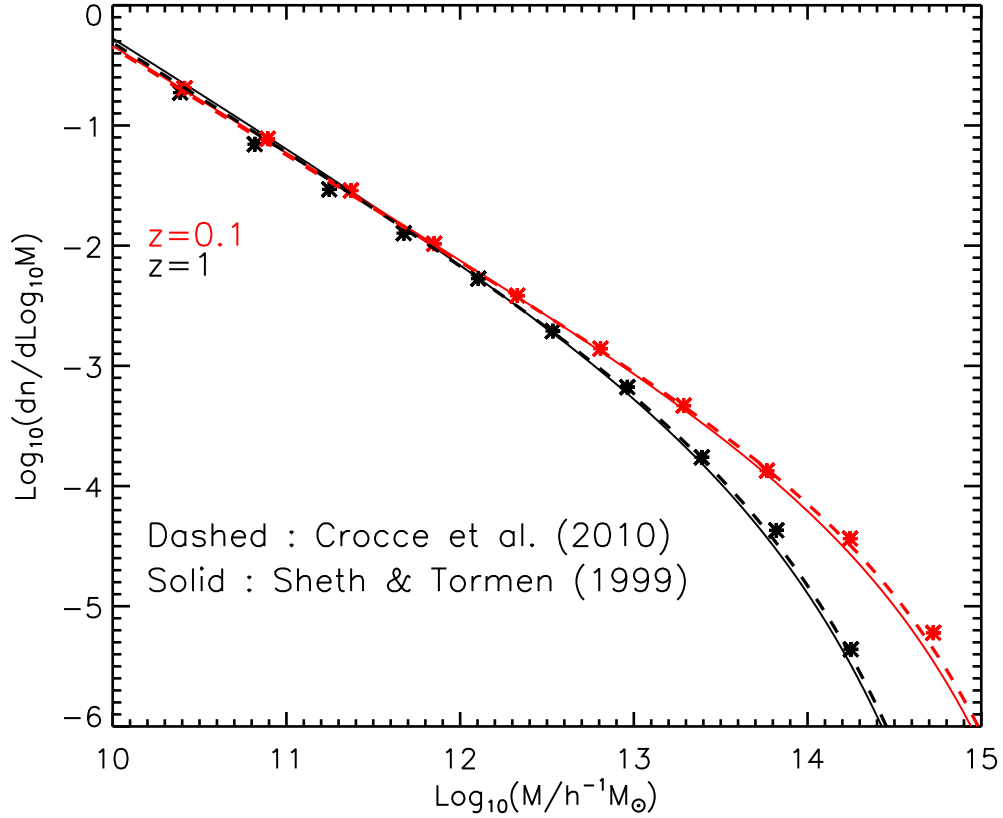


Figure 2.1: The mass function of the FoF groups at $z = 1$ (black) and 0.1 (red). The symbols are from our simulations and the solid lines are the analytic model of Sheth & Tormen (1999). We see a slight difference between our 2LPT simulation and the Sheth-Tormen model, which is consistent with the findings of Crocce et al. (2010).

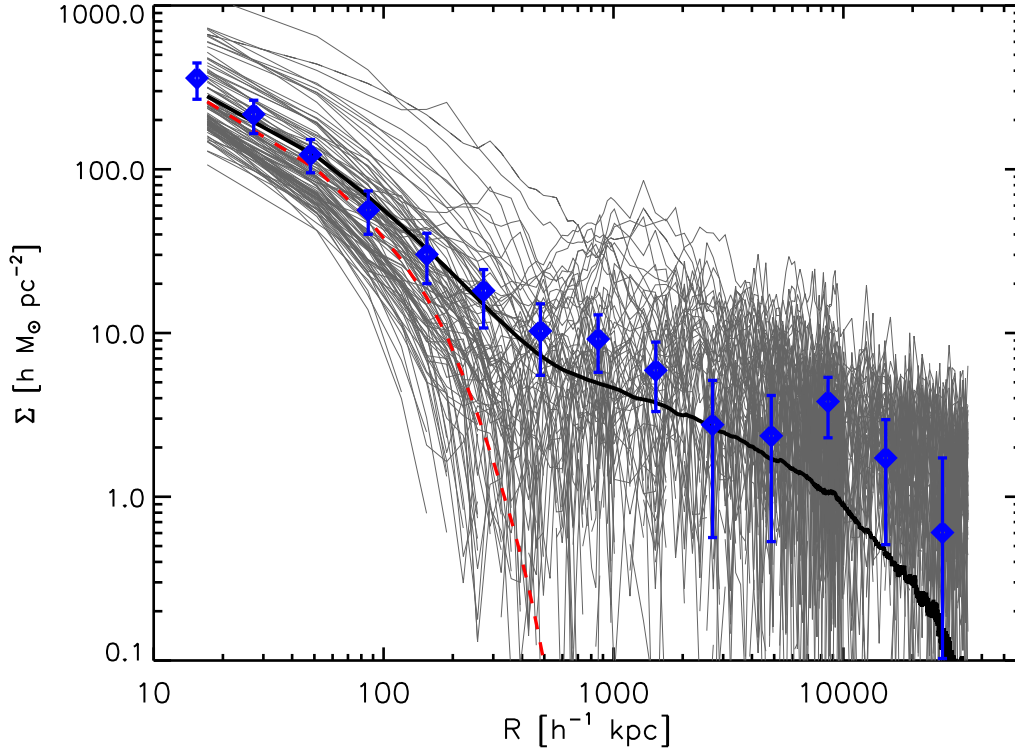


Figure 2.2: The surface density profiles as a function of the projected distance. The simulation is represented by a bunch of thin curves for 100 halos randomly chosen from the 9970 halos that have a virial mass in the range of $2 \times 10^{12} - 5 \times 10^{14} h^{-1} M_{\odot}$. The thick solid line shows the average for the sample halos. The red dashed line shows the contribution from the so-called one-halo term. The data points with error bars are taken from MSFR.

2.3 Mean surface density profiles around halos

2.3.1 Comparisons with MSFR

The mean surface density profile around halos is computed in the following manner. We shift the simulation volume to be centered on a halo. We then project all simulation particles in the simulation box and compute the surface density around the center as a function of projected distance. Finally, we calculate the average of the profiles of all the selected halos, to obtain the mean surface density profile.

Figure 2.2 compares our simulation result with that of MSFR. The horizontal axis corresponds to the physical distance from the center of the halo at $z = 0.36$. The simulation is represented by a bunch of thin curves for 100 halos randomly chosen from the 9970 halos that have a virial mass larger than $2 \times 10^{12} h^{-1} M_{\odot}$ (this choice is discussed below). The maximum halo mass in our simulation is $5 \times 10^{14} h^{-1} M_{\odot}$. The thick solid line is the average for the 9970 halos. The simulation result agrees with the observational result very well, both in the amplitude and in the overall

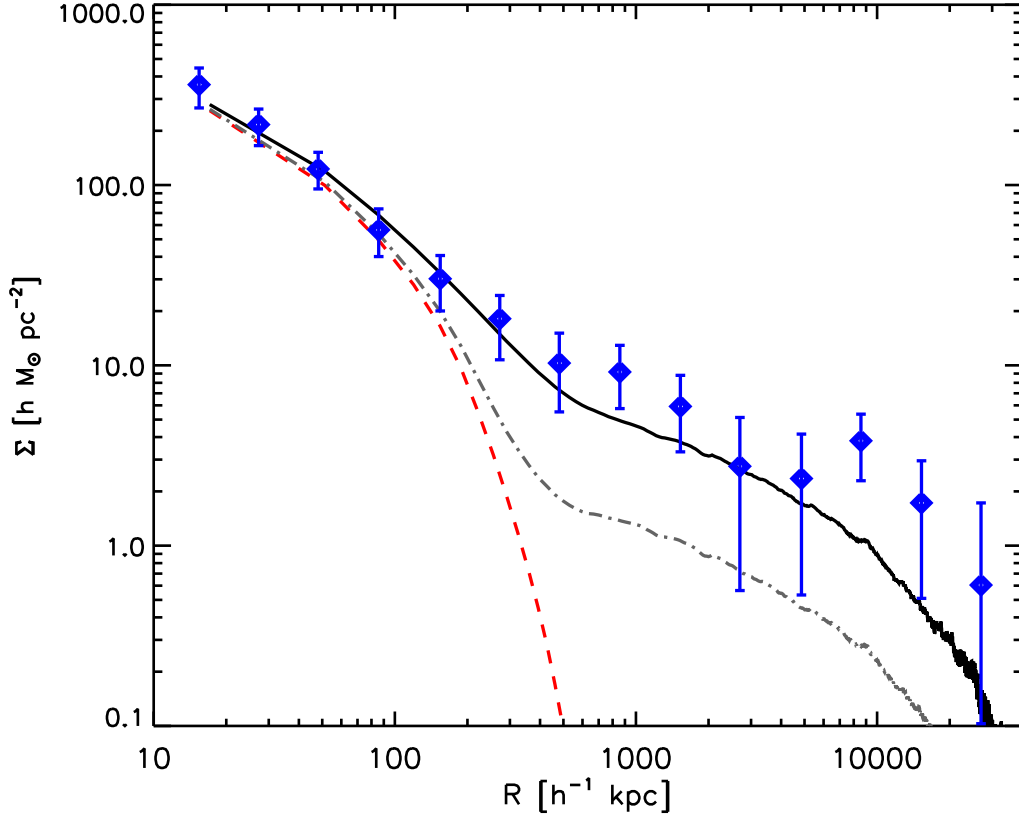


Figure 2.3: Mean surface density profiles around halos : the black solid line, the blue symbols with error bars and the red dashed line are same in Figure 2.2. The gray dotted-dashed line shows the contribution from the neighbouring halos and the central halo. It amounts to only 25% of the surface density of the total (using all particles in the column) at $R > 500h^{-1}\text{kpc}$.

shape. The red dashed line shows the contribution from the central halo truncated at its virial radius, the so-called one-halo term. Clearly, the mean surface density at $R \lesssim 100h^{-1}\text{kpc}$ is dominated by the one-halo term.

The column which has a halo in its center extracted from our simulation box contains not only the neighbouring halos but also “diffuse” particles, where particles not bound in any halos identified in our simulation are defined as diffuse particles. In order to study how neighbouring halos contribute to the mean surface density, we remove the diffuse particles from the column, and then re-compute the mean surface density profile.

Figure 2.3 shows the resulting mean surface density profile for this case. The gray dotted-dashed line is the surface density without diffuse particles. Interestingly, the contribution from the neighbouring halos at $R \gtrsim 500h^{-1}\text{kpc}$ is small, about 25% of the surface density in the case of using all particles. This implies that the diffuse particles dominate the mean surface density at the large scales and thus there is a significant amount of dark matter associated with halos.

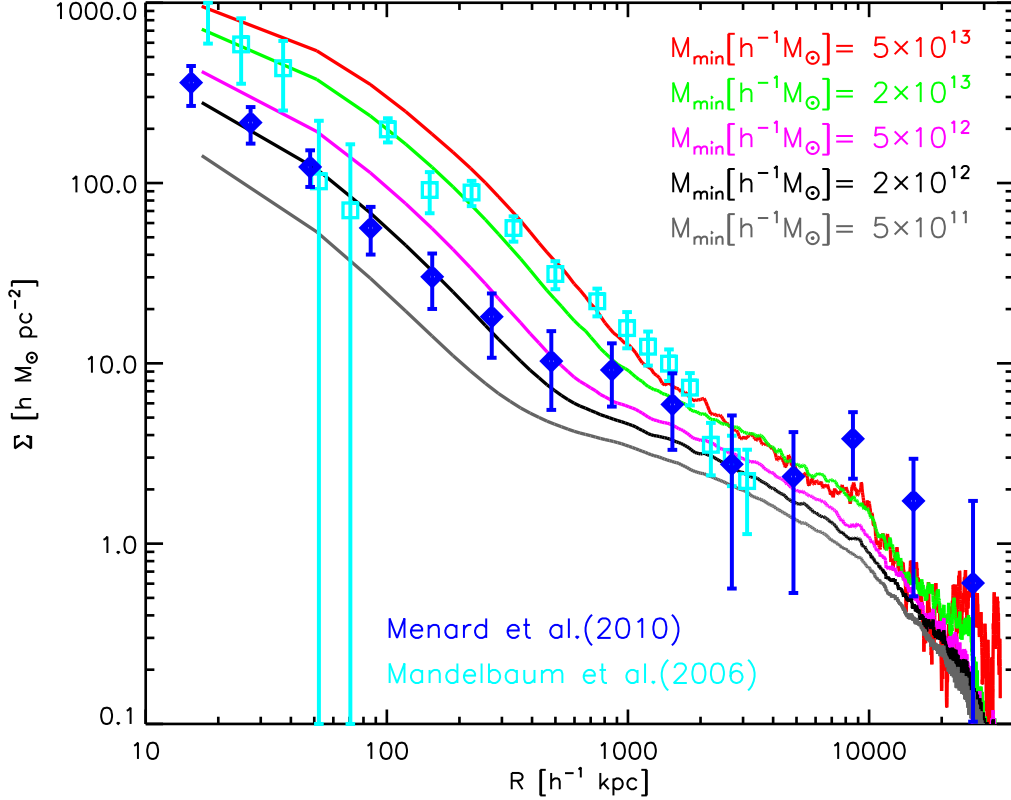


Figure 2.4: Mean surface density profiles around halos for cases with five different lower mass limits. The strong dependence reflects the effect of halo mass function on the ensemble averaging (see text). The cyan data points are for an LRG sample (Mandelbaum et al. 2006a).

2.3.2 The effect of the mass range

We now examine how the choice of the halo mass range affects the mean surface density. In the previous section, the mass range of the central halos is set to be $2 \times 10^{12} h^{-1} M_{\odot} \sim 5 \times 10^{14} h^{-1} M_{\odot}$. Here, we compute the mean surface density profiles by varying the low mass threshold. The upper limit is fixed to $5 \times 10^{14} h^{-1} M_{\odot}$ and we tried five lower limits $M_{\min}[h^{-1} M_{\odot}]$ as follows : 5×10^{11} , 2×10^{12} , 5×10^{12} , 2×10^{13} and 5×10^{13} . Note that the choice of the upper mass does not affect the result significantly. because of the steep mass function at large masses (see Figure 2.1).

The mean surface density profiles for the five cases are shown in Figure 2.4. At $R < 1 h^{-1} \text{Mpc}$, the amplitude of the mean surface density has a strong dependence on M_{\min} . Among the samples used to calculate the mean surface density, the low mass halos are dominant in number (see Figure 2.1). The total number of halos in different mass bins and the corresponding number fraction at $z = 0.36$ are summarized in Table 2.1. Since the one-halo term dominates the amplitude of the surface density at small length scales, the choice of M_{\min} significantly affects the mean density. This

Table 2.1: The number, the number fraction and the mass fraction of halos at $z = 0.36$.

Mass bin [$h^{-1}M_{\odot}$]	Total number	Number fraction [%]	Mass fraction [%]
$5 \times 10^{10} - 5 \times 10^{11}$	189,578	82.5	5.91
$5 \times 10^{11} - 5 \times 10^{12}$	36,402	15.8	8.25
$5 \times 10^{12} - 5 \times 10^{13}$	3,637	1.58	7.64
$5 \times 10^{13} - 5 \times 10^{14}$	187	0.0814	3.13

in turn suggests that, the characteristic mass of the sample galaxies can be inferred from the mean surface density, as we will discuss later.

Figure 2.5 shows the dependence of the mean surface density at $R = 50$ and $120h^{-1}\text{kpc}$, where the one-halo term is expected to dominate in each mass range, on M_{\min} . The dependence can be approximated by $\Sigma \propto M_{\min}^{2/3}$, as indicated in the figure by the grey dotted lines. This can be easily understood as follows. For simplicity, we assume the singular isothermal sphere (SIS) profile for all halos. The surface density profile of the SIS halo is

$$\Sigma_{\text{SIS}}(R) = \int_{-\infty}^{\infty} \rho_{\text{SIS}}(\sqrt{R^2 + \pi^2}) d\pi = \int_{-\infty}^{\infty} \frac{M}{4\pi R_{\text{vir}}(R^2 + \pi^2)} d\pi = \frac{M}{4R_{\text{vir}}R}. \quad (2.6)$$

Using the approximate relation between the mass and the virial radius $R_{\text{vir}} \sim M^{1/3}$, we obtain

$$\Sigma(R) \sim \frac{M^{2/3}}{R}. \quad (2.7)$$

It is summarized at 50 and 120 $h^{-1}\text{kpc}$ as

$$\begin{aligned} \Sigma_{50} &\simeq 245[M_{\min}/(8 \times 10^{12}h^{-1}M_{\odot})]^{2/3} hM_{\odot}\text{pc}^{-2}, \\ \Sigma_{120} &\simeq 100[M_{\min}/(8 \times 10^{12}h^{-1}M_{\odot})]^{2/3} hM_{\odot}\text{pc}^{-2}. \end{aligned} \quad (2.8)$$

The grey dotted lines in Figure 2.5 show these equations. We see that they agree qualitatively well with the simulation results as clearly seen in the figure.

Figure 2.4 indicates that the mean surface density profile around galaxies measured by MSFR is reproduced when M_{\min} is set to a few $\times 10^{12}h^{-1}M_{\odot}$. We therefore conclude that the typical mass of the lens galaxies used in MSFR is a few $\times 10^{12}h^{-1}M_{\odot}$. Note, however, that there could be a few uncertainties in the above argument. Baryonic physics, which are not included in simulations, may affect the halo density profile at small radii. We also have neglected the redshift distribution of MSFR's sample galaxies. MSFR has not done a non-linear treatment of the magnification needed at $R \lesssim 100h^{-1}\text{kpc}$ (Ménard et al. 2003). Further studies considering all of these issues are clearly needed.

Figure 2.4 also shows Σ for luminous red galaxies (LRGs) measured by Mandelbaum et al. (2006a) for comparison. The figure shows that the LRGs profile is

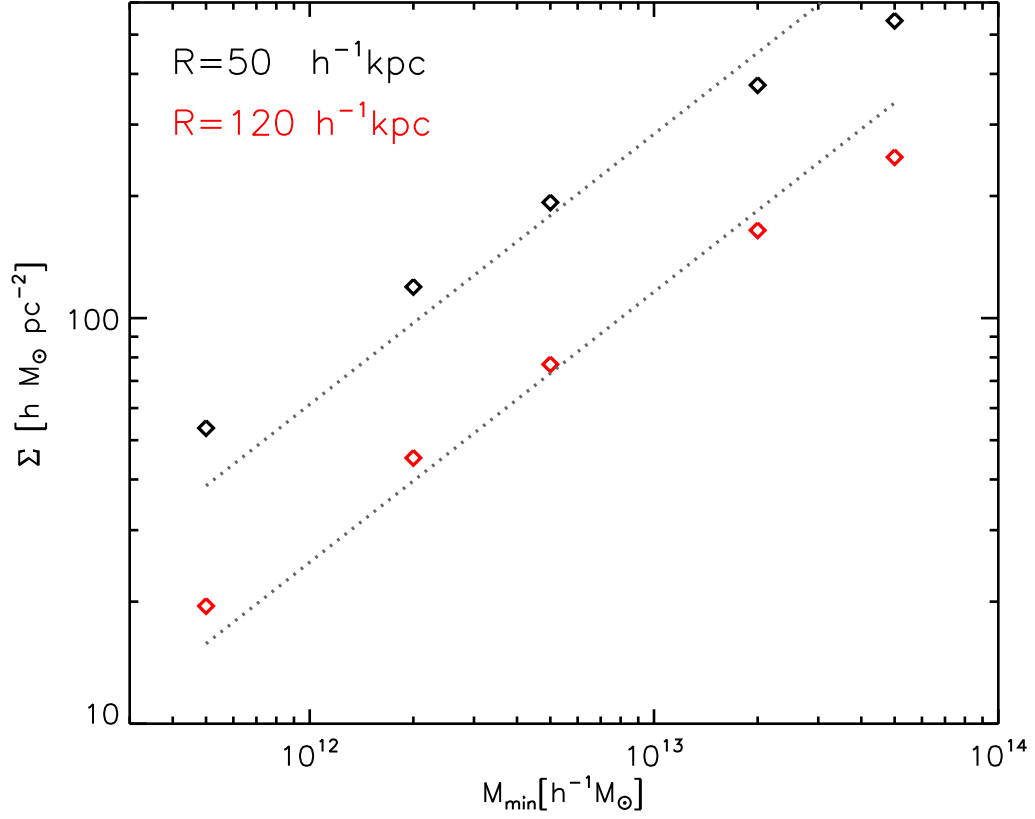


Figure 2.5: The dependence of the mean surface density at $R = 50$ and $120 h^{-1} \text{kpc}$ on M_{\min} . We found that the dependence can be approximated by a simple power law form $\Sigma \propto M_{\min}^{2/3}$. We can roughly understand it by assuming the SIS profile for sample halos (see text).

in a good agreement with the profile for $M_{\min} = 2 \times 10^{13} h^{-1} M_{\odot}$ at small R . Thus the implied typical halo mass for LRGs of $\sim 10^{13} h^{-1} M_{\odot}$ is consistent with the halo model estimation by Mandelbaum et al. (2006a).

2.3.3 NFW vs. SIS

It is interesting to consider if one can discriminate the halo density profiles, such as NFW and SIS, by comparing the predictions with the observed surface mass density profile. To this end, we directly fit the density profile for all the halos identified in our simulation using the NFW profile and by the SIS profile. The surface density of the truncated NFW halo is given by its projection (Hamana et al. 2004) as

$$\begin{aligned}\Sigma_{\text{NFW}}(R) &= \int_{-\sqrt{R_{\text{vir}}^2 - R^2}}^{\sqrt{R_{\text{vir}}^2 - R^2}} d\pi \rho_{\text{NFW}}(r = \sqrt{R^2 + \pi^2}) \\ &= 2\rho_s r_s f(y),\end{aligned}\tag{2.9}$$

$$y \equiv R/r_s,\tag{2.10}$$

$$f(y) = \begin{cases} -\frac{\sqrt{c^2 - y^2}}{(1 - y^2)(1 + c)} + \frac{1}{(1 - y^2)^{3/2}} \text{arccosh} \frac{y^2 + c}{y(1 + c)} \\ \quad (\text{for } y < 1) \\ \frac{\sqrt{c^2 - 1}}{3(1 + c)} \left(1 + \frac{1}{1 + c}\right) \\ \quad (\text{for } y = 1) \\ -\frac{\sqrt{c^2 - y^2}}{(1 - y^2)(1 + c)} - \frac{1}{(y^2 - 1)^{3/2}} \arccos \frac{y^2 + c}{y(1 + c)} \\ \quad (\text{for } 1 < y \leq c) \\ 0 \\ \quad (\text{for } y > c), \end{cases}$$

where r_s is the scale radius and ρ_s is the amplitude (see chapter 1). Here, we redefine a truncated SIS profile as well as the NFW.

$$\begin{aligned}\Sigma_{\text{SIS}}(R) &= \int_{-\sqrt{R_{\text{vir}}^2 - R^2}}^{\sqrt{R_{\text{vir}}^2 - R^2}} d\pi \rho_{\text{SIS}}(r = \sqrt{R^2 + \pi^2}) \\ &= \frac{M \arctan \left(\sqrt{R_{\text{vir}}^2 / R^2 - 1} \right)}{2\pi R_{\text{vir}} R}\end{aligned}\tag{2.11}$$

Using these expressions and the halo mass function in our simulation, we can calculate the average surface density profiles for NFW and SIS for a certain halo mass range.

Figure 2.6 shows the mean surface density profiles at $R < 150 h^{-1} \text{kpc}$ for the cases of NFW and SIS. As well as Figure 2.2, the adopted halo mass range is $2 \times 10^{12} \sim 5 \times 10^{14} [h^{-1} M_{\odot}]$. The figure shows that the NFW case seems to agree with the simulation result slightly better than the SIS. However both cases are

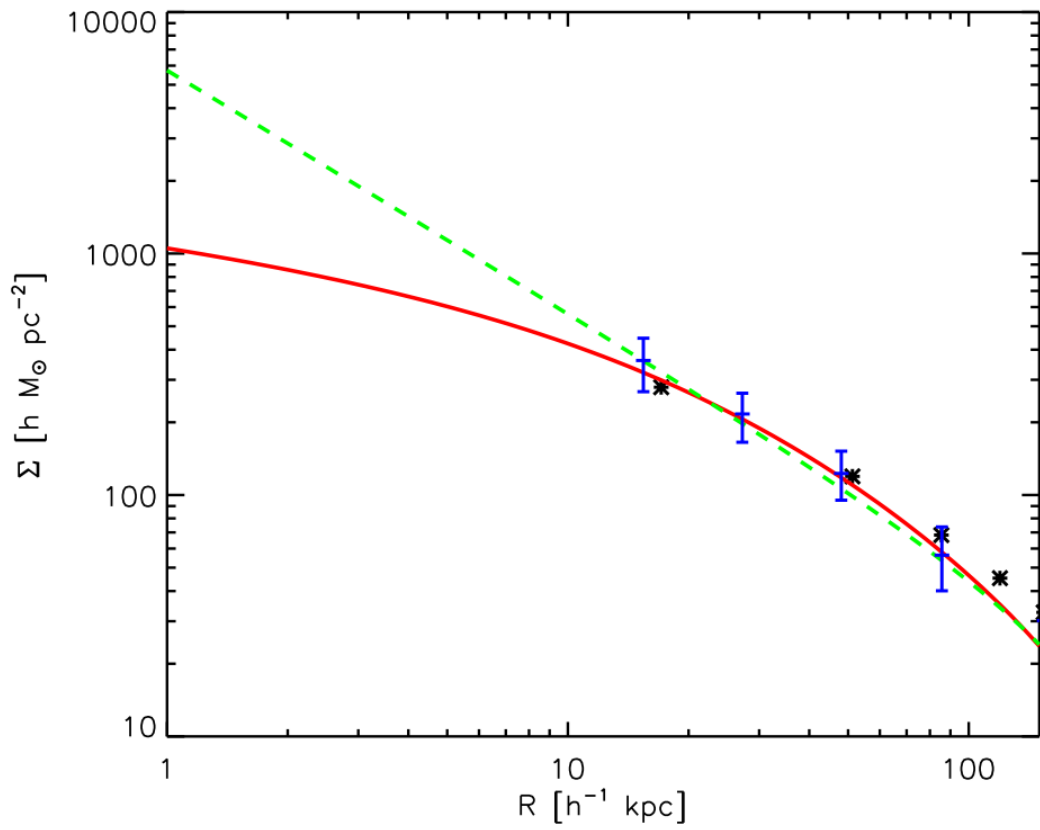


Figure 2.6: The mean surface density profiles around halos at $R < 150h^{-1}\text{kpc}$. The black asterisk denotes the mean profile of the halo sample with the mass range $2 \times 10^{12} \sim 5 \times 10^{14} [h^{-1}M_{\odot}]$, i.e., same as the thick solid line in Figure 2.2. The data with error bars is taken from MSFR. The red solid and the green dashed lines show the mean profile when the sample halos' profiles are fitted to the NFW or SIS, respectively.

consistent with the MSFR result, suggesting that one cannot distinguish the NFW and SIS profiles from the observation. As is shown in Figure 2.6, observations that probe surface densities at smaller scale are needed to distinguish the two.

Mandelbaum et al. (2006a) studied the surface mass density profiles of the galaxy groups and clusters traced by the LRGs through the tangential shear signal. They found that the NFW profile agrees with the observational results, and excluded the SIS profile although the ranges of separation in the lens plane are larger than our study here. This is because they used the LRGs which are more massive ($\sim 10^{13}h^{-1}M_{\odot}$, see Figure 2.4) and larger than typical galaxies. Such more massive halos have smaller concentration than less massive halos (e.g., Bullock et al. 2001). As well as the virial radius, the scale radius r_s of the LRG host halos is larger than that of smaller galaxies. Thus it is easier for one to distinguish the NFW and SIS profiles for LRGs.

2.4 Mass distribution beyond the virial radius

We showed that “diffuse” N -body particles substantially contribute to the mean surface density profiles in Figure 2.3. To examine how the diffuse mass is distributed, we study the amount of dark matter associated with halos using simulation outputs. We measure the enclosed mass within $\alpha \times R_{\text{vir}}$ around halos. We progressively increase the value of α from 1 to 30 and calculated the total enclosed mass around halos. For clarity, the total mass in αR_{vir} is converted to the density parameter as

$$\Omega_{\text{halo}}(\alpha) \equiv \frac{\sum_i M_{\text{halo},i}(\alpha)/L_{\text{box}}^3}{\rho_{\text{cr}}}, \quad (2.12)$$

where L_{box} is the box size of our simulation and $M_{\text{halo},i}(\alpha)$ is the total mass in and around the i -th halo for a given value of α . Hence $\Omega_{\text{halo}}(\alpha = 1)$ is just an integration of the halo mass function. Similarly, the total occupied volume is expressed as

$$V_{\text{halo}}(\alpha) = \sum_i \frac{4\pi}{3} (\alpha R_{\text{vir},i})^3, \quad (2.13)$$

where $R_{\text{vir},i}$ is the virial radius of the i -th halo. Strictly speaking, these expressions are not exact because there are some overlap regions between two or more halos for larger α . We simply avoid double counting in mass and in volume when we calculate $\Omega_{\text{halo}}(\alpha)$ and $V_{\text{halo}}(\alpha)$ by

Figure 2.7 shows $\Omega_{\text{halo}}(\alpha)/\Omega_{\text{m}}$ as a function of α . For this calculation, we use all halos with mass more than $10^{11}h^{-1}M_{\odot}$. The dashed line with symbols is the simulation result. The solid line is a fitting function of

$$\Omega_{\text{halo}}/\Omega_{\text{m}} = 0.23 \ln \alpha + 0.22 \quad (2.14)$$

of which the α dependence is consistent with r^{-3} regime, i.e., $r \gg r_s$ regime, of the

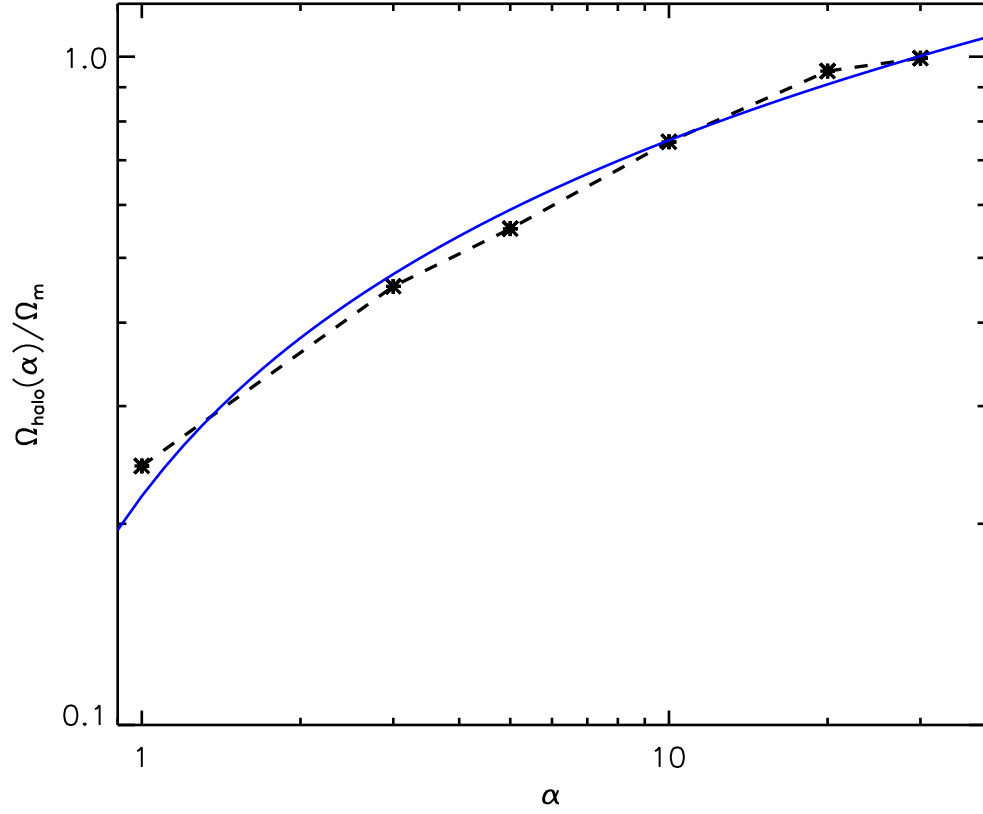


Figure 2.7: We show the total mass density Ω_{halo} scaled by Ω_{m} as a function of α . We use all halos with mass more than $10^{11}h^{-1}M_{\odot}$. The dashed line with symbols is the simulation result. The blue solid line is $0.23 \ln \alpha + 0.22$ (see text).

NFW profile. The figure shows that the matter within the virial radius is only 25% (see $\alpha = 1$). We also see that a half of matter is contained within $\sim 4R_{\text{vir}}$. With large α of > 20 , almost all matter is accounted.

McKay et al. (2001) measured the mass distribution through the lensing shear signals as we referred earlier in this chapter. They obtained

$$\Sigma(R) \simeq 3(R/1h^{-1}\text{Mpc})^{-0.8} hM_{\odot}\text{pc}^{-2}. \quad (2.15)$$

Comparing with our simulation results (see Figure 2.4), we obtain $M_{\text{min}} \simeq 1.5 \times 10^{11}h^{-1}M_{\odot}$ for the sample in McKay et al. (2001). This value is comparable to the threshold mass $10^{11}h^{-1}M_{\odot}$ for Figure 2.7. In our simulation, we found the average virial mass $\bar{R}_{\text{vir}}-M_{\text{min}}$ relation as

$$\bar{R}_{\text{vir}} = 100(M_{\text{min}}/10^{11}h^{-1}M_{\odot})^{0.29} h^{-1}\text{kpc}. \quad (2.16)$$

$M_{\text{min}} = 1.5 \times 10^{11}h^{-1}M_{\odot}$ gives $\bar{R}_{\text{vir}} = 112h^{-1}\text{kpc}$. McKay et al. (2001) claimed that they measured $\langle M/L \rangle$ within the scale of $260h^{-1}\text{kpc}$ which corresponds to $\alpha = 2.3$. From equation (2.14), $\alpha = 2.3$ leads $\Omega_{\text{halo}}/\Omega_{\text{m}} = 0.41$. Using equation (2.4), hence, we obtain the global matter density from the matter associated with halos as

$$\Omega_{\text{m}} = \frac{\Omega_{\text{halo}}}{0.41} = \frac{0.13}{0.41} \simeq 0.32, \quad (2.17)$$

which is in nice agreement with the global matter density (equation [2.5]). Although above estimations are very crude, this agreement implies that the mass beyond the virial radius we examined here is probably broadly correct.

Figure 2.8 shows the enclosed mass fraction $\Omega_{\text{halo}}(\alpha)/\Omega_{\text{m}}$ as a function of the volume occupancy $V_{\text{halo}}(\alpha)/V_{\text{box}}$ where V_{box} is the simulation box volume. From the figure, we easily find that more than a half of the total mass is enclosed within about 10% of the volume ($\alpha = 5$). If the mass distribution is random in outer region of halos, Ω_{halo} should be proportional to V_{halo} . However the figure shows that it is not the case. Also it is seen that there is no clear break at any α and the relation between Ω_{halo} and V_{halo} has a power law like form. The red solid line shows the case of

$$\Omega_{\text{halo}}(\alpha)/\Omega_{\text{m}} \propto [V_{\text{halo}}(\alpha)/V_{\text{box}}]^{0.2} \quad (2.18)$$

and agrees with the simulation result very well. The power law index of 0.2 means that the mass distribution beyond the virial radius behaves follows in average

$$\rho \propto r^{-2.4} \quad (2.19)$$

which is numerically consistent with the NFW profile at $r/r_s = 5 \sim 100$. Having $R_{\text{vir}}/r_s \simeq 5$ and $R_{\text{vir}} = \text{a few} \times 100h^{-1}\text{kpc}$, the relevant scale range is in the inter-galaxy distance of a few \times Mpc. Therefore we conclude that galactic halos do not have clear edges of the matter distribution, extending to the middle of neighboring

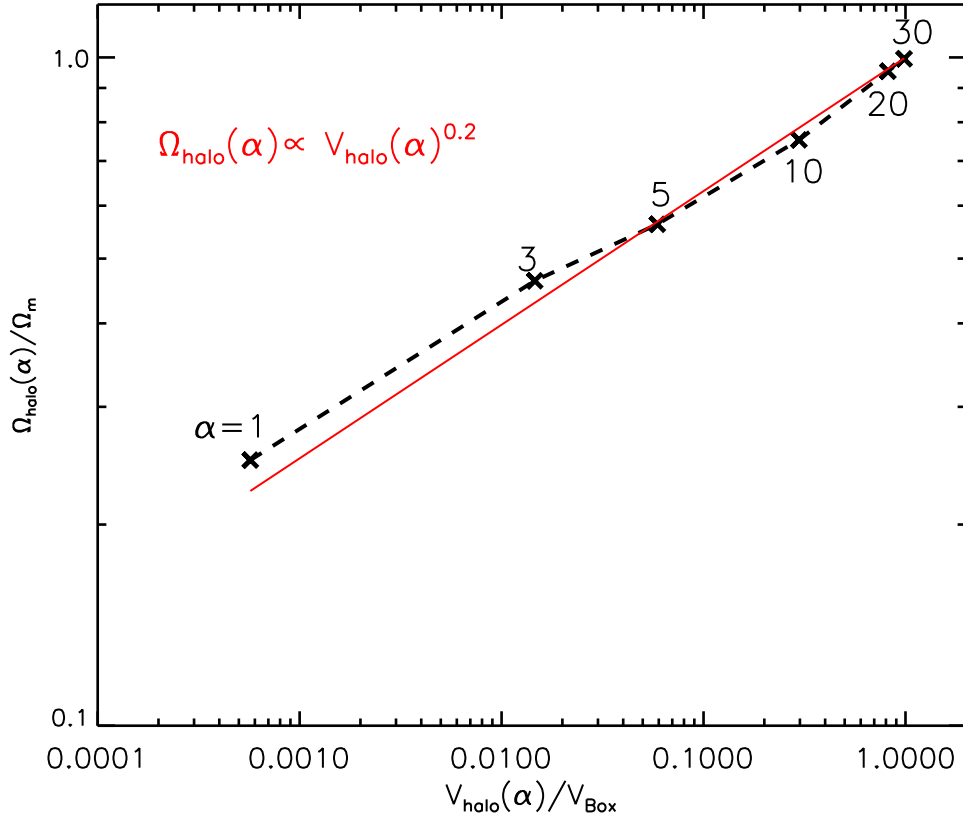


Figure 2.8: The enclosed mass fraction $\Omega_{\text{halo}}/\Omega_{\text{m}}$ as a function of the volume occupancy $V_{\text{halo}}/V_{\text{box}}$. There are six data points corresponding to $\alpha = 1, 3, 5, 10, 20$ and 30 . The red solid line shows the case of $\Omega_{\text{halo}}(\alpha)/\Omega_{\text{m}} \propto [V_{\text{halo}}(\alpha)/V_{\text{box}}]^{0.2}$.

halos.

2.5 Summary

We used high resolution N -body simulations to study the distribution of dark matter in around, and beyond halos. We showed that Λ CDM simulation can reproduce the mean surface density profile Σ of SDSS galaxies reported by Ménard et al. (2010b, MSFR) remarkably well (Figure 2.2). We found that the mean profile amplitude varies with a typical halo mass M_{\min} . We estimated the typical halo mass of sample galaxies used in MSFR is a few $\times 10^{12} h^{-1} M_{\odot}$ (Figure 2.4). In Figure 2.3, we study the contributions from “diffuse” N -body particles, i.e., unbound particles within halos. The figure shows that bound particles within halos contribute up to 25% of the total surface density at large scale $R > 500 h^{-1} \text{kpc}$. In Figure 2.5, we explained the dependence of the one-halo term of Σ by simply assuming the SIS profile for all halos. We showed that one cannot discriminate the NFW and SIS profiles for the MSFR results but that possibility in the small scales (see Figure 2.6).

We employed our simulation data to study the mass distribution beyond the halo virial radius. We measured the enclosed mass fraction (Figure 2.7) and the volume occupancy (Figure 2.8) around halos as functions of the encircling factor α . We found that galactic halos have no definite edges of the matter distribution with the density profile of $\rho \propto r^{-2.4}$ beyond the virial radius. It means that the intergalactic space is filled with the tails of halo density profiles. This explains the gap between the global matter density (equation 2.5) and the matter density in and around galaxies (equation 2.4). With this extended matter distribution, the matter entry closes in the mass inventory, which has been left unclosed in Fukugita & Peebles (2004).

Chapter 3

Distribution of Dust around Galaxies: An Analytic Model

3.1 Introduction

How matter is distributed around galaxies is one of the fundamental questions in cosmology. As we discussed in chapter 2, gravitational lensing provides a powerful method to map the matter distribution at small and large length scales. Ménard et al. (2010b, hereafter MSFR in this chapter) measured the mean surface matter density profile of the SDSS main galaxies with the mean redshift $\langle z \rangle = 0.36$ through gravitational lensing magnification of background quasars (QSOs). They calculated the cross-correlation between the number density of foreground galaxies and the flux magnification of background QSOs. The cross-correlation function was then converted to the surface matter density profile Σ_m of the lens galaxies as a function of the projected distance R from the galactic center. The derived profile is well approximated as $\Sigma_m \propto R^{-0.8}$ at $10\text{kpc} \lesssim R \lesssim 10\text{Mpc}$ and well reproduced by cosmological N -body simulation based on the Λ -dominated cold dark matter (ΛCDM) cosmology as we showed in chapter 2.

MSFR also detected the systematic offset among at the five SDSS photometric bands; at shorter wavelengths, QSOs appear less magnified. It is interpreted as reddening due to dust in and around foreground galaxies. Adopting the Small Magellanic Cloud type dust attenuation model for the sample galaxies, they derived the mean surface dust density profile of galaxies $\Sigma_d(R)$ from the galaxy-QSO color cross-correlation function. The shape of the derived Σ_d is very similar to that of Σ_m at $10\text{kpc} \lesssim R \lesssim 10\text{Mpc}$, suggesting that there are a substantial amount of dust in the galactic halos (see also Chelouche et al. 2007; McGee & Balogh 2010). Theoretical models are needed to properly interpret the observationally inferred dust distribution.

In this chapter, we develop an analytic model based on the so-called halo approach to study the distribution of dust around galaxies. In chapter 2 (see also Masaki et al. 2012a), we used cosmological N -body simulations to study in detail the matter

distribution around galaxies. There, we showed that the observed surface density profile can be used to determine the characteristic mass of the sample lens galaxies, and that the contribution of the mass distributed beyond the galaxies' virial radii is approximately about a half of the global mass density. We provide a physical model for the dust distribution in this chapter. Our model is characterized by two key parameters; one is the host halo mass of galaxies and the other is the extent of dust distribution. The former is determined from the observed matter profile (e.g., Mandelbaum et al. 2006a; Hayashi & White 2008; Leauthaud et al. 2012; Masaki et al. 2012a), while the latter can be inferred from the dust distribution. How far dust is transported from the galaxies is indeed an interesting question. The observed dust profile is well described by a single power law over a wide range of distance of from 10kpc to 10Mpc. We show that the profile is decomposed into two parts, the so-called one-halo and two-halo terms. We parametrize the one-halo term such that dust is distributed to αR_{vir} where R_{vir} is the galaxy's virial radius. Through the model fitting, we constraint the extension parameter α to be greater than unity. We discuss the implication for the dust production and transport mechanism into intergalactic space.

3.2 The model

3.2.1 Halo approach

We present a simple formulation to calculate the surface dust density profile. Our model is based on the so-called halo approach (Seljak 2000; Cooray & Sheth 2002). The mean surface density $\Sigma_d(R)$ is divided into two terms:

$$\Sigma_d(R) = \Sigma_d^{\text{1h}}(R) + \Sigma_d^{\text{2h}}(R), \quad (3.1)$$

where R is the distance in the projected two-dimensional plane. The one-halo term $\Sigma_d^{\text{1h}}(R)$ arises from the central halo, and the two-halo term $\Sigma_d^{\text{2h}}(R)$ from the neighbouring halos. In this chapter, the subscript “d” denotes dust.

The contribution from an individual galaxy halo with mass M_{vir} to the one-halo term $\Sigma_d^{\text{1h}}(R)$ is given by the projection of the halo dust density profile $\rho_d(r|M_{\text{vir}})$ along the line-of-sight χ :

$$\Sigma_d(R|M_{\text{vir}}) = \int_{-\infty}^{\infty} d\chi \rho_d(r = \sqrt{\chi^2 + R^2} | M_{\text{vir}}). \quad (3.2)$$

The one-halo term is then a number-weighted average of $\Sigma_d(R|M_{\text{vir}})$

$$\Sigma_d^{\text{1h}}(R) = \frac{1}{n_{\text{halo}}} \int_{M_{\text{min}}}^{\infty} dM_{\text{vir}} \frac{dn}{dM_{\text{vir}}} \Sigma_d(R|M_{\text{vir}}), \quad (3.3)$$

$$n_{\text{halo}} = \int_{M_{\text{min}}}^{\infty} dM_{\text{vir}} \frac{dn}{dM_{\text{vir}}}, \quad (3.4)$$

where dn/dM_{vir} is the halo mass function and M_{min} is the threshold halo mass for the sample galaxies. The threshold mass corresponds to the typical host halo mass of the observed galaxies.

We calculate the two-halo term power spectrum $P_{\text{d}}^{2\text{h}}(k)$ as follows:

$$\begin{aligned} P_{\text{d}}^{2\text{h}}(k) &= P_{\text{lin}}(k) \\ &\times \left[\frac{1}{\bar{\rho}_{\text{d}}} \int_0^\infty dM_{\text{vir}} \frac{dn}{dM_{\text{vir}}} M_{\text{d}}(M_{\text{vir}}) b(M_{\text{vir}}) u_{\text{d}}(k|M_{\text{vir}}) \right] \\ &\times \left[\frac{1}{n_{\text{halo}}} \int_{M_{\text{min}}}^\infty dM_{\text{vir}} \frac{dn}{dM_{\text{vir}}} b(M_{\text{vir}}) u_{\text{d}}(k|M_{\text{vir}}) \right], \end{aligned} \quad (3.5)$$

where $\bar{\rho}_{\text{d}}$ is the mean cosmic dust density, $P_{\text{lin}}(k)$ is the linear matter power spectrum, $b(M_{\text{vir}})$ is the halo bias factor, $M_{\text{d}}(M_{\text{vir}})$ is dust mass in and around a halo with mass M_{vir} , and $u_{\text{d}}(k|M_{\text{vir}})$ is the Fourier transform of the density profile ρ_{d} normalized by its dust mass. The power spectrum is converted to the two-point correlation function via

$$\xi_{\text{d}}^{2\text{h}}(r) = \frac{1}{2\pi^2} \int_0^\infty dk k^2 \frac{\sin(kr)}{kr} P_{\text{d}}^{2\text{h}}(k). \quad (3.6)$$

Then we obtain the two-halo term of the mean surface density profile

$$\begin{aligned} \Sigma_{\text{d}}^{2\text{h}}(R) &= \bar{\rho}_{\text{d}} \int_{-\infty}^\infty d\chi \xi_{\text{d}}^{2\text{h}}(r = \sqrt{\chi^2 + R^2}) \\ &= 2\bar{\rho}_{\text{d}} \int_R^\infty dr \frac{r \xi_{\text{d}}^{2\text{h}}}{\sqrt{r^2 - R^2}}. \end{aligned} \quad (3.7)$$

We adopt a flat- Λ CDM cosmology, with $\Omega_m = 0.272$, $\Omega_\Lambda = 0.728$, $H_0 = 70.2 \text{ km s}^{-1}$, $n_s = 0.961$ and $\sigma_8 = 0.807$ (Komatsu et al. 2011). We use the code *CAMB* to obtain the linear matter power spectrum (Lewis et al. 2000), and the halo mass function and bias given by Sheth & Tormen (1999) at $z = 0.36$ which is equal to the mean redshift of the galaxy sample used in MSFR.

3.2.2 Dust distribution profile

We assume that the spatial distribution of dust within and around a halo is described as

$$\rho_{\text{d}}(r|M_{\text{vir}}) \propto \frac{1}{r^2} \exp\left(-\frac{r}{\alpha R_{\text{vir}}}\right). \quad (3.8)$$

where R_{vir} is the virial radius. Within the virial radius R_{vir} , the mean internal matter density is $\Delta_{\text{vir}} \times \rho_{\text{crit}}$, where Δ_{vir} is given by Bryan & Norman (1998). Essentially, we assume that the dust distribution follows a singular isothermal sphere (SIS) profile with exponential cut-off at $r = \alpha R_{\text{vir}}$. One of our aims in this chapter is to determine the value of α , i.e., how far dust is distributed from galaxies. Figure 3.1 shows the shape of the dust density profile ρ_{d} for a halo with mass $M_{\text{vir}} = 10^{13} h^{-1} M_\odot$

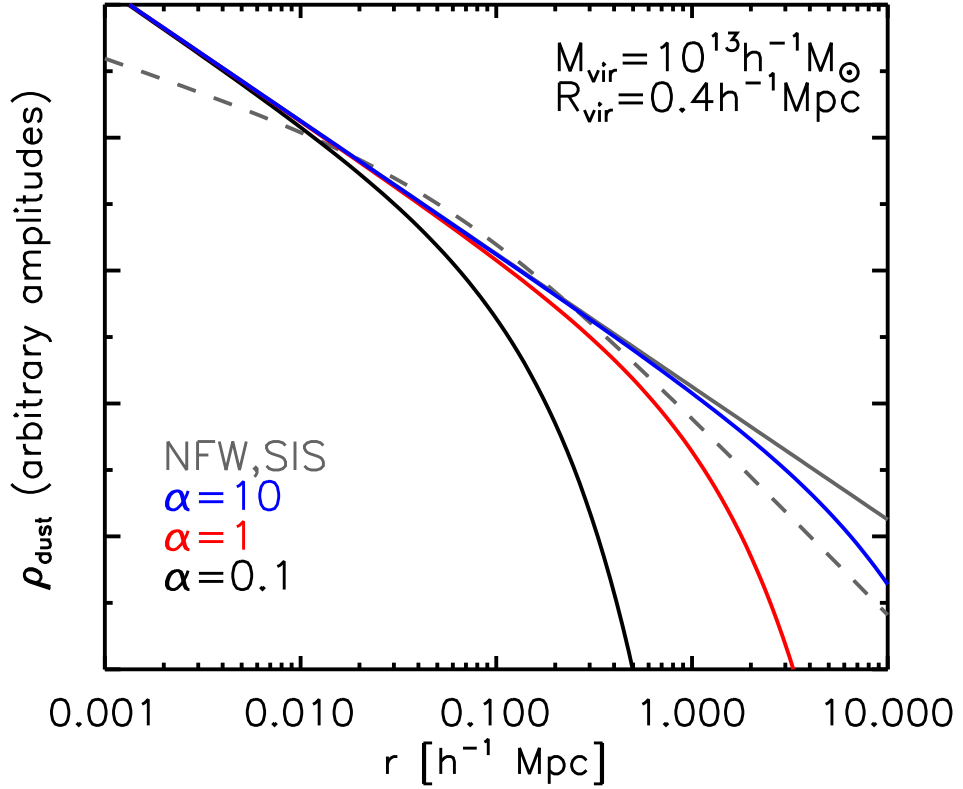


Figure 3.1: The model dust density profile as a function of the spatial distance from the center. The black, red and blue lines represent the model profiles with $\alpha = 0.1, 1$ and 10 , respectively. For comparison, we also show the NFW (Navarro et al. 1997) and the untruncated SIS profiles by grey lines. Note that the amplitudes are arbitrary in this figure.

computed in the above manner. We see the dependence on α clearly.

The power-law shape is motivated by the fact that the observationally derived surface dust profile itself is well fit by a simple power law of $\Sigma_d \propto R^{-0.8}$, similarly to matter distribution (MSFR). Also, detailed calculations of dust ejection and radiation-driven transport by Bianchi & Ferrara (2005) show approximately a power-law distribution for the resulting gas metallicity through dust sputtering. We have also examined other profiles of the form r^{-3} and r^{-1} with a similar exponential cut-off. However, we have found that neither of the steeper or the shallower profile reproduces well the observed dust profile at small distances. We therefore adopt the profile equation (3.8) in our model.

The Fourier transform of $\rho_d(r)$ is given by

$$u_d(k|M_{\text{vir}}) = \int_0^\infty dr 4\pi r^2 \frac{\sin(kr)}{kr} \frac{\rho_d(r|M_{\text{vir}})}{M_d(M_{\text{vir}})}. \quad (3.9)$$

Note that the value of u_d should be unity in small- k limit. We determine the amplitude of ρ_d by setting the halo dust mass associated with a halo to be a certain value M_d . To this end, we first consider the total amount of dust around galaxies in the local universe. Fukugita (2011) estimated the total amount, in units of the cosmic density parameter as,

$$\Omega_{\text{halo dust}} = 4.7 \times 10^{-6}. \quad (3.10)$$

Interestingly, this value is close to the difference between the estimated amount of dust produced and shed by stars over the age of the universe and the summed amount found in local galactic discs (see also Inoue & Kamaya 2003). Suppose that the comoving density of the total halo dust remains constant in the local universe. Then the mean cosmic density of dust in galactic halos is given by

$$\bar{\rho}_d(z) = \Omega_{\text{halo dust}} \rho_{\text{cr}}(z)(1+z)^3. \quad (3.11)$$

We set the dust mass associated with a halo to be

$$\int_0^\infty dr 4\pi r^2 \rho_d(r|M_{\text{vir}}) = M_d = \Gamma \times M_{\text{vir}} \quad (3.12)$$

where Γ is the dust-halo mass ratio. We integrate the dust mass weighted by the halo mass function to obtain the global dust density. We normalize ρ_d , or equivalently Γ , by matching the global dust density to equation (3.11). Note that Γ is not necessarily a constant but can be a function of halo mass.

Dust-halo mass ratio Γ

An essential physical quantity in our model is the dust-halo mass ratio Γ in equation (3.12). We propose two simple models. The first one is *constant model*, i.e., Γ is independent of halo mass. The dust-halo mass ratio is simply the global density ratio

$$\Gamma = 1.73 \times 10^{-5} = \Omega_{\text{halo dust}}/\Omega_m. \quad (3.13)$$

Because the heavy elements that constitute dust are produced by stars, it may be reasonable to expect that the dust mass is proportional to the stellar mass. Intriguingly, Takeuchi et al. (2010) used data of *AKARI* and *GALEX* to show a moderate correlation between the stellar mass and dust attenuation indicator for the sample galaxies (see their Figure 16). In our second model, we consider the observed galaxy stellar-halo mass relation to model the halo mass dependence of Γ . We call the model *mass dependent model*. Leauthaud et al. (2012) recently studied the stellar-halo mass relation from the joint analysis of galaxy-galaxy weak lensing, galaxy clustering and galaxy number densities using the COSMOS survey data. We

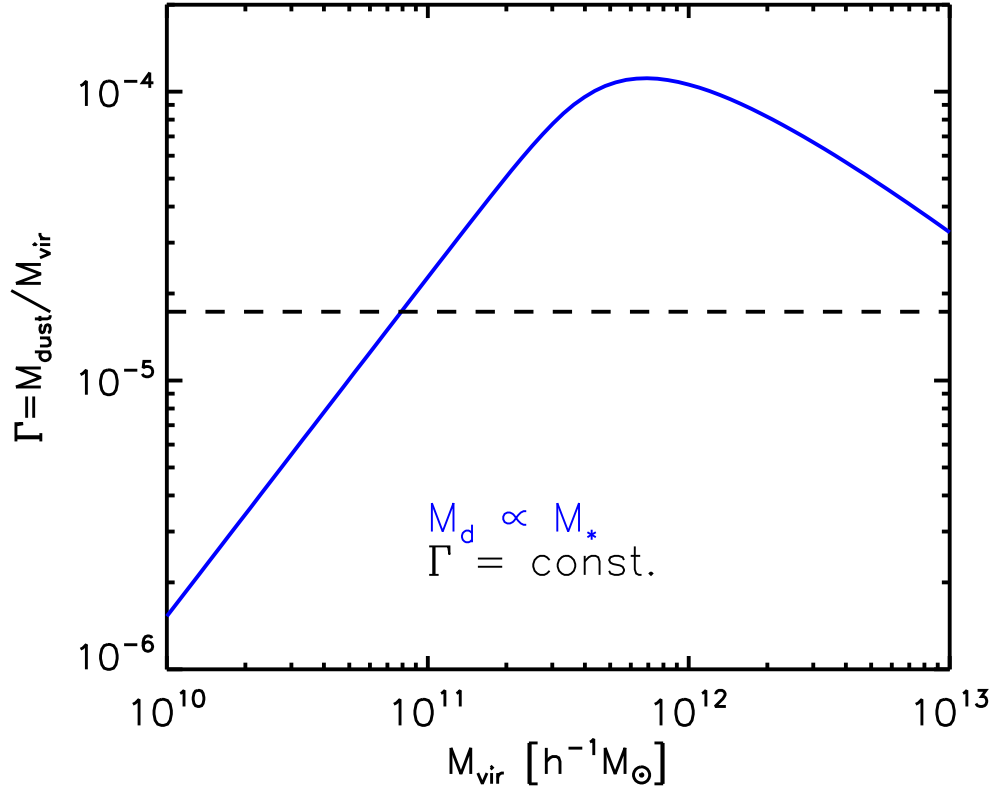


Figure 3.2: Two models for dust-halo mass ratio as a function of halo mass. The dashed and the solid lines are the ratio Γ for the constant and the mass dependent model, respectively.

use their functional form with the best fit parameters at $z \approx 0.37$,

$$\begin{aligned} \log_{10}(M_{\text{vir}}) = & \log_{10}(M_1) + \beta \log_{10} \left(\frac{M_*}{M_{*,0}} \right) \\ & + \frac{(M_*/M_{*,0})^\delta}{1 + (M_*/M_{*,0})^{-\gamma}} - 0.5, \end{aligned} \quad (3.14)$$

where M_* is the galaxy stellar mass, $\log_{10}(M_1/M_\odot) = 12.52$, $\log_{10}(M_{*,0}/M_\odot) = 10.92$, $\beta = 0.46$, $\delta = 0.57$, and $\gamma = 1.5$ (see also Behroozi et al. 2010). We then relate the dust mass to the stellar mass as

$$M_d(M_{\text{vir}}) \propto M_*(M_{\text{vir}}). \quad (3.15)$$

The normalization constant is determined to be 3.05×10^{-3} by integrating this equation weighted by the halo mass function. The global dust mass density thus calculated is matched to equation (3.11).

Figure 3.2 compares Γ for our two models. The shape of Γ for the mass-dependent

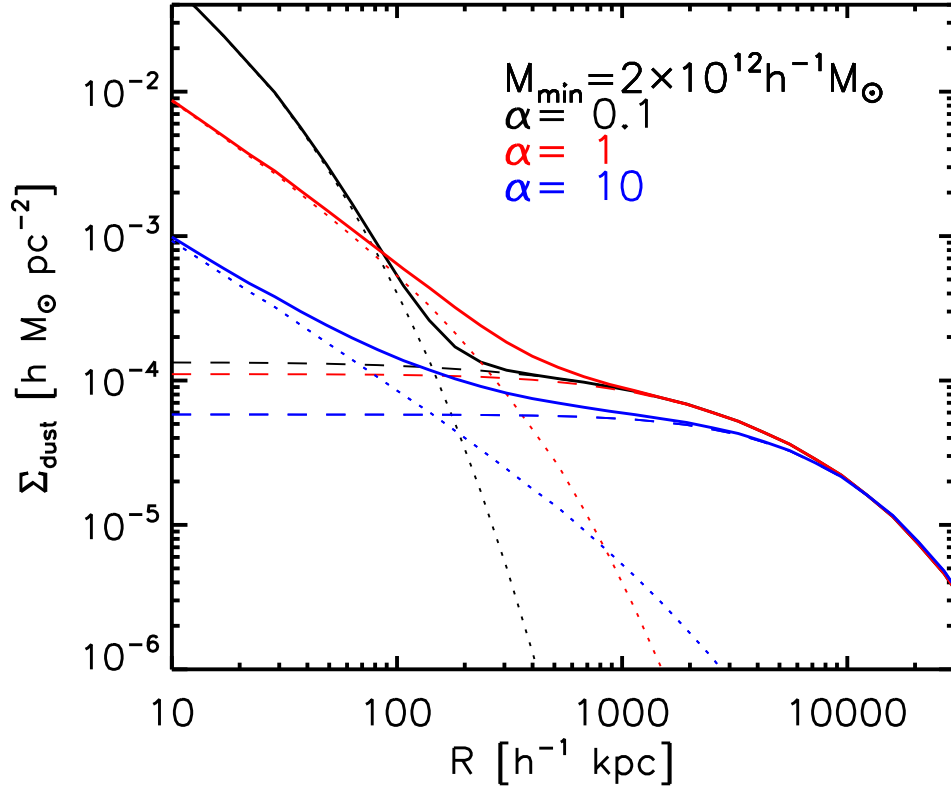


Figure 3.3: The surface dust density profile as a function of the projected radius for $\alpha = 0.1, 1$ and 10 . The projected radius is the physical distance at $z = 0.36$. The constant model for dust-halo mass ratio is adopted. The dotted and the dashed lines represent the one-halo and the two-halo terms, respectively. The solid lines show the sum of the two terms.

model reflects the stellar-halo mass relation. The peak value of Γ at $\sim 6 \times 10^{11} h^{-1} M_{\odot}$ is $\simeq 10^{-4}$. Overall, Γ for the mass dependent model is larger than that for the constant model at the characteristic mass of the sample galaxies (see Section 3.3).

We are now able to calculate the dust surface density profile. In Figure 3.3, we show the dependence of the surface dust density profile on the extension parameter α . For this figure, the threshold halo mass is fixed to be $2 \times 10^{12} h^{-1} M_{\odot}$. We compare three cases; $\alpha = 0.1, 1$ and 10 . The dotted lines show the one-halo term. Clearly the extension parameter α affects significantly the amplitude and the shape of the one-halo term. The central surface density is larger for smaller α . This can be easily understood by noting the total dust mass associated with a halo is given by equation (3.12). On the other hand, α does not affect much the two-halo term at $R \gtrsim 1 \text{ Mpc}$. The amplitude of the two-halo term is essentially set by the halo bias $b(M_{\text{vir}})$ (see equation [3.5]).

3.3 Results

We fit our dust distribution model to the observed surface dust density by the least chi-square minimization. We have two physical parameters, M_{\min} and α , in our model. We found that the parameters were constrained poorly when both of them were set to be free. Because M_{\min} is already estimated to be $2 \times 10^{12} h^{-1} M_{\odot}$ in chapter 2 (Masaki et al. 2012a) through a detailed comparison of the observed matter distribution with the results of N -body simulations, it is sensible to fit our dust distribution model by treating only α as a free parameter. Namely, the characteristic halo mass can be determined by the gravitational lensing measurement of the matter distribution, whereas the dust distribution extension can be inferred from the observed dust profile.

We evaluate the likelihood of the specific model by the χ^2 value of the model fit to the observed quantities. The obtained best-fit α for the constant and the mass dependent models are, respectively,

$$\alpha = 1.16_{-0.155}^{+0.203} (1\sigma) \text{ for constant model,} \quad (3.16)$$

$$\alpha = 2.88_{-0.355}^{+0.450} (1\sigma) \text{ for mass dependent model.} \quad (3.17)$$

Figure 3.4 shows the best-fit dust profile of the constant model with $\alpha = 1.16$ and that of the mass dependent model with $\alpha = 2.88$. The data points are from MSFR. Both models for Γ reproduce the observed profile fairly well. It is interesting to compare these two equally good models. The mass dependent model requires a larger α , which is owing to the difference in the typical value of Γ for the two models. At $M_{\text{vir}} > 10^{11} h^{-1} M_{\odot}$, Γ of mass dependent model is higher than that of constant model. Because the one-halo term is largely contributed by halos with masses $\sim M_{\min} = 2 \times 10^{12} h^{-1} M_{\odot}$, the best fit α is larger for the mass dependent model to match the observed inner dust surface density profile (see Figure 3.3).

Overall, our simple models reproduce the observed dust profile very well. Intriguingly, both our models suggest $\alpha \sim \mathcal{O}(1)$, i.e., halo dust is distributed over a few hundred kilo parsecs from the galaxies. It is also important that the observed power law surface density $\Sigma_d \propto R^{-0.8}$ at $R = 10 \text{ kpc} - 10 \text{ Mpc}$ can be explained with $\alpha \sim \mathcal{O}(1)$. The apparent large-scale dust distribution is explained by the two-halo contributions. Dust is distributed to/over $\sim R_{\text{vir}}$ from a galaxy, but not necessarily up to 10 Mpc as one might naively expect from the observed dust profile.

It is worth discussing the total dust budget in the universe. The amplitude of the two-halo term depends largely on the mean cosmic density of intergalactic dust, $\bar{\rho}_d$ in equation (3.7)¹. The excellent agreement at large separation between the observed dust density profile and our model prediction shown in Figure 3.4 implies that $\Omega_{\text{halo dust}}$ should be $\sim 10^{-6}$. Clearly, a significant amount of dust exists around

¹The halo bias $b(M_{\text{vir}})$ is also a critical factor. However, the characteristic halo mass, and hence $b(M_{\text{vir}})$, is well constrained from the observed matter density profile, as shown in chapter 2 (Masaki et al. 2012a)

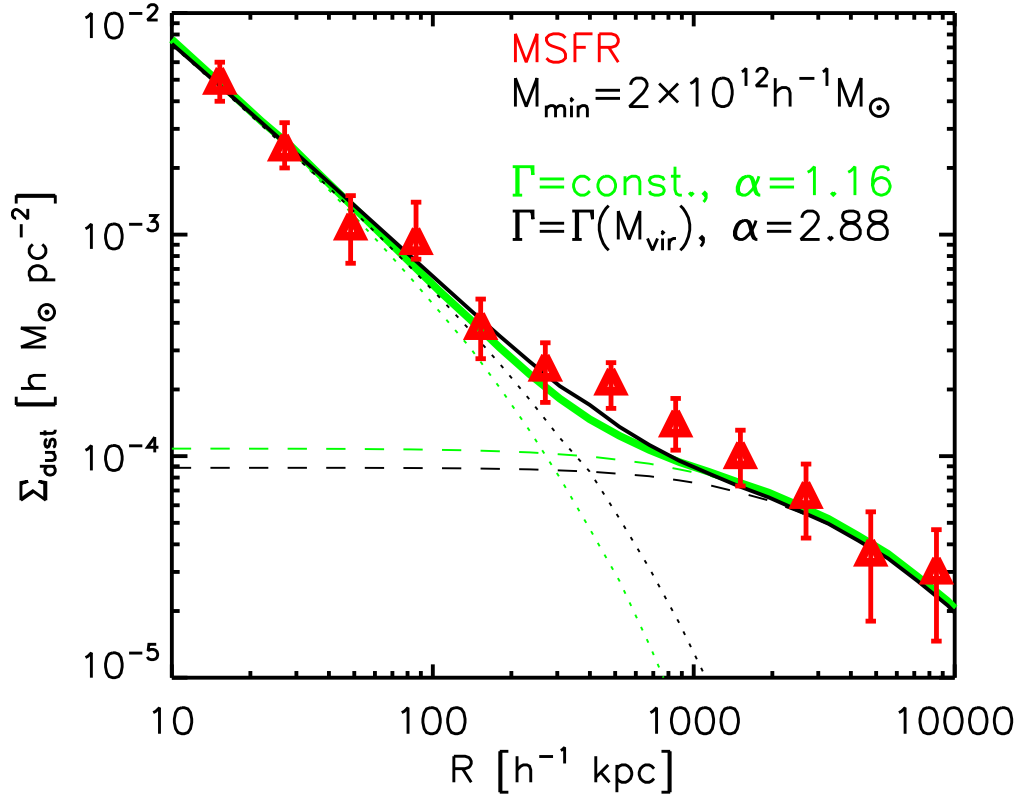


Figure 3.4: The mean surface dust density profile as a function of the physical projected distance from the center of galaxies at $z = 0.36$. The results from our constant model and mass dependent model are shown by the green and the black lines, respectively. The dotted, the dashed and the solid lines are the one-halo, the two-halo and the total, respectively.

the galaxies. Such “halo dust” can close the cosmic dust budget as discussed more quantitatively by Fukugita (2011).

The intergalactic dust could cause non-negligible extinction and thus could compromise cosmological studies with distant supernovae (Ménard et al. 2010a). We calculate the mean extinction by the intergalactic dust following Zu et al. (2011) (see their equation [2]). With our model mean cosmic density of $\Omega_{\text{halo dust}} = 4.7 \times 10^{-6}$, the predicted mean extinction is $\langle A_V \rangle = 0.0090$ mag up to $z = 0.5$. Such an opacity is not completely negligible even in the current Super Novae surveys, and will become important for future surveys that are aimed at determining cosmological parameters with sub-percent precision (Ménard et al. 2010a).

3.4 Summary and discussion

We have shown that our halo model can reproduce the dust profile around galaxies measured by MSFR. By fitting the model to the observed dust profile, we infer that dust is distributed beyond the virial radius of a galaxy. Several authors proposed radiation-driven transport of dust from galactic discs into intergalactic medium at high redshifts (Aguirre et al. 2001; Bianchi & Ferrara 2005). Zu et al. (2011) showed that galactic winds can disperse dust into the inter-galactic medium efficiently. Such studies generally suggest that dust can travel up to a few $\times 100$ kpc from galaxies if the ejection velocity is $\simeq 100 \text{ km s}^{-1}$. The relatively larger extent radius of dust for our mass dependent model requires very efficient transport mechanisms. Note also that the dust must survive on its way through the galactic halos. Dust in a large, group-size halo could be destroyed by the thermal sputtering in hot gas (Bianchi & Ferrara 2005; McGee & Balogh 2010). Clearly, detailed theoretical studies on dust transport are needed.

Fluctuations of the cosmic infrared background (CIB) provide insight into dust distribution around galaxies (e.g., Viero et al. 2009; Amblard et al. 2011). Viero et al. (2009) used BLAST data to measure the CIB power spectrum. Using a halo approach, they found that the observed power spectrum at small angular scales is reproduced if halo dust extends up to a few times of the virial radius of galactic halos. It is remarkably consistent with our conclusion in this chapter. Amblard et al. (2011) compared their measurements of the CIB anisotropies from Herschel wide-area surveys with Viero et al. (2009). Two power spectra are consistent with each other at small scales. Our dust distribution model may provide a key element for studies on the CIB.

Although our model reproduces the observed dust profiles very well, a few improvements can be certainly made. The dust extension α and the dust-halo mass ratio Γ are likely to depend on the halo mass and galaxy type, etc. (McGee & Balogh 2010). One may need to consider the distribution of satellite galaxies within a halo by using, for example, the halo occupation distribution (HOD). Indeed, we see slight discrepancies between the model predictions and the observation in the dust profiles

at $\sim 1\text{Mpc}$ (Figure 3.4), where the contribution from satellite galaxies are non-negligible (for more detailed modeling, see e.g., Leauthaud et al. 2012). In principle, the HOD parameters can be inferred from the lensing magnification measurement presented by MSFR. However, in order to derive the parameters accurately, one needs to use additional information from observations of the galaxy-galaxy correlation function (Leauthaud et al. 2012). Including these effect in our model is beyond the scope of this work, but will be needed in order to interpret data from future wide-field galaxy surveys.

Chapter 4

Modeling Color-Dependent Galaxy Clustering in Cosmological Simulations

4.1 Introduction

Describing galaxy formation and evolution within the context of the standard cosmology is one of the most important goals in astronomy and cosmology. Large data from recent galaxy redshift surveys, such as the Sloan Digital Sky Survey (SDSS; York et al. 2000), have enabled us to measure precisely various statistics for subsamples of the galaxies classified by, for example, luminosity, stellar mass, morphology and so on (e.g., Li et al. 2006; Zehavi et al. 2011). The upcoming deep and wide-area galaxy surveys, e.g., Subaru Hyper Suprime-Cam Survey¹ and Dark Energy Survey², will provide even larger data of distant galaxies. Clearly, accurate theoretical models are needed to interpret observational results such as those on the relationship between galaxies and dark matter (DM) halos.

So far, several useful phenomenological methods to link halos with galaxies have been developed. One is the so-called halo occupation distribution (HOD) modeling (see e.g., Seljak 2000; Cooray & Sheth 2002; Tinker et al. 2005; Blake et al. 2008; Zehavi et al. 2011; Leauthaud et al. 2012). The method parametrizes HOD, i.e., occupation number of galaxies per halo, of central and satellite galaxies separately, as a function of halo mass. The functional form of HOD is inspired by hydrodynamical cosmological simulations or by semi-analytic models (Zheng et al. 2005). By using the halo mass function as well as the bias factor and the DM density profile obtained from cosmological N -body simulations, one can easily calculate the galaxy two-point correlation functions.

There are free parameters in the HOD formalism which are constrained by matching to the observed clustering and to the number density of galaxies (Blake et al.

¹<http://subarutelescope.org/Projects/HSC/> and <http://sumire.ipmu.jp/en/>

²<http://www.darkenergysurvey.org/>

2008; Zehavi et al. 2011; Coupon et al. 2012). More sophisticated treatments of HOD include the conditional luminosity functions (van den Bosch et al. 2003; Cooray 2006). An attractive feature of HOD is that it can be extended to model and calculate other statistical quantities than galaxy clustering (e.g., chapetr 3; De Bernardis & Cooray 2012; Leauthaud et al. 2012; van den Bosch et al. 2012). However, it is known that one often encounters difficulty in fitting HOD model predictions to the observed clustering and the number density simultaneously (Quadri et al. 2008; Matsuoka et al. 2011; Wake et al. 2011).

The second method is called the subhalo abundance matching (SHAM) (Kravtsov et al. 2004; Tasitsiomi et al. 2004; Conroy et al. 2006; Guo et al. 2010; Moster et al. 2010; Wetzel & White 2010; Neistein et al. 2011; Trujillo-Gomez et al. 2011; Reddick et al. 2012; Rodríguez-Puebla et al. 2012). SHAM assumes a tight relation between galaxy luminosity (or stellar mass) and subhalo circular velocity (or mass). The threshold circular velocity is set such that the number density of subhalos and that of luminosity-selected galaxies are matched as

$$n_{\text{subhalo}}(> V_{\text{cir}}) = n_{\text{galaxy}}(> L). \quad (4.1)$$

The predicted clustering generally agrees with observations, reproducing the observed luminosity dependence of galaxy clustering. It should be emphasized that SHAM does not need fitting parameters while HOD modeling does. An additional advantage of SHAM is that it can utilize N -body simulation outputs directly. Therefore, SHAM can incorporate the non-linear evolution of galaxy clustering accurately while having a simple and direct galaxy-subhalo connection.

Both the HOD model and SHAM are used to calculate the galaxy two-point correlation or the galaxy-mass cross correlation as a function of a galaxy property, e.g., luminosity and stellar mass. It would be ideal if multiple observable properties are assigned simultaneously to (sub)halos. Galaxy color is one of the most fundamental properties. It is thought to indicate the galaxy's age and the star formation activity. Also it is well-known that there are two apparent sequences in the color-magnitude diagram, which represent red and blue galaxies for optical sample. The two populations differ in many aspects including their spatial clustering, reflecting probably their formation histories. So far, detailed treatments for color-dependent clustering or lensing measurements have been developed, but only within the HOD model (van den Bosch et al. 2003; Cooray 2006; Mandelbaum et al. 2006b; Tinker et al. 2008; Ross & Brunner 2009; Simon et al. 2009; Skibba & Sheth 2009; Zehavi et al. 2011).

In this chapter, we develop a method to assign galaxy color to subhalos by extending SHAM. We first apply SHAM to a subhalo catalog to obtain luminosity-selected subhalo samples. We then divide subhalos in a luminosity bin into two groups by ordering subhalos using a secondary quantity. The two groups are then meant to represent red and blue galaxy samples. Similarly to the original SHAM, the abundance ratio of the divided two groups is matched to the observed red/blue ratio. Clearly, we need to choose an appropriate subhalo property which is presumably

correlated with galaxy colors. We propose two models for the secondary property. One is motivated by the so-called assembly bias whereas the other incorporates environmental effects.

Assembly bias is a property-dependent bias for halos in a fixed mass bin. A variety of properties have been considered so far, such as assembly time, spin, concentration and so on (see e.g., Gao et al. 2005; Wechsler et al. 2006; Croton et al. 2007; Gao & White 2007; Reed et al. 2007; Lacerna & Padilla 2011, 2012). Among these, we choose a subhalo age as a proxy of galaxy color. It is thought that there is some environmental effect through which a galaxy’s morphology and color evolve. Gerke et al. (2012) recently developed a model to assign color to subhalos (see also Tasitsiomi et al. 2004). In their model, color is assigned to subhalos by using local galaxy density along with the empirical color-galaxy density relation (e.g., Hogg et al. 2004; Balogh et al. 2004; Bamford et al. 2009). Our second model is motivated by their approach, but we do not use such an empirical relation.

Finally, we consider lensing measurements in addition to galaxy clusterings in order to distinguish the two models. Lensing observations will provide an independent information which possibly allows us to derive an accurate galaxy-halo connection. In particular, we utilize the observed early/late-type dependent lensing profile (Mandelbaum et al. 2006b) assuming early/late-type galaxies approximately correspond to red/blue galaxies. We show, for the first time, that an extended SHAM can reproduce the observed lensing profiles as well as the color-dependent galaxy clusterings in the local universe.

4.2 Setup

4.2.1 Cosmological N -body simulations

We use the massively parallelized code *Gadget-2* (Springel et al. 2001b; Springel 2005) in its Tree-PM mode to run two cosmological N -body simulations. For each run, the assumed Λ -cold-DM cosmology is consistent with the *WMAP* 7-year results, with $\Omega_m = 0.272$, $\Omega_b = 0.0441$, $\Omega_\Lambda = 0.728$, $H_0 = 100h = 70.2 \text{ km s}^{-1} \text{ Mpc}^{-1}$, $\sigma_8 = 0.807$ and $n_s = 0.961$ in the standard notation (Komatsu et al. 2011). The two runs, one with $200 h^{-1} \text{ Mpc}$ on a side and the other with $300 h^{-1} \text{ Mpc}$ box size, both employ 1024^3 DM particles, and will be referred to as L200 and L300, respectively. The resulting mass of a particle is $5.6 \times 10^8 h^{-1} M_\odot$ ($1.9 \times 10^9 h^{-1} M_\odot$) for the L200 (L300) run. We use the code *CAMB* (Lewis et al. 2000) to obtain the matter power spectrum for the initial condition. We set the initial redshift to be 49 (65) for the L200 (L300) run. The gravitational softening length is set to be $5 h^{-1} \text{ kpc}$ and $8.8 h^{-1} \text{ kpc}$ for the L200 and the L300 run, respectively. The L300 run has lower mass and spatial resolution than the L200 run but provides higher statistical precision of correlation functions for massive objects and at the large scale.

4.2.2 Identification of halos, tracking assembly history and construction of subhalo catalog

We identify the distinct halos, i.e., halos that do not lie in more massive halos, using the friends-of-friends (FoF) algorithm with linking parameter of 0.2 in units of the mean interparticle separation. For the identification of subhalos, i.e., dense self-gravitating clumps that reside in a distinct halo, we utilize the *SubFind* algorithm developed by Springel et al. (2001a). The algorithm decomposes a distinct halo into a central subhalo, i.e., the so-called smooth component which contains the majority of mass, and satellite subhalos. We store the subhalos with more than 20 particles.

To implement SHAM, we construct the subhalo catalog with $V_{\text{max}}^{\text{acc}}$ for the satellite subhalos, where $V_{\text{max}}^{\text{acc}}$ is the maximum value of particle circular velocity $V_{\text{cir}}(r) = \sqrt{GM(< r)/r}$ at the last epoch when the satellite subhalo was a central one (Conroy et al. 2006). We follow the recipe described in detail by Allgood (2005) to construct the mass assembly history of the most massive progenitor of subhalos. We use 50 simulation snapshots taken evenly in $\ln(1+z)$ from $z = 10$ to $z = 0$ for the two simulations. For the central subhalos, we tabulate the maximum circular velocity at the redshift when they are *observed*, $V_{\text{max}}^{\text{now}}$. The term V_{cir} in equation (4.1) is replaced with $V_{\text{max}}^{\text{now}}$ for the central subhalos and $V_{\text{max}}^{\text{acc}}$ for the satellite subhalos. Note that the circular velocity defined in this way is a direct proxy of gravitational potential and is less sensitive to subhalo identification algorithms.

4.2.3 Application of SHAM

Following Zehavi et al. (2011), we consider galaxies in three magnitude bins, $-22 < M_r - 5 \log_{10} h < -21$, $-21 < M_r - 5 \log_{10} h < -20$ and $-20 < M_r - 5 \log_{10} h < -19$, and hereafter denote the absolute magnitude just as M_r without the $-5 \log_{10} h$ term. We apply SHAM to the subhalo catalogs constructed in the L200 and L300 runs to create the magnitude-binned subhalo samples. We take the bracketing threshold samples for a bin and then use the difference of them as a binned sample. The comoving number density for each threshold sample can be found in Zehavi et al. (2011).

We measure the projected correlation function w_p as a function of the projected distance R as

$$w_p(R) = 2 \int_0^{\pi_{\text{max}}} d\pi \xi(r = \sqrt{\pi^2 + R^2}). \quad (4.2)$$

We take the same value of π_{max} used by Zehavi et al. (2011) for each bin. For the fainter and the intermediate samples we use the L200 subhalo catalog at $z = 0$. Only for the brighter sample, we use the catalog from the L300 run at $z = 0.1$. The chosen redshift is very close to the mean redshift of each magnitude binned galaxy sample. The results are compared with Zehavi et al. (2011) in Figure 4.1. The top panel shows fairly nice agreements between SHAM and the observation, as expected from previous works (Conroy et al. 2006; Trujillo-Gomez et al. 2011).

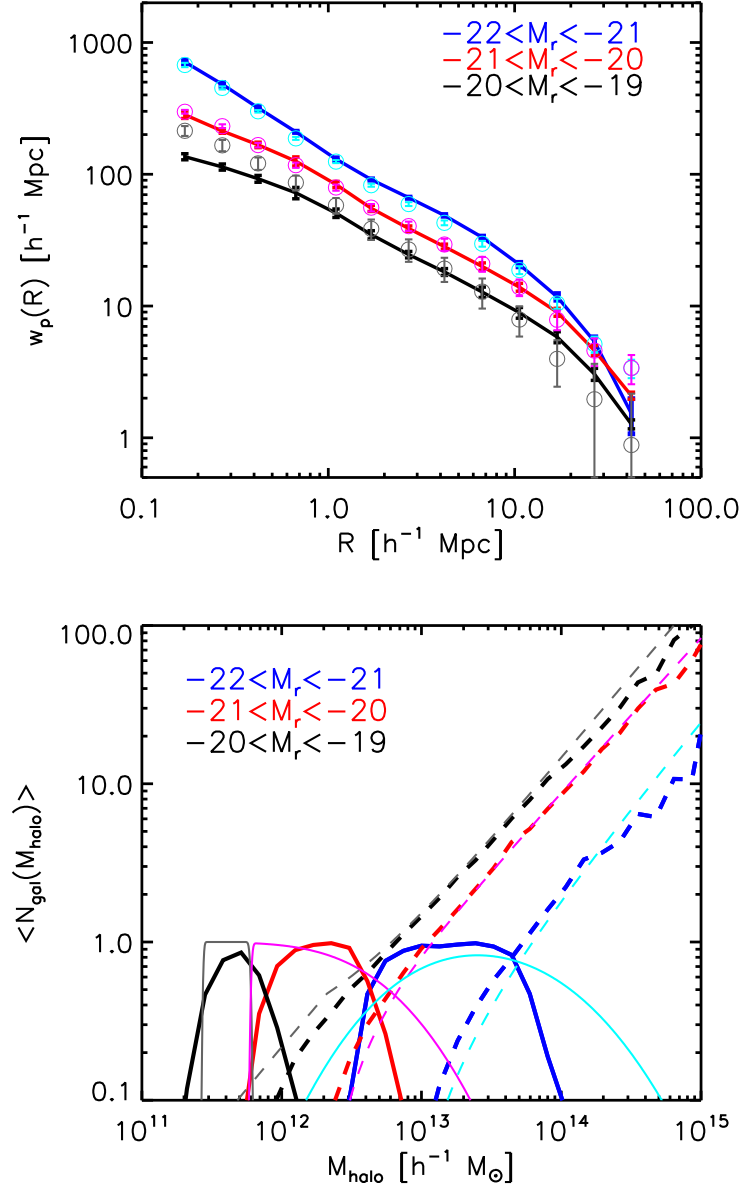


Figure 4.1: Top: The projected correlation functions for the magnitude-binned samples. The SHAM predictions are shown by solid lines with error bars taken from the jack-knife resampling of eight subvolumes. The SDSS results (Zehavi et al. 2011) are shown by open circles with error bars. The amplitudes of the brightest and the faintest sample are shifted upward and downward by 0.1 dex for clarity. Bottom: HODs for each binned sample obtained by SHAM (the thick lines). For comparison, the best-fit models of HOD modeling (Zehavi et al. 2011) are shown by pale color thin lines. The solid and the dashed lines are HODs of central and satellite galaxies. Note that we quote the FoF mass as the distinct halo mass while the HOD modeling uses the virialized mass. Hence our HODs should be shifted to the left hand side slightly to be compared with the HOD fitting results.

We found that SHAM overpredicts the amplitude for the brightest sample by about 10% at all scales. This may be because we do not include scatter in the $V_{\text{max}} - M_r$ relation. In reality, scatter between the two quantities is expected. It has been pointed out that introducing scatter reduces the clustering amplitude, in particular for the brighter sample effectively, and makes the agreement better (Wetzel & White 2010; Trujillo-Gomez et al. 2011; Reddick et al. 2012).

We show the HODs obtained for each binned sample in the bottom panel and compare them with the best-fit HOD modeling results estimated by Zehavi et al. (2011). We consider the galaxies assigned to the central and satellite subhalos as the central and satellite galaxies, respectively. The figure shows that the HODs of satellite galaxies of SHAM agree with the best-fit HOD model well. The figure also shows that the HODs of central galaxies from SHAM are narrower than the HOD modeling for the bright and intermediate samples. It should be noted that both HOD modeling and SHAM give very similar predictions for galaxy clustering.

4.3 Method for color assignment

Here we describe our method to assign galaxy color to subhalos. SHAM uses the abundance as a function of subhalo and galaxy properties to match their number densities. SHAM works well if the properties, e.g., galaxy luminosity and the subhalo maximum circular velocity, highly correlate with each other (Conroy et al. 2006; Neistein et al. 2011; Reddick et al. 2012). The spirit of our method is also based on this insight. We separate each luminosity-binned subhalo catalog into two groups by a secondary subhalo property. The secondary property is expected to be correlated well with galaxy color. Then the two groups correspond to the red and blue galaxies within the luminosity bin. In a fashion similar to SHAM, the number density ratio of the two subhalo groups is matched with the observed red/blue galaxy abundance ratio. We study two models for the secondary subhalo property: one is motivated by assembly bias (e.g., Gao et al. 2005; Wechsler et al. 2006; Croton et al. 2007; Gao & White 2007; Reed et al. 2007; Lacerna & Padilla 2011) while the other incorporates environment in and around subhalos. We discuss our two models below.

4.3.1 Models for a proxy of galaxy color

Subhalo age

It is naive but natural to consider that the galaxy color is a proxy of the galaxy age and to expect that subhalo age is highly correlated with the age of the galaxy³. We use the redshift evolution of the maximum circular velocity to define the formation epoch z_{form} of subhalos via

$$V_{\text{max}}(z = z_{\text{form}}) = f \times V_{\text{max}}, \quad \text{with } 0 < f < 1 \quad (4.3)$$

³For simplicity, we do not consider bias in age due to starburst triggered by mergers.

where V_{\max} on the right hand side is V_{\max}^{acc} for the satellite subhalos and V_{\max}^{now} for the central subhalos at $z = 0$ or 0.1 , depending on the simulation box. Note that z_{form} of the satellite subhalos is defined at an earlier epoch than the accretion epoch. In practice, we identify the two snapshots between which $f \times V_{\max}$ is located and then we interpolate linearly between them to get z_{form} . For low mass subhalos or small values of f , we cannot follow down to $f \times V_{\max}$ due to the lack of mass resolution. In such cases, we define the redshift at which the subhalo is identified for the first time as z_{form} .⁴ We refer to this model as the *age model*. In this model, the subhalos with higher z_{form} correspond to redder galaxies. It has been shown extensively in the literature that the older distinct halos are more clustered than the younger ones (Gao et al. 2005; Gao & White 2007; Reed et al. 2007; Lacerna & Padilla 2011).

The choice of value of f is not unique. We find that the predicted correlation function depends on the value of f . We show the impact of f in the age model in Figure 4.2. For example, we show models with $f = 0.9, 0.8$ and 0.6 for the $-21 < M_r < -20$ sample. For the fainter and brighter samples, very similar trends are found. The red and the blue lines represent w_p or HOD for the subhalos with higher- and lower- z_{form} , respectively. As we expect, a “split” like the red/blue galaxy separation is seen in the correlation function (top panel). Furthermore, larger value of f gives larger split. This can be understood as the larger f value captures subhalos which formed at earlier epoch. Hence the predicted clustering for red galaxies is enhanced. In the bottom panel, HODs are shown. The peaks at $M_{\text{halo}} \simeq 2 \times 10^{12} h^{-1} M_{\odot}$ are HODs of central galaxies and the power law-like curves at high halo mass regime are HODs of satellite galaxies. It can be seen that the satellite HOD is more sensitive to f than the central HOD.

Local DM density around subhalos

As our second model, we adopt the local DM density around subhalos as the secondary subhalo property. Mandelbaum et al. (2006b) showed that early type galaxies have higher mass density profile than late type ones at $z = 0 \sim 0.1$ in several magnitude bins via galaxy-galaxy lensing techniques. In particular, this morphology dependence of mass density profile is more apparent at $R \gtrsim 100 h^{-1} \text{kpc}$. This suggests that redder galaxies tend to be hosted by subhalos with higher density envelope than bluer ones.

We take a sphere with radius of R_{DM} centered on the center of a subhalo to measure the local DM density. In this model, the subhalos with higher local density corresponds to the redder galaxy populations. We take the sphere radius of $\sim \mathcal{O}(100 h^{-1} \text{kpc})$ to reflect our motivation from the lensing study. It should be noted that this property is less affected by simulation resolution than the age model. We refer to this model as the *local density model*.

⁴As we will see later, high values of $f \simeq 0.9$ are preferred to fit the observed clustering. For such f , the formation epochs of almost all subhalos are identified later than the first identified epoch even for the faint sample.

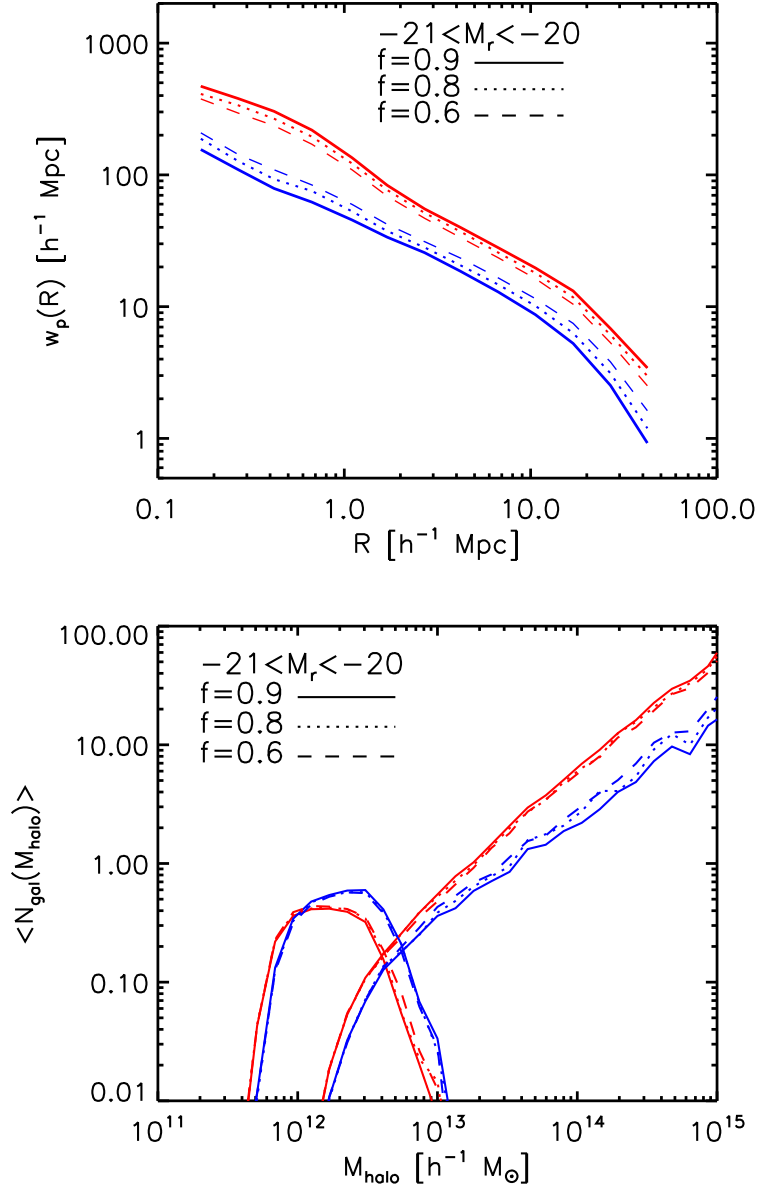


Figure 4.2: Impact of the adopted f value (see Equation [4.3]) on the clustering and HOD in the age model. The red and the blue lines show w_p or HOD for the subhalo subsamples with higher- and lower- z_{form} . The adopted values of f are 0.9, 0.8 and 0.6. Top: Projected correlation functions from the age model. Bottom: HODs of central and satellite galaxies as a function of host halo mass.

Similar to the age model, we find that the predicted correlation function depends on the size of a sphere, R_{DM} . Figure 4.3 illustrates the impact of R_{DM} in the local density model. The adopted sphere sizes in the figure are $R_{\text{DM}} = 500, 300$ and $200 h^{-1}\text{kpc}$. Again, the predictions for the $-21 < M_r < -20$ sample are shown. The red and the blue lines are w_p or HOD for the subhalos with higher and lower local DM density, respectively. The top panel shows that clustering amplitudes for the subhalos with higher local density are higher than those for the subhalos with lower density as we expect. The panel also shows that the color split is larger for larger- R_{DM} . These are because that counting simulation particles in a sphere with radius of $\gtrsim 100 h^{-1}\text{kpc}$ leads subhalos in massive halos (i.e., cluster or groups sized halos) to be ones with higher local density. This trend is more effective for larger- R_{DM} as shown in the HOD (bottom panel). The bottom panel shows that the red central galaxies are assigned to higher mass distinct halos than the blue central galaxies. This is because that our local density measure strongly traces subhalo mass or host distinct halo mass itself for central subhalos.

4.4 Results

4.4.1 Color dependence of projected correlation functions

Comparison with observations

We compare our model predictions for the color dependence of clustering with the observational results by Zehavi et al. (2011). They separate the red and blue galaxies in the $(g - r) - M_r$ color-magnitude space with the division

$$(g - r) = 0.21 - 0.03M_r. \quad (4.4)$$

For each magnitude bin, we search the model with the lowest value of $\chi^2 = \chi_{\text{red}}^2 + \chi_{\text{blue}}^2$, where χ_{red}^2 and χ_{blue}^2 are chi-square values for fits to the red and the blue galaxy correlation functions.

In the age model, we take eight values of $f = 0.6, 0.65, 0.7, 0.75, 0.8, 0.85, 0.9$ and 0.95 . For the intermediate sample, $-21 < M_r < -20$, we find that $f = 0.9$ gives the least χ^2 . We find that, for the fainter and brighter samples, the model with $f = 0.95$ is the best model. The best model results for each sample are shown by thick solid lines in Figure 4.4. The red and the blue lines with error bars represent the predicted w_p for the red and the blue galaxies, respectively. The error bars are taken from jack-knife subsampling with eight subvolumes. Data points with error bars show the observational results taken from Zehavi et al. (2011).

As shown in Figure 4.4, our age model reproduces the observed color-dependent clusterings very well. The values are relatively high but not surprising since the time evolution of the maximum circular velocity is slower than mass evolution. For the Milky-Way sized distinct halo, z_{form} with $f = 0.95$ corresponds to $z \simeq 1 - 2$ on

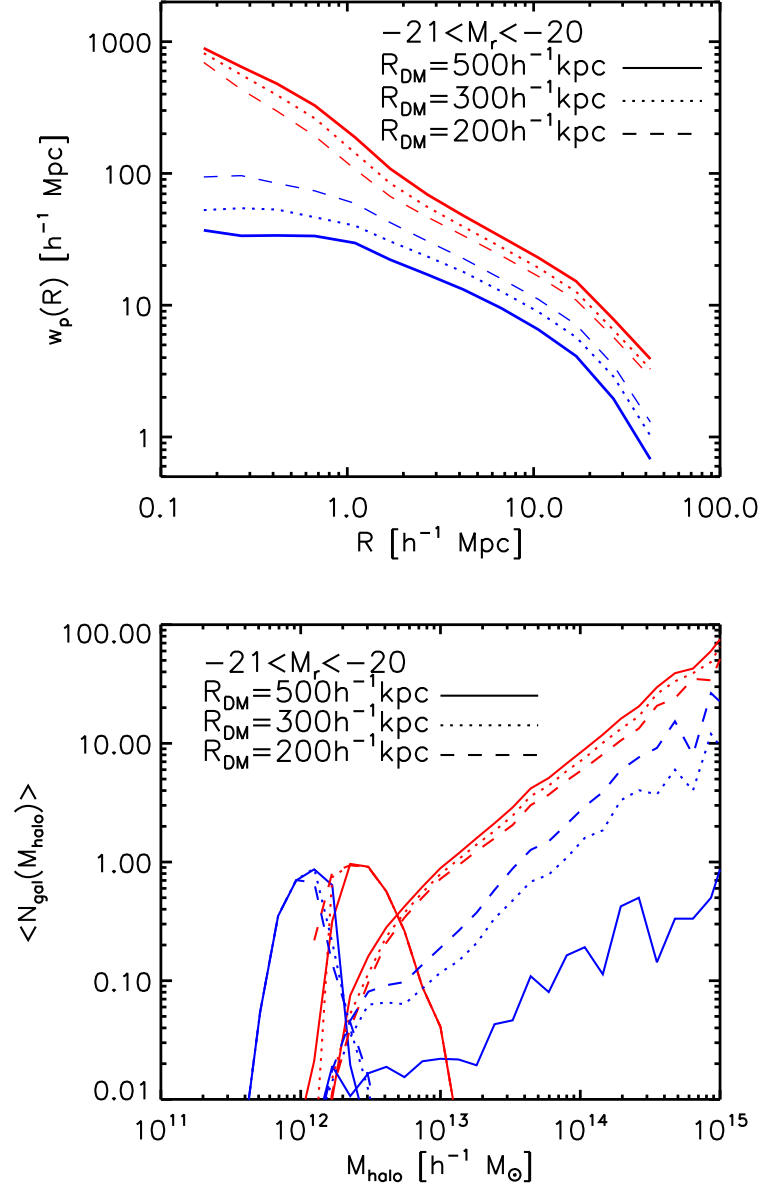


Figure 4.3: Same as Figure 4.2 but for the local density model. The red and the blue lines show w_p or HOD for the subhalo subsamples with higher and lower local density. The adopted sizes of R_{DM} are 500, 300 and $200 h^{-1} \text{ kpc}$.

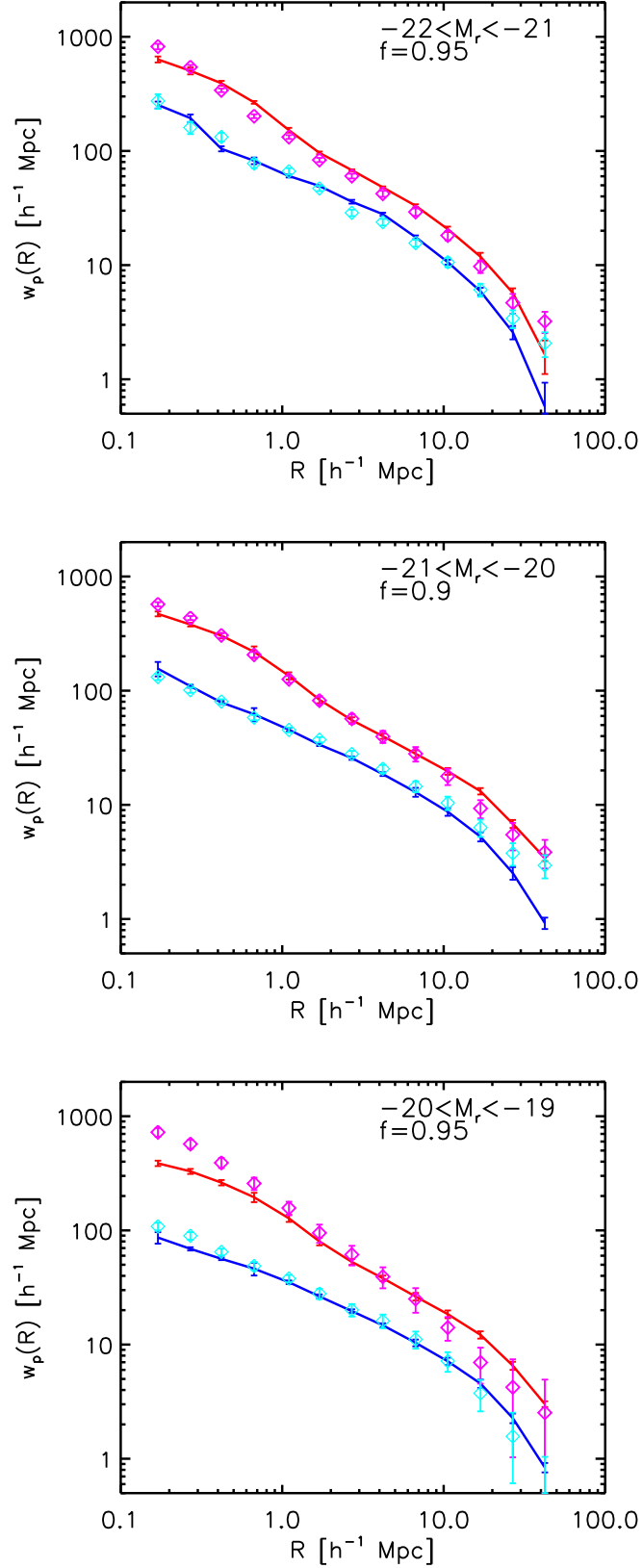


Figure 4.4: Comparison of the projected correlation functions between the best models in the age model (solid lines) and the observation (data points, Zehavi et al. 2011) for the three magnitude binned samples.

	bright	intermediate	faint
red	1.23	2.44	2.09
blue	0.30	0.78	0.43

Table 4.1: The average values of z_{form} as a function of magnitude and color in the age model.

average (Boylan-Kolchin et al. 2010). In Table 4.1, we list the average value of z_{form} in the best model for each magnitude bin and color.

Next we present the results from the local density model. We take seven sphere sizes of $R_{\text{DM}} = 100, 150, 200, 250, 300, 400$ and $500 h^{-1}\text{kpc}$. We compare the best model shown by the thick lines with the observation in Figure 4.5. For the fainter and intermediate samples, we find that the model with $R_{\text{DM}} = 200 h^{-1}\text{kpc}$ is the best model. Only for the brightest sample, the best fit is given by the model with $R_{\text{DM}} = 250 h^{-1}\text{kpc}$.

As well as the age model, our local density model shows good agreement with the observational results. It should be noted that the local density model is motivated by the observed lensing profiles. However the local density model gives a lower clustering amplitude at the smallest scale, $R \lesssim 20 h^{-1}\text{kpc}$, for blue galaxies. It is because that the local density model populates less massive subhalos with more blue central galaxies than the age model does. We will discuss this point in more details below.

HODs from our models

The HODs for each magnitude bin obtained from the best models in our two models are shown in Figure 4.6. The results from the age model and the local density model are shown by the solid and dashed lines. The thick red and thin blue lines represent the red and blue galaxy HODs, respectively. Note that the quoted distinct halo mass in the horizontal axis is the FoF mass. It can be seen that the shapes and amplitudes of HODs of satellite galaxies are very similar among our two models for red and blue galaxies. The primary difference is found in HODs of central galaxies. By construction, the host halo mass range of central is same in the two models. In the local density model, however, central blue galaxies are hosted by low mass distinct halos which have few satellite ones.

We here compare our two models. The most apparent difference between them is the clustering amplitude of blue galaxies at the smallest scale. Systematic suppression of clustering amplitude can be found in the local density model. At such scale, clustering is dominated by signals from central-satellite pairs. As shown in Figure 4.6, the local density model assigns the central blue galaxies to lower mass halos than the age model does whereas satellite galaxies live in more massive halos. It means that the number of distinct halos with a central blue galaxy and more than one blue satellites is decreased. This suppresses the clustering amplitude at

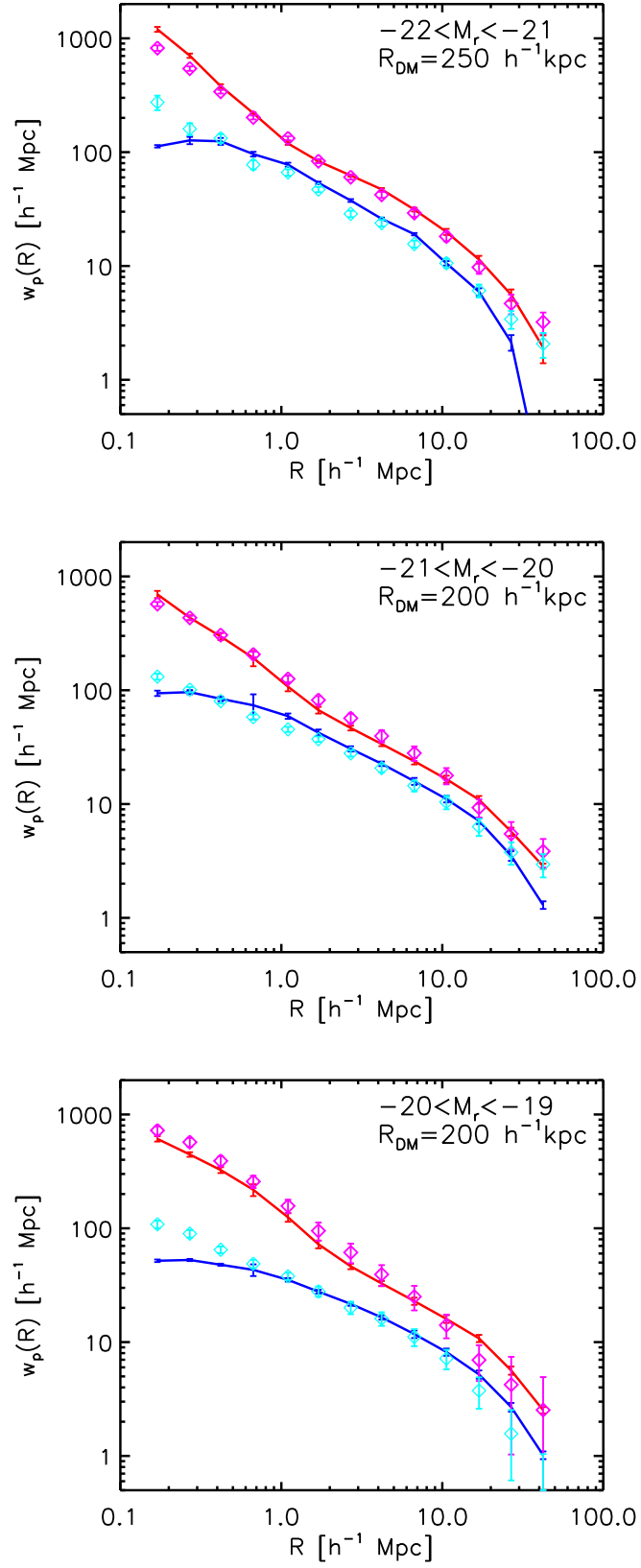


Figure 4.5: Same as Figure 4.4 but for the local density model.

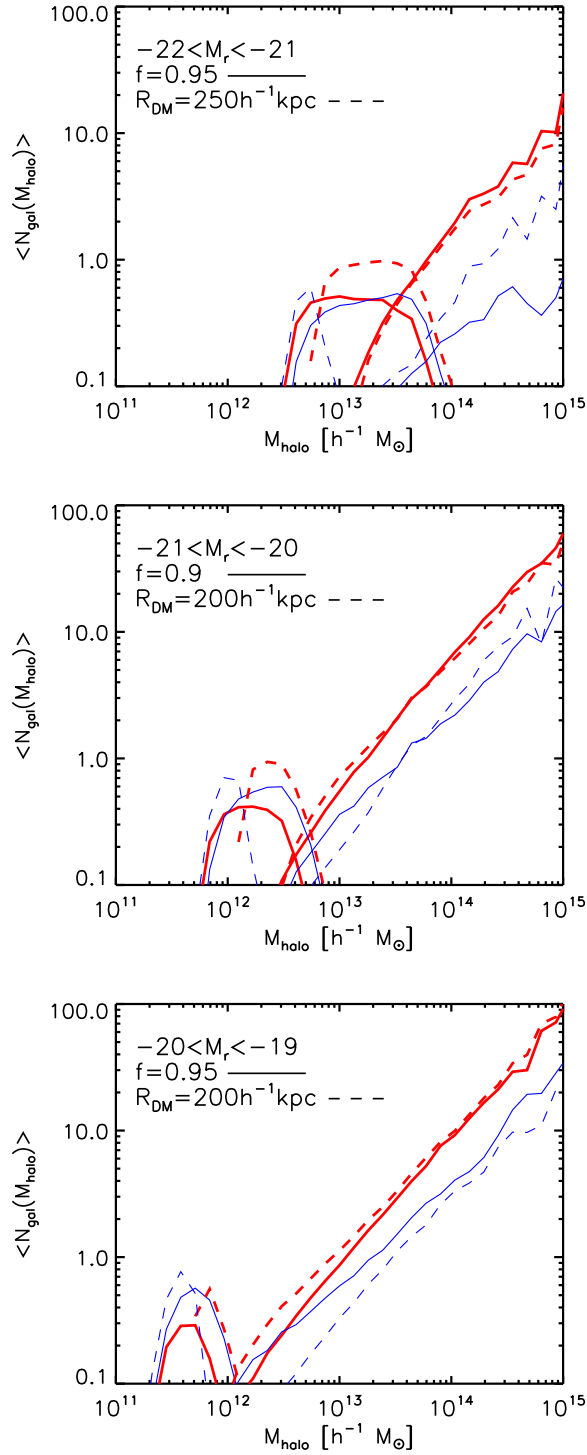


Figure 4.6: The obtained HOD from our two models for red and blue galaxies in the three magnitude bins. The quoted distinct halo mass is the FoF mass. The results from the age model and the local density model are shown by the solid and dashed lines, respectively. The thick red and thin blue lines represent the red and blue galaxy HODs.

	bright	intermediate	faint
age model			
red	0.31	0.41	0.46
blue	0.08	0.21	0.23
local density model			
red	0.26	0.42	0.59
blue	0.16	0.20	0.13

Table 4.2: The obtained satellite fractions from our two model for each magnitude bin.

the small scale.

The satellite galaxy fractions for each bin from our models are listed in Table 4.2. It can be seen that the satellite fractions of red galaxies are higher than those of blue ones in all magnitude bins.

Zehavi et al. (2011) calculated correlation functions analytically with the model HODs. Their assumed HODs of red and blue galaxies have the same form but different amplitudes. They also obtained very good agreement for both red and blue samples. However our two models do not agree exactly with their HOD forms though both reproduce the observed correlation functions well.

4.4.2 Color dependence of lensing profile

We have shown that both the age and the local density models can be tuned to reproduce the observed color dependence of projected correlation functions reasonably well. To discuss which model is better to assign galaxy color, we here consider the galaxy-galaxy lensing measurement $\Delta\Sigma$ as

$$\Delta\Sigma(R) = \gamma_t(R)\Sigma_{\text{cr}} = \bar{\Sigma}(< R) - \Sigma(R), \quad (4.5)$$

where Σ is the surface mass density, γ_t is the tangential shear and Σ_{cr} is the critical surface density (see chapter 1). We project all simulation particles around each subhalo along a direction in the simulation box to measure the surface mass density (chapter 2; Mandelbaum et al. 2005; Hayashi & White 2008; Neistein & Khochfar 2012). Using the red/blue magnitude-binned subhalo catalogs obtained from our models, we calculate the mean profile for each catalog.

We compare the model predictions for red and blue galaxies with measurements for early and late type galaxies by Mandelbaum et al. (2006b). They used flux-limited samples and the average value of `frac_deV` in *g*, *r* and *i* bands to classify the early and late type galaxies (≥ 0.5 for early types and < 0.5 for late types). The parameter `frac_deV` specifies the galaxy flux profile as `frac_deV` × (de Vaucouleurs profile) + (1 − `frac_deV`) × (exponential profile). As a *zeroth order approximation*, we

regard early (late) type galaxies as red (blue) ones. Using the SDSS DR7 (Abazajian et al. 2009), we checked that 74% of early (89% of late) type galaxies actually lie in the red (blue) sequence for $-21 < M_r < -20$. For the fainter (brighter) sample, these rates are 78 (74) % and 85 (91) % for early-red and late-blue correspondences. Therefore the early (late) type samples primarily consist of red (blue) galaxies. Again, the red/blue galaxies are separated via equation (4.4). Sheldon et al. (2004) showed that early (late) types and red (blue) galaxies have very similar lensing profiles but with the different color division and early/late type definition.

In Figure 4.7, we show the results from our age model by thick lines with error bars for the three luminosity binned samples. The red and blue lines are results for red and blue galaxies, respectively. The error bars are taken from twenty seven subsamples of subhalos. The magenta and the cyan data points with error bars are the lensing profiles of early and late type galaxies measured by Mandelbaum et al. (2006b). For the sample of $-22 < M_r < -21$, we simply show the number weighted averages of the observed lensing profiles of $-22 < M_r < -21.5$ and $-21.5 < M_r < -21$ samples. The used subhalo catalogs are from models with $f = 0.9$ for the intermediate and $f = 0.95$ for the fainter and the brighter samples. It can be seen that the age model predictions for the red galaxies agree with the observational results of the early type galaxies well in the three magnitude bins. However the age model does not trace the observation of the late type galaxies of the intermediate and the brightest samples at $100 h^{-1}\text{kpc} \lesssim R \lesssim 1 h^{-1}\text{Mpc}$ at all.

The results from our local density model are shown in Figure 4.8 in the same way as Figure 4.7. For the intermediate and the faintest bins, the adopted size for local DM density measuring is $R_{\text{DM}} = 200 h^{-1}\text{kpc}$. For the brightest bin, $R_{\text{DM}} = 250 h^{-1}\text{kpc}$ is adopted. As well as the age model, agreements between the local density model and the observation are good. The most striking difference from the age model predictions is larger color split at $R \gtrsim 300 h^{-1}\text{kpc}$. This is because the blue galaxies in the local density model live in the less dense region than red ones do. The split is large enough to trace the late type lensing profiles.

We discuss the difference between our two models more quantitatively here. We estimate the effective mass of host distinct halos $\langle M_{\text{eff}} \rangle$ and the average mass of host subhalos $\langle M_{\text{acc}} \rangle$ for each magnitude bin and color. $\langle M_{\text{eff}} \rangle$ is the HOD weighted average mass of host distinct halos M_{halo} and is calculated as

$$\langle M_{\text{eff}} \rangle = \int dM_{\text{halo}} \frac{dn}{dM_{\text{halo}}} M_{\text{halo}} \frac{\langle N_{\text{gal}}(M_{\text{halo}}) \rangle}{n_{\text{gal}}}, \quad (4.6)$$

where dn/dM_{halo} is the distinct halo mass function. The distinct halo mass M_{halo} comes from the FoF algorithm. The subhalo mass is determined by the *SubFind* algorithm at the accretion epoch. We show the masses as a function of magnitude in Figure 4.9 for our two models. The quoted magnitude is the average value for each magnitude bin which can be found in Zehavi et al. (2011). The top and bottom panels show the results from the age and the local density models, respectively. We

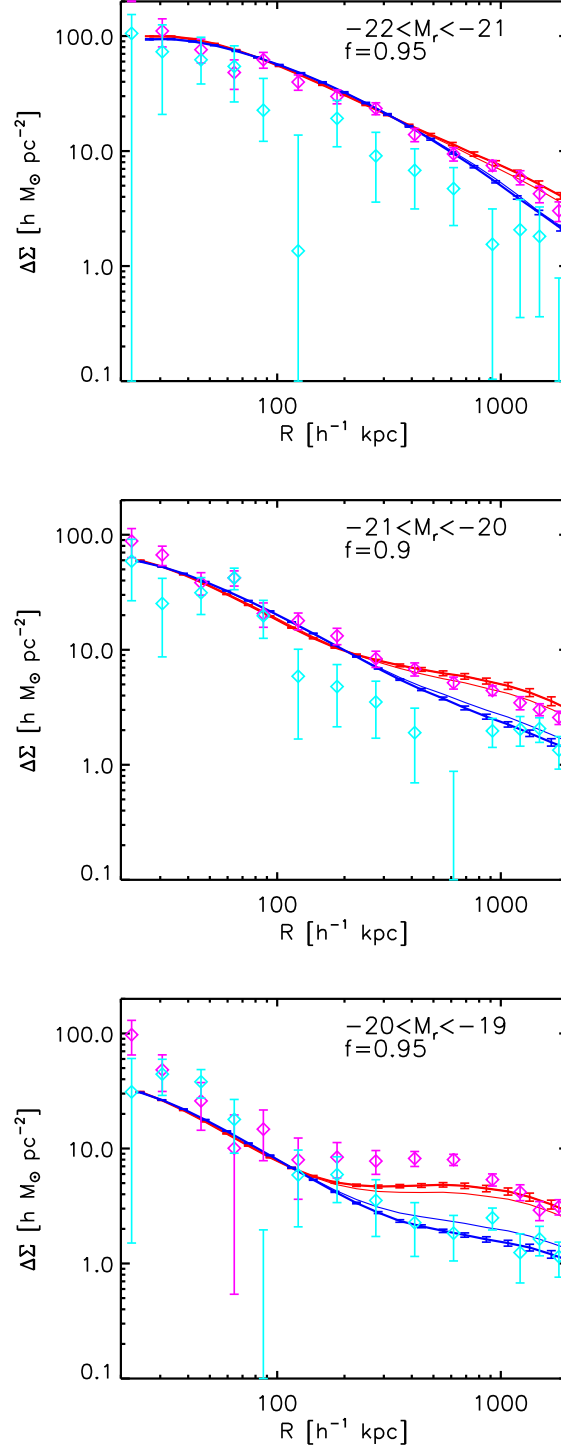


Figure 4.7: Surface mass density profile around galaxies. The red and blue thick lines with error bars represent the predictions for the red and blue galaxies in the age model. The magenta and cyan data points with error bars are the observational results from the SDSS (Mandelbaum et al. 2006b) and show the early and late type galaxies' mass profile, respectively. The thin lines show results for the simulated early/late type samples (see text).

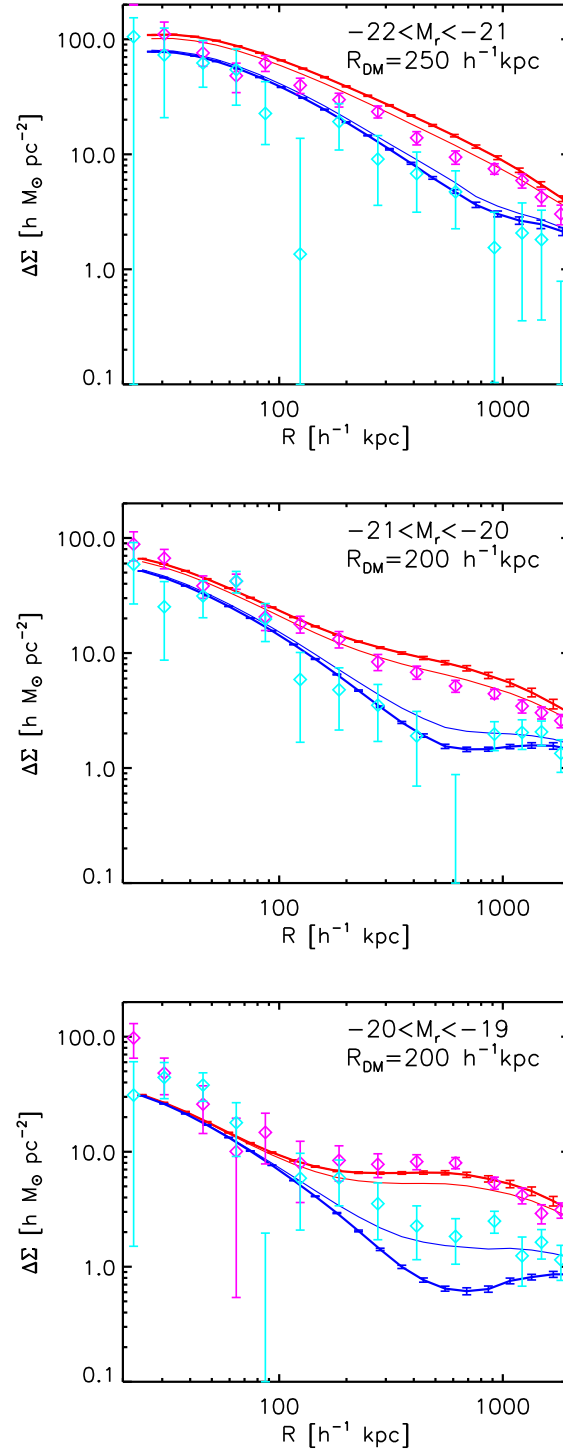


Figure 4.8: Same as Figure 4.7 but for the local density model.

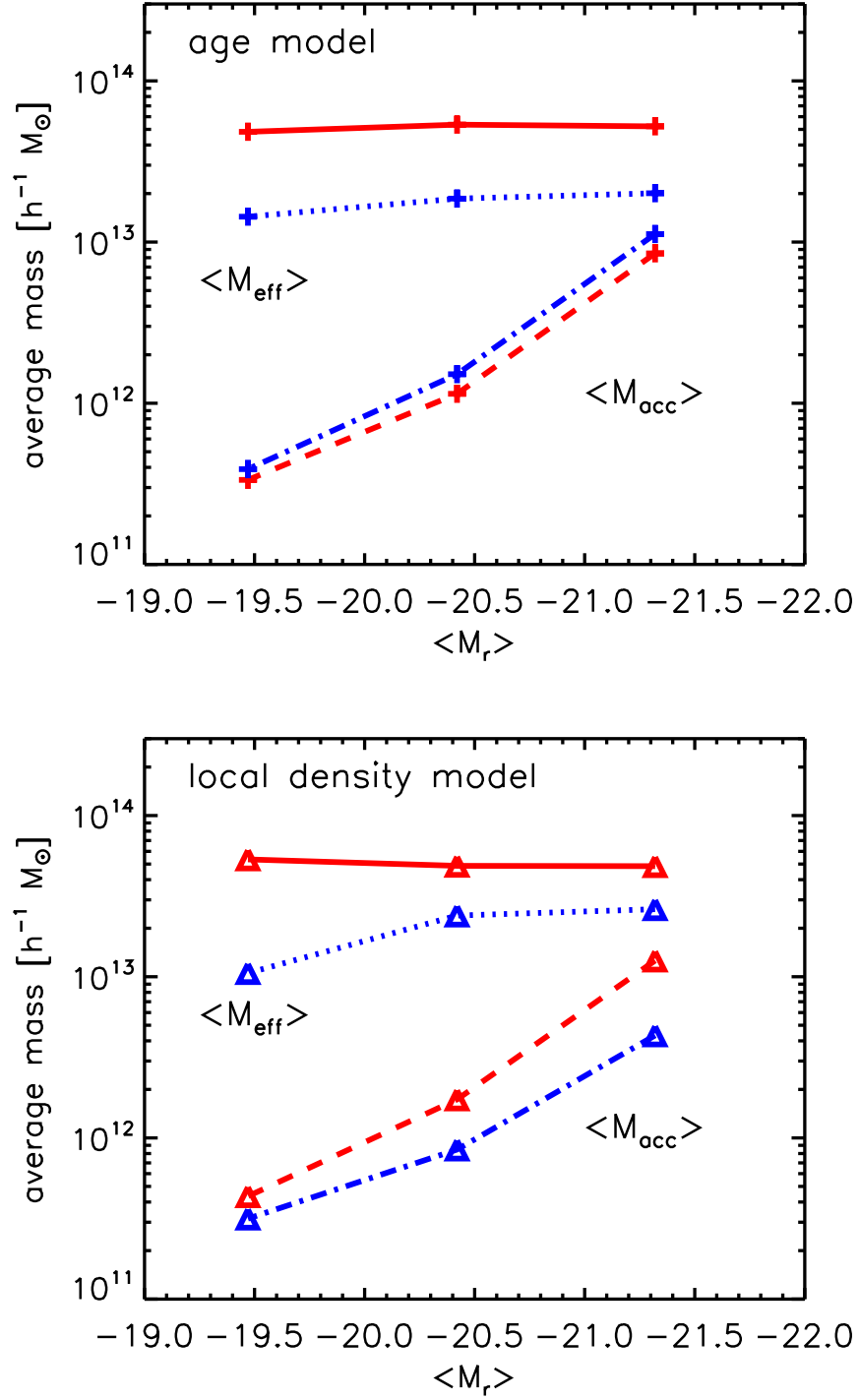


Figure 4.9: The effective mass of distinct host halos $\langle M_{\text{eff}} \rangle$ and the average mass of host subhalos $\langle M_{\text{acc}} \rangle$ as a function of magnitude. $\langle M_{\text{eff}} \rangle$ for red and blue galaxies are shown by solid and dotted lines, respectively. $\langle M_{\text{acc}} \rangle$ for red and blue galaxies are shown by dashed and dotted-dashed lines, respectively. Top: The results for the age model. Bottom: Same as Top panel but for the local density model.

	bright	intermediate	faint
age model			
$\langle M_{\text{eff}} \rangle$ red	5.2×10^{13}	5.4×10^{13}	4.8×10^{13}
$\langle M_{\text{eff}} \rangle$ blue	2.0×10^{13}	1.9×10^{13}	1.4×10^{13}
$\langle M_{\text{acc}} \rangle$ red	8.5×10^{12}	1.1×10^{12}	3.3×10^{11}
$\langle M_{\text{acc}} \rangle$ blue	1.1×10^{13}	1.5×10^{12}	3.9×10^{11}
local density model			
$\langle M_{\text{eff}} \rangle$ red	4.9×10^{13}	4.9×10^{13}	5.4×10^{13}
$\langle M_{\text{eff}} \rangle$ blue	2.6×10^{13}	2.4×10^{13}	1.1×10^{13}
$\langle M_{\text{acc}} \rangle$ red	1.3×10^{13}	1.7×10^{12}	4.4×10^{11}
$\langle M_{\text{acc}} \rangle$ blue	4.3×10^{12}	8.5×10^{11}	3.2×10^{11}

Table 4.3: The effective average mass of host distinct halos $\langle M_{\text{eff}} \rangle$ and the average mass of host subhalos $\langle M_{\text{acc}} \rangle$ from our models for each magnitude bin and color. The unit is $h^{-1}M_{\odot}$.

see that $\langle M_{\text{eff}} \rangle$ of red galaxies is always greater than that of blue galaxies in both the age and the local density models. This is consistent with the fact that the model predicted lensing profiles of red galaxies have higher amplitude than those of blue galaxies at all scales. Also in the local density model, $\langle M_{\text{acc}} \rangle$ of red galaxies is greater than that of blue galaxies. However in the age model, $\langle M_{\text{acc}} \rangle$ of blue galaxies is more massive than that of red galaxies. This trend can be found in HODs of central galaxies from the age model (see Figure 4.6). This is because more massive halos have more rapid mass growth on average (see e.g., Wechsler et al. 2002). Hence, with our definition of the subhalo formation epoch, more massive subhalos tend to be blue galaxies in our age model. Thus the resulting low (high) mass of host subhalos of red (blue) galaxies in the age model makes the color split of the lensing profiles smaller than in the local density model even at $R \lesssim \text{a few} \times 100 h^{-1}\text{kpc}$. The characteristic masses are listed in Table 4.3.

To discuss further, we make a more “fair” comparison with the observation of Mandelbaum et al. (2006b). We match the red/blue fraction of our simulated galaxies in a magnitude bin to the fraction we obtain from the SDSS galaxy catalog for the early/late type sample. To this end, we blend the red/blue galaxies randomly.

The results of lensing measurements from the matched early/late type galaxy catalogs are shown by thin lines in Figures 4.7 and 4.8 without error bars. The red and blue thin lines represent lensing profiles of the early and late types, respectively. We see the effect of the color fraction matching clearly at $R > 300 h^{-1}\text{kpc}$. Figure 4.8 shows fairly good agreement between the predictions from the modified subhalo samples with the local density model and the observations. However the agreement is less impressive for the age model subhalo samples, as can be seen in Figure 4.7. This implies that the local DM density is more crucial for the galaxy color assignment model than the subhalo formation epoch.

4.5 Summary and discussion

We have extended the subhalo abundance matching (SHAM) to develop a new scheme that assigns galaxy color as well as luminosity to subhalos. We consider the subhalo age and the local density as a secondary subhalo property which is expected to be correlated with galaxy color. Technically, we divide a magnitude-binned subhalo catalog obtained by SHAM into two samples by the secondary property. The two samples are then meant to represent red galaxies and blue ones. In a similar fashion to SHAM, the abundance ratio of the red and blue galaxies is matched to the observed ratio. We have studied the spatial clustering of the red and blue galaxies based on the subhalo age model and the local density model. Overall, the two models reproduce the observed color-dependent galaxy clustering properties (Zehavi et al. 2011) reasonably well. It is encouraging that SHAM can be extended successfully in this way by using a secondary subhalo property that can be easily measured.

The clustering amplitudes of the blue galaxies in our local density model is systematically smaller than the observation at $R \lesssim 20 h^{-1}\text{kpc}$, where the central-satellite signal dominates. This is because, in the local density model, central blue galaxies tend to be hosted by relatively small distinct halos (see Figure 4.6). The number of pairs of a blue central and a blue satellite is then smaller than in the observation. The small-scale clustering can be better matched to the observation by introducing scatter in the local DM density-color relation. In the real universe, there are substantial scatters in the relation. It is straightforward to model the scatters by perturbing the measured local DM density with a certain probability distribution, e.g., a Gaussian with a finite variance. Such an 'improved' model would then assign a blue central galaxy more likely to a massive distinct halo. We have explicitly checked that introducing scatters in the local density - color relation, in the above *ad hoc* manner, improves the agreement in the small-scale clustering of the blue galaxies.

We have examined a few other subhalo properties as an alternative proxy for galaxy color, for instance, the density concentration and the spin parameter. We have also tried with slightly different definitions for the concentration, spin, age and local DM density. None of them yields better agreement with the observed correlation functions. We thus conclude that our original age model and the local density model are the best among those we have examined. It is worth discussing further the success of our local density model. One can naively expect that galaxies in higher density environment formed earlier and that they are not forming stars actively any more. Thus the local matter density could be related to the galaxy color. The local DM density around a subhalo within $100 h^{-1}\text{kpc}$ -order sphere closely traces the subhalo mass or, for central galaxies, the mass of the host parent halo. Then the subhalo mass itself could be used as a proxy for the galaxy color rather than the local density. We can test the idea by using the subhalo masses determined by the *SubFind* algorithm at the observation time. In this model, more (less) massive subhalos correspond simply to redder (bluer) galaxies similarly to the

local density model. We have run the same calculations in the previous sections. The subhalo mass model does not reproduce at all the observed color-dependent clustering. Because subhalos in a massive distinct halo typically have small masses, owing to tidal mass stripping, they tend to be assigned a blue galaxy in this model. Indeed, the selected blue galaxies show strong clustering at all length scales. We argue that some environmental effect, in terms of local density, is important for color assignment for the satellite galaxies.

It is crucial to test our model predictions against not only spatial clustering but also other measurement(s). We propose to use the color dependence of lensing profile, motivated by the observed morphology dependence (Mandelbaum et al. 2006b). To this end, we regard the early (late) types as the red (blue) galaxies and calculate the lensing profiles for the two populations. The predictions from our two models agree with the observed red galaxy lensing profile reasonably well. In particular the local density model reproduces the observed lensing profile for the blue (late type) galaxies. However, while the local density model shows a large color (morphology) split at $100 h^{-1}\text{kpc} \lesssim R \lesssim 1 h^{-1}\text{Mpc}$, the age model does not account for the low amplitude of the lensing profiles of the late (blue) galaxies with $-21 < M_r < -20$ and $-22 < M_r < -21$ at $100 h^{-1}\text{kpc} \lesssim R \lesssim 1 h^{-1}\text{Mpc}$ at all.

The fact that the age model does not reproduce the observed color (morphology) dependence of lensing profiles might indicate that galaxy color and subhalo age are not tightly related to each other. There is an observational hint for this notion. Tinker et al. (2011) studied the fraction of central galaxies that are not forming stars actively (“quenched centrals”) as a function of the local galaxy density using a SDSS group catalog. They showed that the fraction of passive galaxies does not agree with the fraction of old halos, in particular for relatively small galaxies with $\log[M_*/(h^{-2}M_\odot)] < 10$. Their findings are qualitatively consistent with our result. There is not a tight relation between the galaxy color and the age of the host (sub)halo, or one may need to devise a rather complex conversion from one to the other. We can think of using the subhalo assembly history of red and blue galaxies directly obtained from N -body simulations. Further studies are clearly needed.

The abundance matching is a powerful technique to populate a cosmological simulation with galaxies. It is encouraging that our simple models reproduce the observed color-dependent clustering well. There are a variety of choices of the secondary subhalo property as a proxy of galaxy color, and thus it is important to test models using other observations independent of spatial clustering, as we have done in this chapter.

Chapter 5

Understanding the Nature of Luminous Red Galaxies (LRGs): Connecting LRGs to Central and Satellite Subhalos

5.1 Introduction

Galaxy redshift surveys are one of the primary tools for studying the large-scale structure in the Universe (Davis & Huchra 1982; de Lapparent et al. 1986; Kirshner et al. 1987; York et al. 2000; Peacock et al. 2001). Over the coming decade, astronomers will have even larger surveys including BOSS¹ (Dawson et al. 2012), WiggleZ² (Blake et al. 2011), VIPERS³, FMOS⁴, HETDEX⁵, BigBOSS⁶ (Schlegel et al. 2009), Subaru Prime Focus Spectrograph (PFS⁷; Ellis et al. 2012), *Euclid*⁸, and *WFIRST*⁹. The upcoming generation of galaxy redshift surveys is aimed at understanding cosmic acceleration as well as measuring the composition of the Universe via measurements of both the geometry and the dynamics of structure formation (Wang et al. 1999; Eisenstein et al. 1999; Tegmark et al. 2004; Cole et al. 2005).

On large scales, galaxies trace the underlying distribution of dark matter, thus, measurements of their correlations are an important probe of cosmology. Because of their relatively high spatial densities and their intrinsic luminosities, the luminous red galaxies (LRGs) are one of the most useful tracers as they can reach a higher

¹<http://cosmology.lbl.gov/BOSS/>

²<http://wigglez.swin.edu.au/site/>

³<http://vipers.inaf.it/>

⁴<http://www.naoj.org/Observing/Instruments/FMOS/>

⁵<http://hetdex.org/>

⁶<http://bigboss.lbl.gov/>

⁷<http://sumire.ipmu.jp/pfs/intro.html>

⁸<http://sci.esa.int/euclid>

⁹<http://wfirst.gsfc.nasa.gov/>

redshift, thereby enabling us to cover a larger survey volume for cosmology (Eisenstein et al. 2001, 2005; Wake et al. 2006). Measurements of the clustering properties of LRGs have been used to measure the baryon acoustic oscillation (BAO) scale (Eisenstein et al. 2005; Percival et al. 2007; Anderson et al. 2012) as well as to constrain cosmological parameters (Tegmark et al. 2004; Cole et al. 2005; Reid et al. 2010; Saito et al. 2011).

Our lack of a detailed understanding of the relationship between galaxies and their host halos are the dominant systematic uncertainty in the analysis of large-scale clustering data. The halo occupation distribution (HOD) approach or the halo model approach has been a useful, albeit empirical, approach to relating galaxies to dark matter (see e.g., Peacock & Smith 2000; Seljak 2000; Scoccimarro et al. 2001, for the pioneer works). In these approaches, the distribution of halos is first modeled for a given cosmological model, e.g. by using N -body simulations, and then galaxies of interest are populated into the dark matter halos. The previous works have shown that, by adjusting the model parameters, the HOD based model well reproduces the auto-correlation functions of LRGs measured from the Sloan Digital Sky Survey¹⁰ (SDSS, Zehavi et al. 2005; Zheng et al. 2007; Wake et al. 2008; Reid & Spergel 2009; White et al. 2011). Based on these studies, it has been shown that LRGs reside in massive halos with a typical mass of a few times $10^{13} h^{-1} M_{\odot}$. However, the HOD method employs several simplified assumptions. For instance, the distribution of galaxies is assumed to follow that of dark matter in their host halo and the model assumes a simple functional form for the HOD.

In this chapter, we pursue an alternative approach, abundance matching. The abundance matching method directly connects target galaxies to simulated subhalos assuming a tight and physically-motivated relation between their properties, e.g., galaxy luminosity and subhalo circular velocity, without employing any fitting parameters (e.g., chapter 4; Kravtsov et al. 2004; Conroy et al. 2006; Trujillo-Gomez et al. 2011; Reddick et al. 2012; Nuza et al. 2012). However, it is not still clear whether the method can simultaneously reproduce different clustering measurements such as the auto-correlation function and the galaxy-galaxy weak lensing (Neistein & Khochfar 2012). Most authors only use the auto-correlation function to test their abundance matching model.

However, rather than matching galaxies with halos at low redshift, we take an alternative approach to abundance matching. Motivated by observations suggesting that LRGs are passive, massive early-type galaxies, which are believed to have formed at $z > 1$ (Masjedi et al. 2008; Carson & Nichol 2010; Tojeiro et al. 2012), we assume that the progenitor halos for LRG-host subhalos are formed at $z = 2$. (The conclusions of the method are not sensitive to the exact redshift choice). We identify the most massive halos at this redshift, follow the innermost particles of each progenitor halo, and then identify the subhalos at $z = 0.3$ containing these particles. We adjust the number of halos identified as LRG progenitors at $z = 2$

¹⁰<http://www.sdss.org/>

to match the observed number density of the SDSS LRGs, $\bar{n}_{\text{LRG}} \simeq 10^{-4} h^3 \text{ Mpc}^{-3}$ (also see Conroy et al. 2008; Seo et al. 2008, for a similar idea based method). In this method, we directly trace, from the simulations, how each progenitor halo at $z = 2$ experiences merger(s), is destroyed or survives at lower redshift as well as which progenitor halos become central or satellite galaxies in each host halo at $z = 0.3$. Thus, our method allows us to include assembly/merging histories of the LRG-progenitor halos. Our method is solely based on a mass-selected sample of progenitor halos at $z = 2$ and does not have *any* free parameter because the mass threshold is fixed by matching to the number density of SDSS LRGs. We compare statistical quantities computed from our mock catalog with the SDSS measurements: the HOD, the projected auto-correlation function of LRGs, the LRG-galaxy weak lensing. Even though our method is rather simple, we show that our mock catalog remarkably well reproduces the different measurements simultaneously. Then we discuss the non-linear redshift distortion effect, the Finger-of-God (FoG) effect, and implications for cosmological interpretation of the redshift-space power spectrum of LRGs.

5.2 Methods

5.2.1 Cosmological N -body simulations

We perform two realizations of cosmological N -body simulations using the publicly-available *Gadget-2* code (Springel et al. 2001b; Springel 2005). For each run, we assume a flat Λ CDM cosmology with $\Omega_{\text{m}} = 0.272$, $\Omega_{\text{b}} = 0.0441$, $\Omega_{\Lambda} = 0.728$, $H_0 = 100h = 70.2 \text{ km s}^{-1} \text{ Mpc}^{-1}$, $\sigma_8 = 0.807$ and $n_s = 0.961$ using the same parameters and notation as in the the *WMAP* 7-yr analysis (Komatsu et al. 2011). Our large scale simulation, which we label at L1000, employs 1024^3 dark matter particles in a box of $1 h^{-1} \text{ Gpc}$ on a side. This large box is most useful for statistical quantities such as correlation functions, so we will mainly use the L1000 simulation to have enough statistics. We test convergence with a higher resolution simulation that employs 1024^3 particles in a box of $300 h^{-1} \text{ Mpc}$ on a side. This run is referred as L300. The mass resolution for the simulations (mass of an N -body particle) is $7 \times 10^{10} h^{-1} M_{\odot}$ or $1.9 \times 10^9 h^{-1} M_{\odot}$ for L1000 or L300, respectively. The initial conditions for both simulations are generated using the second-order Lagrangian perturbation theory (Crocce et al. 2006; Nishimichi et al. 2009) and an initial matter power spectrum at $z = 65$, computed from the *CAMB* code (Lewis et al. 2000). We set the gravitational softening parameter to be 30 and $8 h^{-1} \text{ kpc}$ for L1000 and L300 runs, respectively.

We use the friends-of-friends (FoF) group finder (e.g., Davis et al. 1985) with a linking length of $b = 0.2$ in units of the mean interparticle spacing to create a catalog of halos from the simulation output and use the *SubFind* algorithm (Springel et al. 2001a) to identify subhalos within each halo. We use halos and subhalos that contain more than 20 particles. Each particle in a halo region is assigned to

either a smooth component of the parent halo or to a subhalo, where the smooth component contains the majority of N -body particles in the halo region. Hereafter we refer the smooth component as the central subhalo and the subhalo(s) as satellite subhalo(s), respectively. For each subhalo, we estimate its mass by counting the bounded particles, which we refer as the subhalo mass (M_{sub}). We store the data (positions and velocities) of particles in halos and subhalos at different redshifts. To estimate the virial mass (M_{vir}) for each parent halo, we apply the spherical overdensity method to the FoF halo, where the boundary of the spherical region is determined by the interior virial overdensity, Δ_{vir} , relative to the mean mass density (Bryan & Norman 1998). The overdensity is $\Delta_{\text{vir}} \simeq 268$ at $z = 0.3$ for the assumed cosmological model. The virial radius is estimated from the estimated mass as $R_{\text{vir}} = (3M_{\text{vir}}/4\pi\bar{\rho}_{m0}\Delta_{\text{vir}})^{1/3}$, where $\bar{\rho}_{m0}$ is the comoving matter density.

5.2.2 Mock catalogs of LRGs: connecting halos at $z = 2$ to central and satellite subhalos at $z = 0.3$

LRGs are passively-evolving, early-type massive galaxies, and their typical stellar ages are estimated as ~ 5 Gyrs (Kauffmann 1996; Wake et al. 2006; Masjedi et al. 2008; Carson & Nichol 2010). This implies that LRGs, at least a majority of their stellar components, were formed at $z \gtrsim 1$ (Masjedi et al. 2008). Motivated by this fact, we here propose a simple abundance matching method for connecting LRGs to dark matter distribution in large-scale structure as follows.

Our method rest on an assumption that progenitor halos for LRG-host subhalos today are formed at $z = 2$, which is close to the peak redshift of cosmic star formation rate (Hopkins & Beacom 2006). Our choice of $z = 2$ is just a first attempt, and a formation redshift can be further explored so as to have a better agreement with the SDSS measurements (see Section 5.5 for further discussion). First, we select halos from the simulation output at $z = 2$ as candidates of the progenitor halos (hereafter sometimes referred as $z2$ -halo in this chapter). In doing this, we select the $z2$ -halos in descending order of their masses (from more massive to less massive) until the comoving number density becomes close to that of SDSS LRGs at $z = 0.3$, which we set to $\bar{n}_{\text{LRG}} = 10^{-4} h^3 \text{Mpc}^{-3}$. More exactly speaking, we need to identify more halos at $z = 2$ having the number density of $\simeq 1.3 \times 10^{-4} h^3 \text{Mpc}^{-3}$ at least, because about 30 % of $z2$ -halos, preferentially in a massive halo region at $z = 0.3$, experience mergers from $z = 2$ to $z = 0.3$ for the assumed ΛCDM model (see below for details). Second, we trace the 30 % innermost particles of each $z2$ -halo particles to lower-redshift simulation outputs until $z = 0.3$, where the innermost particles are defined by particles within a spherical boundary around the mass peak of a $z2$ -halo (see Figure 5.1). Third, we match the traced innermost particles of each $z2$ -halo to central and satellite subhalos at $z = 0.3$ (hereafter $z0.3$ -subhalo). If more than 50 % of the innermost particles are contained in a $z0.3$ -subhalo, we define the subhalo as the subhalo hosting LRG at $z = 0.3$. We repeat this procedure in

descending order of the FoF masses of $z2$ -halos until the comoving number density of the matched $z0.3$ -subhalos (LRG-host subhalos) is closest to the target value of $\bar{n}_{\text{LRG}} = 10^{-4} h^3 \text{Mpc}^{-3}$. Thus we should stress that our method does not have *any* free parameter to adjust; the mass threshold for the LRG-progenitor halos is fixed by the target number density. In addition, central and satellite subhalos are populated with galaxies under a single criterion: if a subhalo at $z = 0.3$ is a descendant of the $z2$ -halo, the subhalo is included in the matched sample. On the other hand, the standard abundance matching uses different quantities for central and satellite subhalos, e.g., the circular velocities at the redshift of target galaxies or at the accretion epoch, an epoch for a subhalo accreting onto the parent halo. In this way, we construct a mock catalog of LRGs at $z = 0.3$, and keep all the necessary information; the mass of LRG-progenitor $z2$ -halo, the mass of LRG halo at $z = 0.3$, the mass and location of each LRG-host subhalo and the internal motion inside the parent halo. We refer an LRG, which resides in a central or satellite subhalo, as a central or satellite LRG, respectively, in each parent halo.

Some of the LRG-host halos at $z = 0.3$, especially massive halos, contain multiple LRG-host subhalos in our mock catalog (see the example in the lower panel of Figure 5.1). We often call such systems “multiple-LRG systems” in the following discussion (also see Reid & Spergel 2009; Hikage et al. 2012a). We refer the LRG-host halos, which host only a single LRG inside, as “single-LRG systems”. The average halo masses for the single- and multiple-LRG systems are found from the L1000 run to be $M_{\text{vir}} = 4.8 \times 10^{13}$ and $1.5 \times 10^{14} h^{-1} M_{\odot}$, respectively. The fraction of the multiple-LRG systems among all the LRG-host halos is about 8 % in the L1000 run. Assuming that most stars in each LRG are formed until $z = 2$ and the total stellar mass scales with host halo mass, i.e. mass of $z2$ -halo, we will often refer the most massive $z2$ -halo in a multiple-LRG system as the brightest LRG (BLRG), while we refer the smallest $z2$ -halo as the faintest LRG (FLRG). Note that we also refer an LRG in a single-LRG system as BLRG. A BLRG does not necessarily become a central galaxy in the parent halo at $z = 0.3$, although the central subhalo is the most massive subhalo in the parent halo by definition.

Table 5.1 summarizes properties of the LRG-host halos in our mock catalog, computed using the L1000 run. In the table, we give the average virial mass and radius for all the LRG-host halos and for each sample of the single- and multiple-LRG halos. The table also gives the fraction of satellite LRGs or central LRGs in each sample of the host halos. These results can be compared with the recent results found in Hikage et al. (2012a) from the SDSS DR7 LRG catalog, as given in the table caption. The mock catalog fairly well reproduces the SDSS results. In the following, we study these quantities in more detail.

Figure 5.1 shows snapshots of the N -body particle distribution in the L1000 run outputs at different redshifts, for the regions where multiple- or single-LRG systems are formed at $z = 0.3$. The figure clearly shows how each LRG-progenitor halo is defined at $z = 2$, how the innermost particles are traced to lower redshift and

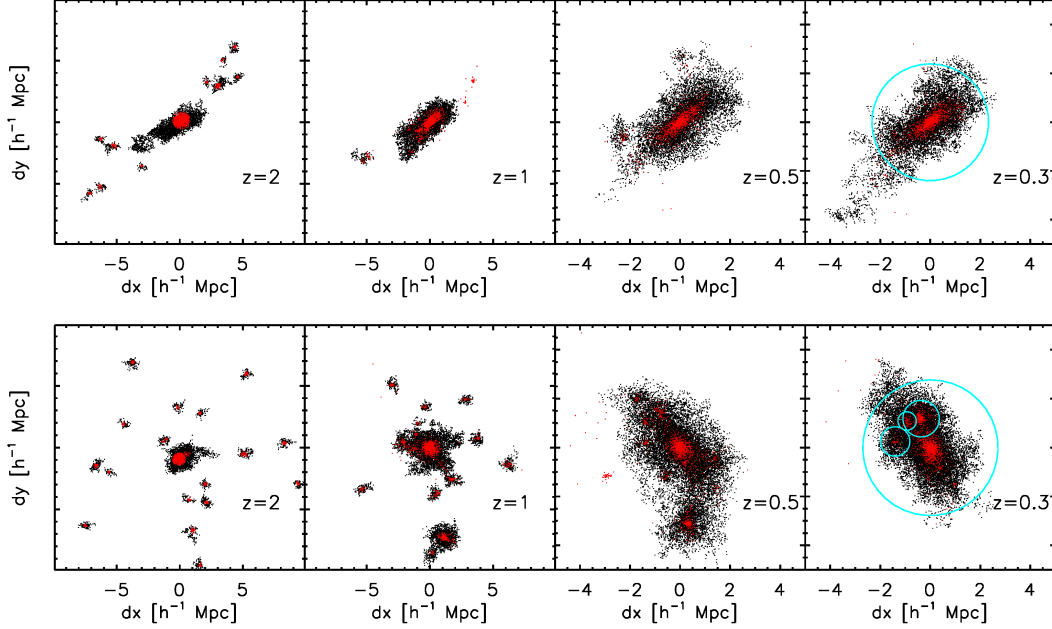


Figure 5.1: Evolution of dark matter (N -body) particle distribution around the region of subhalos hosting mock LRGs at $z = 0.3$, taken from our L1000 simulation run. The upper-row panels are for the region around a halo which hosts only one central LRG (the host halo mass $M_{\text{vir}} = 8.42 \times 10^{14} h^{-1} M_{\odot}$), while the lower-row panels are the most massive host-halo among systems hosting one central and three satellite LRGs ($M_{\text{vir}} = 1.44 \times 10^{15} h^{-1} M_{\odot}$). The dot symbols in each panel are member particles in the halo regions at $z = 2$ or the subhalo region(s) at lower redshifts. The red-color particles are 30% innermost particles of each halo at $z = 2$. The upper-row panels show the case that 11 progenitor halos of LRGs are formed at $z = 2$, and then are merged at lower redshift, forming one central LRG in the host halo at $z = 0.3$. The lower-row panels show that 24 progenitor halos at $z = 2$ form one central LRG and three satellite LRGs in the host-halo at $z = 0.3$. The blue circles in the panel of $z = 0.3$ shows the positions of mock LRGs. The size of each circle is proportional to $M_{\text{sub}}^{1/3}$, where M_{sub} is the subhalo mass.

Type of LRG-host halos	Total number	$\bar{M}_{\text{vir}} [h^{-1}M_{\odot}]$	$\bar{R}_{\text{vir}} [h^{-1}\text{Mpc}]$
All LRG-host halos	91,090	5.64×10^{13}	0.80
Single-LRG halos	83,891	4.81×10^{13}	0.78
Multiple-LRG halos	7,199	1.52×10^{14}	1.1

Type of LRG-host halos	$f_{\text{sat-LRG}}$	$q_{\text{cen}}^{\text{BLRG}}$	$q_{\text{cen}}^{\text{FLRG}}$
All LRG-host halos	0.099	0.96	–
Single-LRG halos	0.022	0.98	–
Multiple-LRG halos	1.00	0.74	0.21

Table 5.1: Summary of properties of LRG-host halos, computed from the mock LRG catalog in the L1000 simulation run (see text for details). \bar{M}_{vir} and \bar{R}_{vir} are the average virial mass and radius of the host halos. $f_{\text{sat-LRG}}$ is the fraction of halos that have satellite LRG(s) among all LRG-host halos taken in each row. $q_{\text{cen}}^{\text{BLRG}}$ is the fraction of halos that host its BLRG as a central galaxy among all the halos. $q_{\text{cen}}^{\text{FLRG}}$ is the fraction of halos that host FLRG as a central LRG. Note that the fraction of satellite LRGs among all the LRGs (not the LRG-host halos) in the mock catalog is 0.108. The results can be compared with the results in Hikage et al. (2012a) obtained from the SDSS DR7 LRG catalog and the halo model analysis: the fraction of multiple-LRG systems among all the LRG-host halos is 0.045, the average halo masses for the single- and multiple-LRG systems are $\bar{M}_{\text{vir}} \simeq 0.36$ and $1.36 \times 10^{14} h^{-1}M_{\odot}$, respectively, and the fractions of central BLRGs and FLRGs in the multiple-LRG systems $q_{\text{cen}}^{\text{BLRG}} \simeq 0.54$ and $q_{\text{cen}}^{\text{FLRG}} \simeq 0.32$, respectively.

how LRG-progenitor halos merge with each other and become to reside in central and satellite subhalos at the final redshift $z = 0.3$. Our method directly traces the merging and assembly histories of LRG-progenitor halos. Although the number density of LRG-host subhalos is set to the density of LRGs as we described above, the figure shows that more LRG-progenitor halos or subhalos survive (with less mergers) at higher redshift than at $z = 0.3$. Hence our method also has a capability to study what kinds of halos or subhalos at higher redshift are progenitors for the SDSS LRGs (see Section 5.5 for a further discussion).

Figure 5.2 shows how each LRG-progenitor halo at $z = 2$ loses or gains its mass due to merger and/or tidal stripping when it becomes an LRG-host subhalo at $z = 0.3$, computed using the catalogs of halos and subhalos in the $z = 2$ and $z = 0.3$ outputs of L1000 run. Note that the halo mass shown in the x -axis, M_{FoF} , is the FoF mass, the sum of FoF particles in each halo region. First, the figure shows that we need to select the LRG-progenitor halos at $z = 2$ down to a mass scale of about $6 \times 10^{12} h^{-1}M_{\odot}$ which contains about 90 N -body particles for the L1000 run. It is shown that some subhalos for satellite LRGs lose their masses due to tidal stripping as implied in Figure 5.1, while subhalos for central LRGs gain their masses due to merger. Comparing the top and bottom panels manifests that multiple-LRG systems tend to reside in more massive LRG-progenitor halos at $z = 2$ and become more massive LRG-host halos at $z = 0.3$, and that the mass difference between subhalos for central and satellite LRGs is larger in multiple-LRG systems, implying

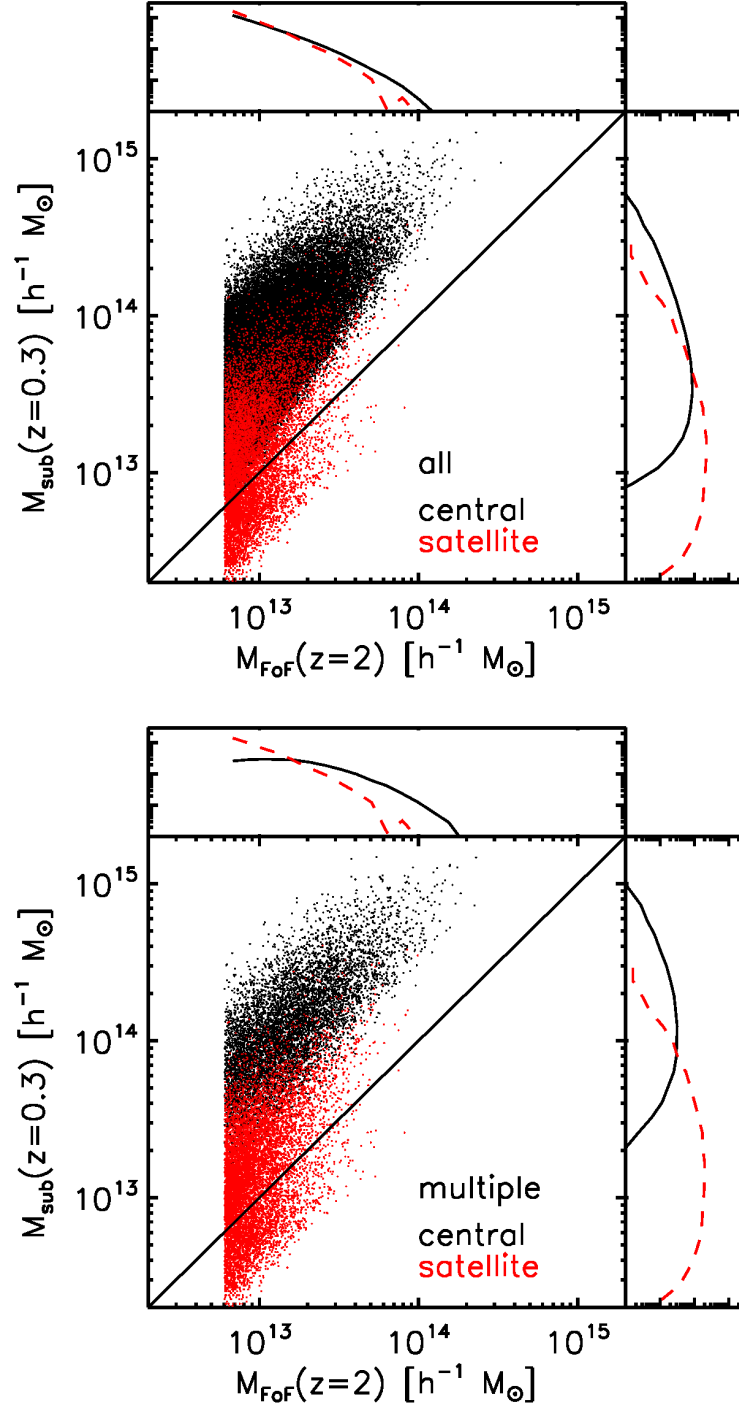


Figure 5.2: Comparisons between masses of the LRG-progenitor halos at $z = 2$ and the LRG-host subhalos at $z = 0.3$, computed from the L1000 run. The top and bottom panels show the results for all the LRG-host halos and the multiple-LRG systems, respectively. The black and red points are for central and satellite LRGs, respectively. The line in each panel shows the case that the progenitor halo does not either gain or lose its mass at $z = 0.3$, i.e., $M_{\text{sub}}(z = 0.3) = M_{\text{FoF}}(z = 2)$. The upper- and right-side panels in each plot are the projected distributions for central and satellite LRGs along the y - or x -axis direction, respectively.

a larger difference between their luminosities (see Hikage et al. 2012a, for a similar discussion).

Thus our method is solely based on the masses of LRG-progenitor halos at $z = 2$ (see Figure 5.2) and the connection with central and satellite subhalos in the parent halos at $z = 0.3$. On the other hand, LRGs in the SDSS catalog are selected based on the magnitude and color cuts from the SDSS imaging data (primarily *gri*), and are not necessarily a stellar-mass-selected sample, although their stellar masses are believed to have a tight relation with the host halo masses. Nevertheless, we will show below that the mock catalog surprisingly well reproduces the SDSS measurements.

Since LRGs in our mock catalog reside in relatively massive halos at $z = 2$, with masses $M_{\text{FoF}} \gtrsim 6 \times 10^{12} h^{-1} M_{\odot}$ (Figure 5.2), as well as in massive parent halos at $z = 0.3$, our method does not necessarily require a high spatial resolution for simulations. A simulation with $1 h^{-1} \text{Gpc}$ on a side length seems sufficient, which allows an accurate estimation of statistical quantities of LRGs. This is not the case if one wants to work on the abundance matching method for less massive galaxies or more general types of galaxies (e.g., chapter 4; Trujillo-Gomez et al. 2011; Reddick et al. 2012).

5.3 Results: comparisons with the SDSS LRG measurements

5.3.1 Halo occupation distribution

To test our abundance matching method to create LRG mock catalogs, we compare the predictions with the SDSS measurements. First, we study the halo occupation distribution (HOD) for LRGs in Figure 5.3, where the HOD gives the average number of LRGs that the halos at $z = 0.3$ host as a function of host-halo mass. Here we consider the HODs for central and satellite LRGs which reside in central and satellite subhalos in the LRG-host halos, respectively. Again we should emphasize that our method does not assume any functional forms for the HODs, unlike done in the standard HOD method, and rather allows us to directly compute the HODs from the simulations. The figure shows that, even if LRG-progenitor halos are selected from halos at $z = 2$ by a *sharp* mass threshold, our mock catalog naturally predicts that the central HOD has a smoother shape around a minimum halo mass, as a result of their merging and assembly histories from $z = 2$ to $z = 0.3$. To be more precise, the central HOD is smaller than unity ($\text{HOD} < 1$) for host halos with $M_{\text{vir}} \lesssim 10^{14} h^{-1} M_{\odot}$, meaning that only some fraction of the halos host a central LRG. Most of massive halos host at least one LRG and can host multiple LRGs inside. Conversely, the L1000 run shows that the fraction of massive halos, which do not host *any* LRG, is 1.3 % for halos with masses $M_{\text{vir}} \geq 1 \times 10^{14} h^{-1} M_{\odot}$, while *all* halos with $M_{\text{vir}} \geq 2 \times 10^{14} h^{-1} M_{\odot}$ have at least one LRG inside.

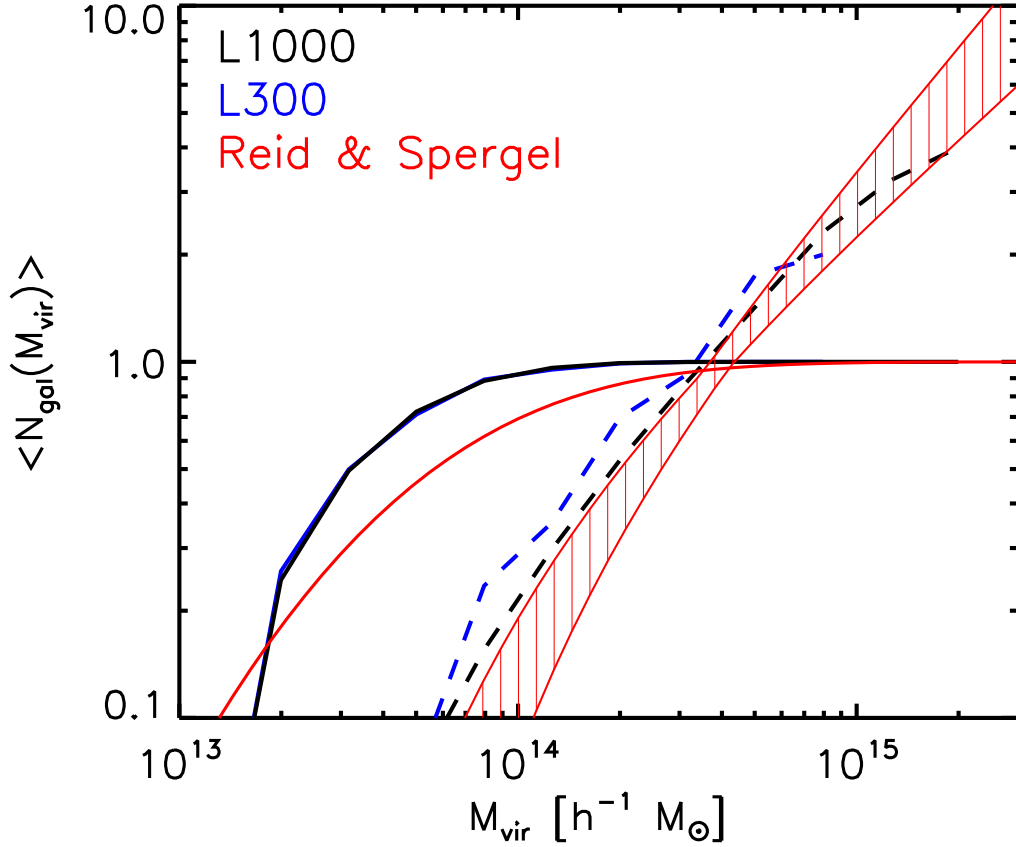


Figure 5.3: The halo occupation distribution (HOD) for LRGs as a function of parent halo mass, measured from our mock catalog. The solid and dashed curves show the HOD of central and satellite LRGs, respectively. The black and blue curves are the results from the L1000 and L300 runs, respectively. The red curves show the SDSS measurements, taken from Reid & Spergel (2009, RS09). RS09 fixed the function form of central HOD, and then constrained the satellite HOD from the SDSS LRG catalog using the Counts-in-Cylinders technique. The hatched region is the range allowed by varying each model parameter of the satellite HOD within its 1σ confidence range.

In Figure 5.3, we compare the HODs of our mock catalog with the result in Reid & Spergel (2009, hereafter RS09), where the HOD was constrained by using the Counts-in-Cylinders (CiC) method for identifying multiple LRG systems from the SDSS DR7 LRG catalog with the aid of halo catalogs in N -body simulations. Although the cosmological models are slightly different in between our study and RS09 and the assumed redshift is slightly different ($z = 0.2$ in their study), we employed the same best-fit parameters to compute the LRG HOD in RS09 for this figure.

Due to limited constraints from the SDSS LRG catalog, especially for low-mass host-halos, RS09 assumed the fixed form for the central HOD:

$$\langle N_{\text{cen}}(M) \rangle = \frac{1}{2} \left[1 + \text{erf} \left(\frac{\log_{10} M - \log_{10} M_{\text{min}}}{\sigma_{\log M}} \right) \right], \quad (5.1)$$

with $M_{\text{min}} = 5.7 \times 10^{13} h^{-1} M_{\odot}$ and $\sigma_{\log M} = 0.7$, in order to obtain meaningful constraints on the satellite HOD. The central HOD for low-mass host-halos is difficult to constrain, because low-mass host-halos of LRGs are observationally difficult to identify. Our mock catalog naturally predicts a smoother shape for halos with $M \lesssim 10^{14} h^{-1} M_{\odot}$ for the central HOD. Therefore, we do not think that the difference for the central HODs is significant, and needs to be further carefully studied.

On the other hand, the satellite HOD in RS09 is almost perfectly recovered by our mock catalog, where RS09 assumed the functional form for the satellite HOD to be given by $\langle N_{\text{sat}}(M) \rangle = \langle N_{\text{cen}}(M) \rangle [(M - M_{\text{cut}})/M_1]^\alpha$ and then constrained the parameters $(M_{\text{cut}}, M_1, \alpha)$ from the SDSS LRG catalog. The hatched region is the range at each host-halo mass that is allowed by varying the model parameters within the 1σ confidence regions. Our results confirm that parent halos of $\sim 10^{15} h^{-1} M_{\odot}$ have up to several LRGs inside, as first pointed out in RS09. The L300 result, the simulation result with higher spatial resolution, gives similar results to the L1000 results, showing that the numerical resolution is not an issue for the HOD results. Even though SDSS LRGs are selected by the magnitude and color cut, not by their host subhalo masses, our method seems to capture the origin of SDSS LRGs; mass-selected halos at $z \sim 2$ are main progenitors of LRGs, and their subsequent assembly and merger histories determine where LRGs are distributed within the host halos at lower redshift.

5.3.2 Projected correlation function

Next we study the projected auto-correlation function of LRGs, $w_p(R)$, defined as

$$w_p(R) = 2 \int_0^{\pi_{\text{max}}} d\pi \xi_{\text{gg}}(r = \sqrt{\pi^2 + R^2}), \quad (5.2)$$

where R is the projected separation between two LRGs in the pairs used for the correlation measurement in units of the comoving scale, π is the separation parallel to

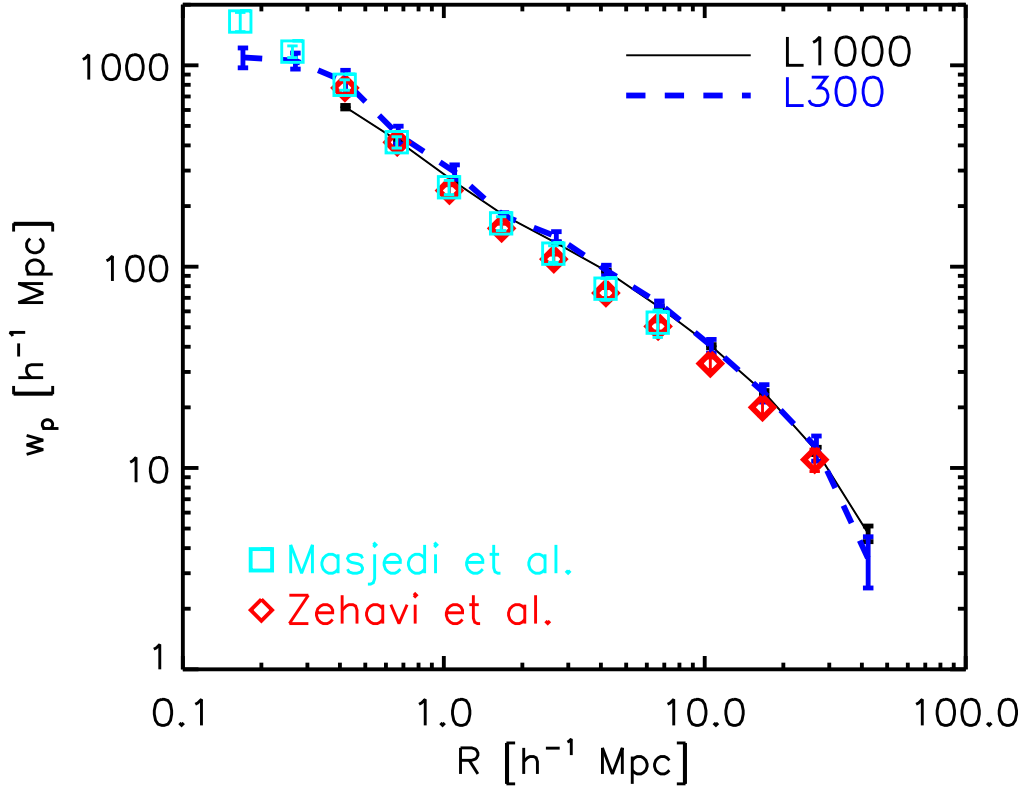


Figure 5.4: Projected auto-correlation function w_p of LRGs as a function of the projected distance R . The solid and dashed curves show the results from our mock catalogs in the L1000 and L300 runs, respectively. The error bars are estimated using the measurements from 8 subdivided volumes of each simulation volume. The square and diamond symbols are the correlation functions measured from the SDSS catalog of LRGs at $z \sim 0.3$, taken from Zehavi et al. (2005) and Masjedi et al. (2006), respectively.

the line-of-sight and $\xi_{gg}(r)$ is the three-dimensional correlation function. Following Zehavi et al. (2005), π_{\max} is set to be $80 \ h^{-1}\text{Mpc}$. The projected correlation function is not affected by the redshift-space distortion effect due to peculiar velocities of LRGs.

In Figure 5.4, we compare the projected correlation function measured from our LRG mock catalog with the SDSS measurements (Zehavi et al. 2005; Masjedi et al. 2006). In the SDSS measurements, Zehavi et al. (2005) used an LRG sample in the magnitude range of $-23.2 < M_g < -21.2$ and with the mean redshift $\langle z \rangle \simeq 0.3$. Masjedi et al. (2006) used the same sample to extend the measurement down to very small scale, below $R = 500 \ h^{-1}\text{kpc}$, by taking into account various observational effects such as the fiber collision. Note that the number density of the SDSS LRGs is $9.7 \times 10^{-5} \ h^3\text{Mpc}^{-3}$, which is slightly smaller than the number density of the mock LRGs ($10^{-4} \ h^3\text{Mpc}^{-3}$), and the cosmological model employed in the measurement

is slightly different from the model we assumed for our simulations. The figure shows that our mock catalog remarkably well reproduces the projected correlation function of LRGs over a wide range of separation radii, including the one-halo and two-halo terms that arise from correlations between LRGs within the same host halo and in different host halos, respectively. Comparing the results for the L1000 and L300 runs reveals that the correlation function for L1000 has a smaller amplitude at $R < 0.7 h^{-1}\text{Mpc}$ than that for L300. Thus the L1000 run implies a systematic error due to the lack of numerical resolution at the small scales. The L300 result shows a better agreement with the SDSS measurement in Masjedi et al. (2006). The small-scale clustering arises mostly from multiple-LRG systems, different LRGs in the same halo, so that numerical resolution seems important to resolve these small subhalos.

5.3.3 LRG-galaxy weak lensing

Correlating the positions of LRGs with shapes of background galaxies, the so-called LRG-galaxy weak lensing, is a powerful means of probing the average dark matter distribution around the LRGs (Mandelbaum et al. 2006a, 2012). The LRG-galaxy lensing measures the radial profile of differential surface mass density defined as

$$\Delta\Sigma(R) = \bar{\Sigma}(< R) - \Sigma(R). \quad (5.3)$$

The profile $\Sigma(R)$ is the average surface mass density around the LRGs defined as

$$\Sigma(R) = \bar{\rho}_{m0} \int d\pi [1 + \xi_{\text{gm}}(r = \sqrt{\pi^2 + R^2})], \quad (5.4)$$

where $\bar{\rho}_{m0}$ is the mean background mass density today, and $\xi_{\text{gm}}(r)$ is the three-dimensional cross-correlation between LRGs and the surrounding matter. In equation (5.3), $\bar{\Sigma}(< R)$ is the surface mass density averaged within a circular aperture of a radius R . Our use of the mean mass density today ($\bar{\rho}_{m0}$) is due to our use of the comoving units.

Figure 5.5 shows that the average mass profile measured for all LRGs in the mock catalog is in good agreement with the SDSS measurement in Mandelbaum et al. (2012). Note that, to obtain the average mass profile from our mock catalogs, we stacked all N -body particles around all the LRG-host subhalo in the simulations, including the particles outside dark matter halos. The lensing signal at the radii smaller than about $1 h^{-1}\text{Mpc}$ arises from the mass distribution within the same halo, while the signal at the larger scale arises from the mass distribution surrounding the host halos. These small- and large-scale signals are called the one- and two-halo terms, respectively (e.g. see Oguri & Takada 2011). The mock catalog well reproduces both the signals of different scales. The average halo mass inferred from the SDSS measurement and the halo model analysis is $\bar{M}_{\text{vir}} \simeq 4.1 \times 10^{13} h^{-1} M_{\odot}$ (Hikage et al. 2012a). The average mass in the mock catalog (Table 5.1) agrees with

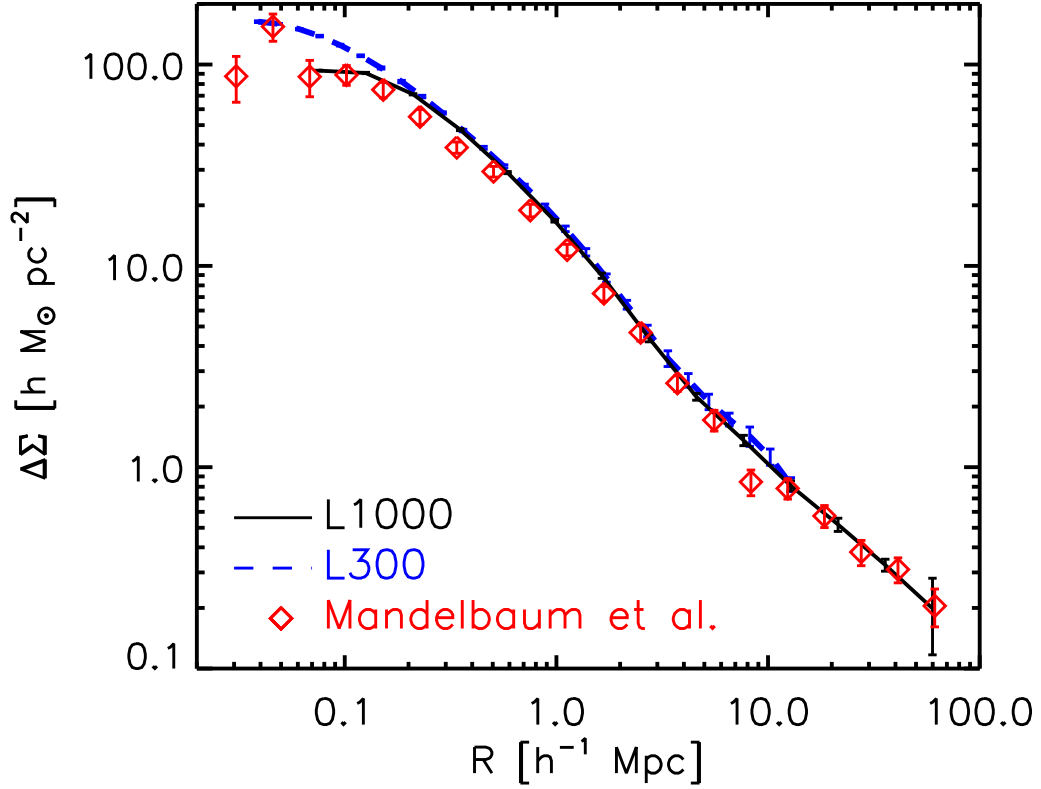


Figure 5.5: The average surface mass density profile around LRGs, which is an observable of the LRG-galaxy weak lensing. The solid and dashed curves are the results of our mock catalog, obtained by stacking N -body particles around all the LRG-host subhalos in the L1000 and L300 runs, respectively. The error bars are estimated using the measurements from 27 subsamples of LRG-host subhalos. The data with error bars show the SDSS measurements in Mandelbaum et al. (2012).

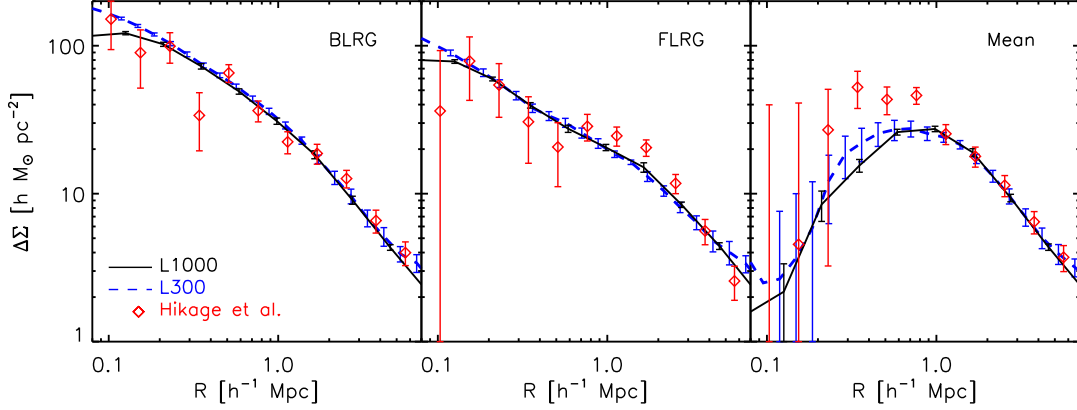


Figure 5.6: The average surface mass profiles for the multiple-LRG systems. The different panels show the results obtained by taking the different centers in each multiple-LRG halo; the brightest LRG (BLRG), the faintest LRG (FLRG) and the center-of-mass of different LRGs or the arithmetic mean positions of member LRGs (Mean) in the left, middle and right panels, respectively. The data with error bars show the SDSS measurements for the multiple-LRG systems in Hikage et al. (2012a).

the SDSS measurement within about 30% accuracy.

Hikage et al. (2012a) also used the SDSS LRG catalog to study the weak lensing for the multiple-LRG systems. When making the lensing measurements, they used three different proxies for the halo center of each multiple-LRG system, the BLRG, FLRG and the arithmetic mean position of member LRGs (hereafter “Mean”). By comparing the lensing signals for the different centers, they constrained the average off-center profiles for satellite BLRGs and FLRGs in the parent halos, finding about $400 h^{-1}\text{kpc}$ for a typical offset radius. Figure 5.6 shows that the mock catalog predictions are in remarkably good agreement with the SDSS measurements for the different centers. Since these lensing signals are from the same sample parent halos of the multiple-LRG systems, the differences between the signals of the different centers arise from the off-centering effects of the different centers. As nicely shown in Hikage et al. (2012a), the lensing signals for the BLRG and FLRG centers can be well explained by a mixture of the central and satellite LRGs in the sample (see Table 5.1 and Figure 5.8). The lensing signals for the FLRG center have smaller amplitudes due to the larger dilution effect because of a larger fraction of satellite (off-centered) FLRGs than in the BLRG centers. On the other hand, the Mean center does not have any galaxy (subhalo) at its position, and therefore the Mean center always has an off-centering effect from the true center in each LRG system. This causes decreasing powers of the lensing signal at the smaller radii than the typical off-center radius. The lensing signals at some radii for the FLRG and Mean centers show some discrepancy from the mock catalog, but we do not think that the disagreement is significant. The average masses inferred from the SDSS measurement and the mock

catalog (Table 5.1) for the multiple-LRG halos agree within about 30%; $\bar{M}_{\text{vir}} \simeq 1.36$ or $1.52 \times 10^{14} h^{-1} M_{\odot}$, respectively.

As can be shown in Figures 5.4, 5.5 and 5.6, our mock catalog of LRGs well reproduces both the SDSS measurements for the auto-correlation function of LRGs and the LRG-galaxy weak lensing simultaneously. As recently discussed in Neistein & Khochfar (2012) (also see Neistein et al. 2011), the abundance matching method has a difficulty to reproduce these measurements with the same model, although they considered the spectroscopic sample of SDSS galaxies, rather than focused on LRGs. Thus the agreements of our mock catalog show a capability of our method to predict different statistical quantities of LRGs by self-consistently modeling, rather than assuming, the fractions of satellite LRGs among different halos and the radial distribution of satellite LRGs in the host halos (also see chapter 4 for a recent development on the extended abundance matching method based on the similar motivation).

5.4 Properties of satellite LRGs and the FoG effect

One motivation in this chapter is to understand the physics of the non-linear redshift-space distortion, i.e. the FoG effect, in the redshift-space power spectrum of LRGs. The FoG effect is caused by internal motion of satellite LRG(s) in LRG-host halos (Hikage et al. 2012b,a). In the following, we study several quantities relevant for the FoG effect; the fraction of satellite LRGs, the radial profile of satellite LRGs inside the parent halos and the internal velocities of satellite LRGs (see Hikage et al. 2012b, for details of the theoretical modeling).

Figure 5.7 shows how much fraction of LRG-host halos that host *satellite* LRG(s) inside at $z = 0.3$, as a function of the halo mass. Note that we include the single-LRG systems, which host one LRG as a *satellite* galaxy, in addition to the multiple LRG systems. The error bars around the solid curve are Poisson errors, estimated using the number of halos in each mass bin. The figure shows that more massive halos have a higher probability to host satellite LRG(s). About 20 % of parent halos with $M_{\text{vir}} \simeq 10^{14} h^{-1} M_{\odot}$ host satellite LRG(s).

We naively expect that a BLRG, the most massive LRG-progenitor halo at $z = 2$ among LRG-progenitor halo(s) in the same LRG-host halo at $z = 0.3$, becomes a central galaxy in a host halo. The solid curves in Figure 5.8 show the fraction of BLRGs for becoming a satellite galaxy in LRG-host halos at $z = 0.3$ as a function of the halo mass, computed using all the LRG-host halos. For parent halos with $M_{\text{vir}} \gtrsim 10^{14} h^{-1} M_{\odot}$, there is up to 10 % probability for its BLRG to be a satellite galaxy.

The dashed curves are the similar fraction, but computed using only the multiple LRG systems. This sample is intended to compare with the recent result in Hikage

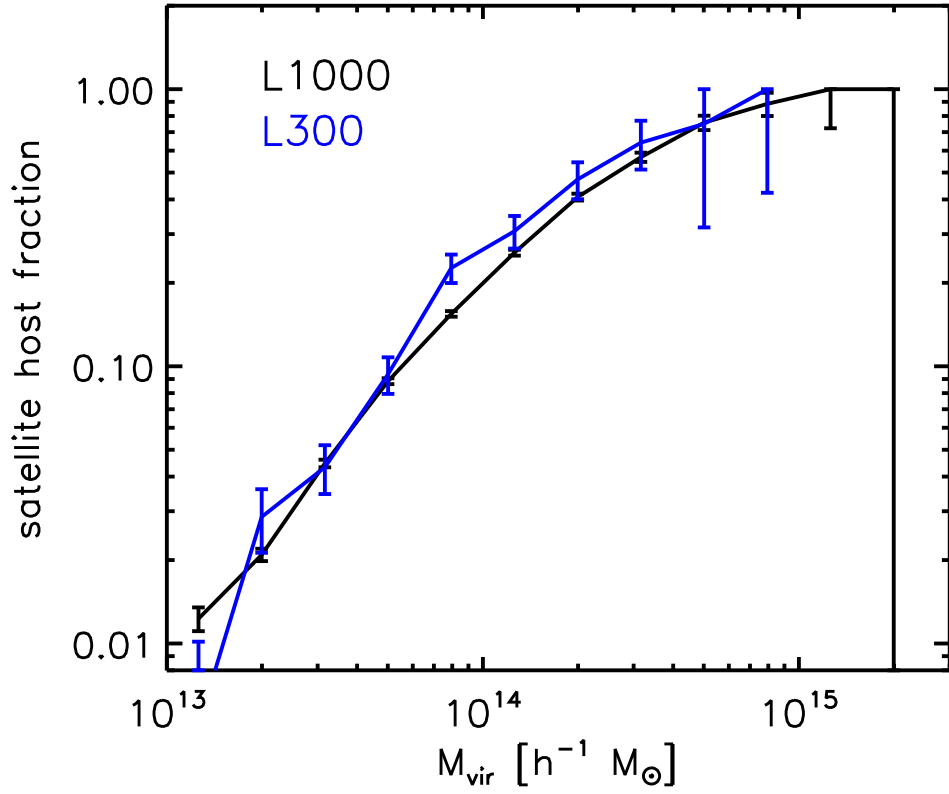


Figure 5.7: The fraction of halos hosting *satellite* LRG(s) inside as a function of halo mass, computed by using all the LRG-host halos at $z = 0.3$ in the L1000 and L300 runs.

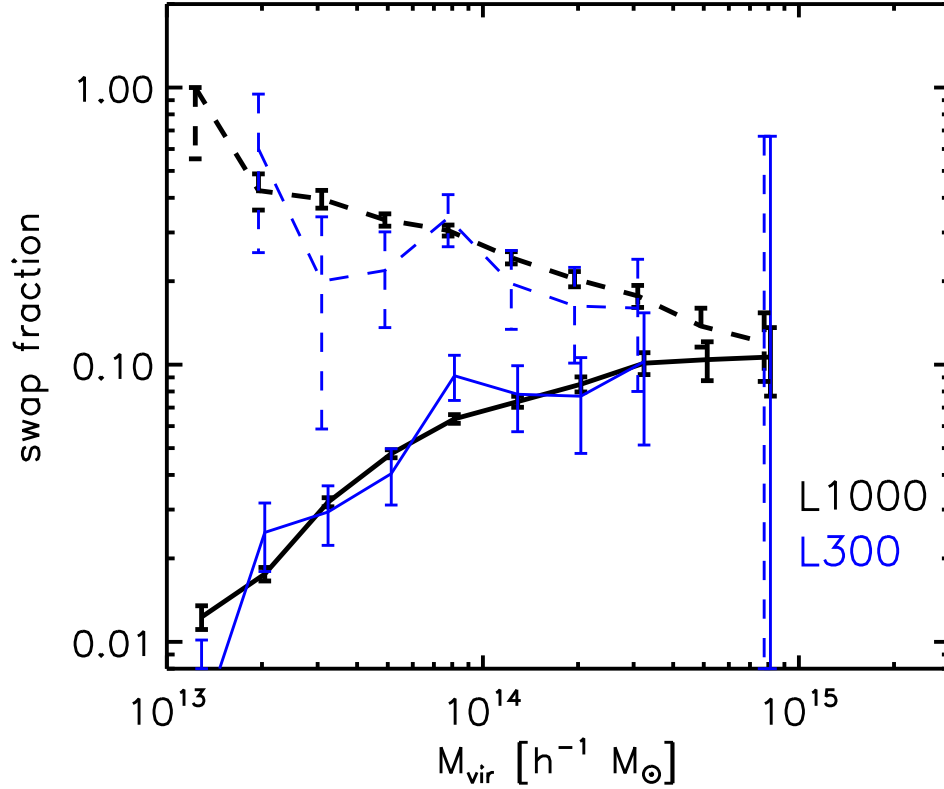


Figure 5.8: The solid curves show the fraction of the parent halos hosting the brightest LRG (BLRG) as a *satellite* galaxy, among all the LRG-host halos. The dashed curves are the similar fraction of LRG-host halos with satellite BLRG, but computed using only the multiple-LRG systems. The error bars are computed from the number of halos in each mass bin assuming Poisson statistics.

et al. (2012a) (see below). In this case, the fraction of satellite BLRGs is higher for host halos with smaller masses, with larger error bars. This can be explained as follows. Most of low-mass host-halos with masses $\lesssim 10^{14} h^{-1} M_{\odot}$ are single-LRG systems as can be found from Figure 5.3, and only a small number of halos are multiple-LRG systems, causing larger Poisson error bars at each mass bin. We have found from the simulation outputs that such low-mass halos of multiple LRG systems (mostly the systems with 2 LRGs) tend to display a bimodal mass distribution due to ongoing or past major merger, where the BLRG and other (mostly central) LRG tend to have the small mass difference. As a result, such low-mass multiple-LRG systems have a higher chance to host the BLRG as a satellite LRG. On the other hand, the fraction of halos with satellite BLRG converge to the solid curve with increasing the host-halo mass, because most of such massive halos are multiple-LRG systems. For multiple LRG systems with mass of $M_{\text{vir}} \simeq 10^{14} h^{-1} M_{\odot}$, about 30% of BLRGs are satellite galaxies.

Recently, Hikage et al. (2012a) studied the multiple-LRG systems defined from the SDSS DR7 catalog by applying the CiC technique as well as the FoF group finder method to the distribution of LRGs in redshift space. Then they used the different correlation measurements, the redshift-space power spectrum, the LRG-galaxy lensing and the cross-correlation of LRGs with photometric galaxies, to study properties of satellite LRGs. They found that the multiple-LRG systems has a typical halo mass of $M_{180b} \simeq 1.6 \times 10^{14} h^{-1} M_{\odot}$ (with a roughly 10 % statistical error), and that about 40 % of BLRGs in the multiple-LRG systems appear to be satellite galaxies¹¹. Using the method in Appendix C in Hu & Kravtsov (2003), we find $M_{\text{vir}} \simeq 0.85 M_{180b}$ assuming an NFW profile with concentration parameter $c = 4$. The weak lensing for the SDSS multiple-LRG systems implies $M_{\text{vir}} = 1.4 \times 10^{14} h^{-1} M_{\odot}$ from $M_{180b} = 1.6 \times 10^{14} h^{-1} M_{\odot}$. Our mock catalog shows a fairly good agreement with the SDSS results, for the average halo mass and the fraction of satellite BLRGs (also see Table 5.1).

In Figure 5.9, we study the average radial profile of satellite LRGs. In this calculation, we employ only the parent halos containing satellite LRG(s), and estimate the radial profile by stacking the radial distribution of satellite LRG(s) in units of the radius relative to the virial radius of each halo. We use the mass peak of the smooth component as the halo center. The average profile p_{off} is normalized as

$$\int dr' 4\pi r'^2 p_{\text{off}}(r') = 1, \quad \text{with } r' = r_{\text{off}}/R_{\text{vir}}, \quad (5.5)$$

where r_{off} is the distance from the density maximum of the smooth component. The average mass of the host halos is $M_{\text{vir}} \simeq 1.31 \times 10^{14}$ or $1.24 \times 10^{14} h^{-1} M_{\odot}$ for the L1000 or L300 run, respectively, while the average virial radius $R_{\text{vir}} \simeq 1.07$ or

¹¹Note that Hikage et al. (2012a) used the halo mass definition of M_{180b} , which is different from the virial mass M_{vir} and defined by the enclosed mass inside which the mean density is 180 times the mean background mass density.

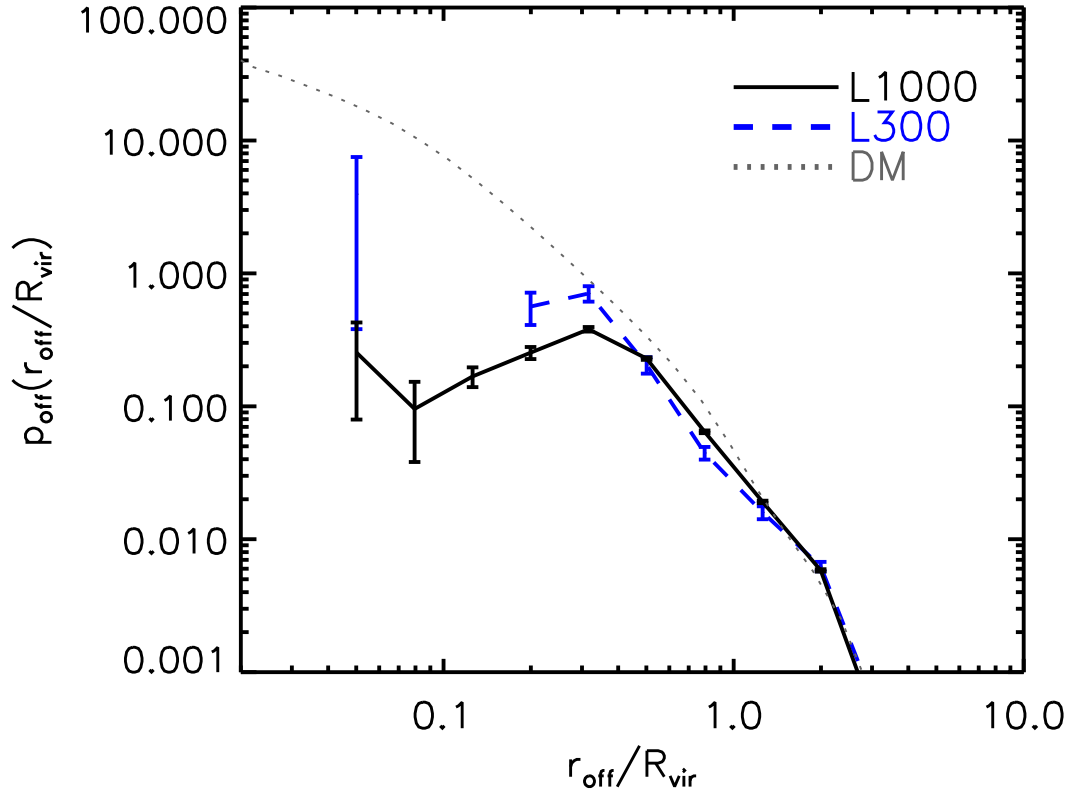


Figure 5.9: The average radial profile of satellite LRG host subhalos, obtained by stacking the positions of satellite LRGs in all the LRG-host halos with satellite LRG(s), as a function of radius relative to the virial radius of each parent halo. For comparison, the upper dotted curve shows the profile of dark matter averaged for the same host halos with an arbitrary amplitude. The error bars at each radial bin are estimated by first dividing LRG-host halos into 27 subsamples (27 subvolumes) and then computing variance of the number of satellite LRGs at the radial bin.

$1.06 h^{-1}\text{Mpc}$ in the comoving unit. Compared to the dark matter profile, the radial profile of satellite LRGs clearly displays a flattened profile. The typical off-center radius, where the profile starts to be flattened, is found to be about $400 h^{-1}\text{kpc}$ as $R_{\text{vir}} \simeq 1 h^{-1}\text{Mpc}$, which is in a good agreement with the result in Hikage et al. (2012a). The radial profile also shows a decline at the smaller radii. Thus our result clearly shows a violation of the assumption often used in a standard HOD method that the radial profile of member galaxies follows the dark matter profile. However, note that the L300 run shows no satellite LRG at small radii $r_{\text{off}}/R_{\text{vir}} \leq 0.1$, except in the innermost bin. Thus the satellite LRGs at the small radii are mainly from most massive host-halos, which do not exist in the smaller box simulation, L300. Although the mock catalogs show a sharp rise at the innermost bin $r_{\text{off}}/R_{\text{vir}} \simeq 0.06$ ($\sim 60 h^{-1}\text{kpc}$), which may indicate merging LRGs to the central subhalo in the less massive halos, the scatters are large even for the L300 run, so the result is not significant. Nevertheless, it is worth mentioning that the satellite LRG distribution in our mock catalog seems to show a similar profile to the profile of most massive subhalos in cluster-scale halos in Gao et al. (2012) (see there Figures 15 and 16 for the profile). These features in the radial profile of massive subhalos may be as a result of dynamical friction, tidal stripping and merger to the central galaxy. However, this needs a further careful study to derive a more robust conclusion, by using high-resolution simulations as well as a larger number of the realizations.

Figure 5.10 shows the average radial profile of internal motions of satellite LRGs in the parent halos, where the bulk motion of each parent halo (the average velocity of N -body particles belonging to the smooth component of the halo) is subtracted from the velocity of each LRG-host subhalo. We considered only the host halos with satellite LRG(s) as in Figure 5.9. The curves, labelled as $\langle v_{\text{off},r} \rangle$, are the average radial velocities for all the satellite LRGs with respect to the halo center. The average velocity is negative, reflecting the coherent infall motion towards the halo center, and the infall velocity is larger with increasing radius up to the virial radius. The average radial velocity becomes zero on average at the halo center. These support that the LRG-host subhalo approaches to the halo center due to dynamical friction. On the other hand, the curves labelled as $\sigma_{\text{off},r}$ are the average velocity dispersions of satellite LRGs. The velocity dispersion has greater amplitudes with decreasing the radius, reaching to $\sigma_{\text{off},r} \simeq 500 \text{ km s}^{-1}$. For comparison, the horizontal dotted line shows the average virial velocity dispersion, $\sigma_{\text{vir}} \equiv \sqrt{GM_{\text{vir}}/2R_{\text{vir}}} = 521 \text{ km s}^{-1}$, among the satellite LRG-host halos in the L1000 run. The combination of $\langle v_{\text{off},r} \rangle$ and $\sigma_{\text{off},r}$ implies that satellite LRGs gradually approach to the halo center due to dynamical friction and have an oscillating motion around the halo center. Again the amplitude of the velocity dispersion, $\sigma_{\text{off},r} \simeq 500 \text{ km s}^{-1}$, is in a nice agreement with the recent measurement in Hikage et al. (2012a), where they found the velocity dispersion of about 500 km s^{-1} for satellite LRGs in the multiple-LRG systems by combining the different correlation measurements from the SDSS DR7 LRGs.

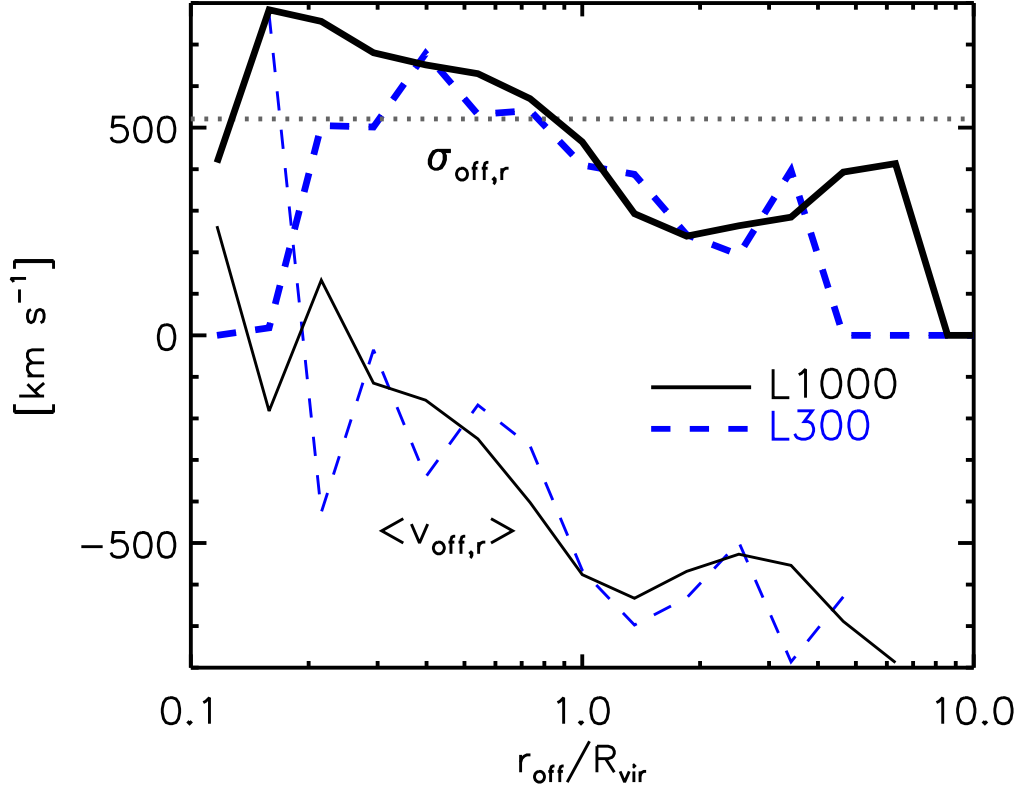


Figure 5.10: The average radial velocity of satellite LRGs, $\langle v_{\text{off},r} \rangle$, with respect to the halo center in each LRG-host halo, computed by using all the LRG-host halos with satellite LRG(s) as in the previous figure. The upper curves show the average radial velocity dispersion around the coherent infall, $\sigma_{\text{off},r}$. For the comparison, the dotted curve shows the average velocity dispersion expected from virial theorem, $\sigma_{\text{vir}} = \sqrt{GM_{\text{vir}}/2R_{\text{vir}}}$.

5.4.1 Redshift-space power spectrum of LRGs

Here we consider the redshift-space power spectrum of LRGs. The FoG effect due to internal motion of galaxies is one of systematic errors to complicate the cosmological interpretation of the measured power spectrum. The FoG effect involves complicated physics inherent in the evolution and assembly processes of galaxies, so is very difficult to accurately model from the first principles. The standard way to reduce the FoG contamination is to remove satellite galaxies from the region of each multiple-LRG system, and to keep only one galaxy (LRG in our case), ideally the central galaxy, because the central galaxy is supposed to be at rest with respect to the parent halo center and does not suffer from the FoG effect (see below for the related discussion). For example, Reid et al. (2010) developed a useful method for this purpose; first, reconstruct the distribution of halos from the measured distribution of LRGs by identifying multiple-LRG systems based on the CiC and FoF group finder method, and then keep only one LRG for each multiple-LRG system. However, the chosen LRG is not necessarily the central galaxy (more exactly, they used, as the halo center proxy, the arithmetic mean of member LRGs or the center-of-mass of different CiC groups without any luminosity or mass weighting), so there may generally remain a residual FoG contamination in the measured LRG power spectrum as pointed out in Hikage et al. (2012a).

In the top panel of Figure 5.11, we study the FoG effect on the redshift-space power spectrum, caused by the off-centering effect of LRGs in our mock catalog. Following the method in Reid et al. (2010) and Hikage et al. (2012a), we study the redshift-space power spectrum for halos that host LRG(s), instead of the power spectrum for LRGs. To compute the power spectrum of halos, we need to specify the halo center in each LRG-host halo. For single-LRG systems, we use the LRG position as the halo center proxy. For multiple-LRG systems, we employ different proxies of halo center for each system as done in Figure 5.6 for the LRG-galaxy lensing; BLRG, FLRG or the arithmetic mean (Mean), where the Mean center is computed in redshift space taking into account redshift space distortion due to peculiar velocities of LRG-host subhalos. The figure shows the angle-averaged redshift-space power spectra for the different centers, relative to the power spectrum for the mass center of each LRG-host halo (the mass center of N -body particles of the host halo). Note that, for the power spectrum measurement, we used the exactly same number of LRG-host halos, and the difference is only the positions of halo centers in the multiple-LRG systems. Hence, the difference between the different spectra should be from the off-centering effects in the multiple-LRG systems. Interestingly, the spectra for BLRG, FLRG and Mean centers all show smaller amplitudes with increasing wavenumber, as expected in the FoG effect. To be more precise, the power spectrum of FLRG center shows the strongest FoG effect, because a larger fraction of FLRGs are satellite galaxies than BLRGs (see Table 5.1). These results can be compared with Figure 2 in Hikage et al. (2012a). It can be found that the mock catalog qualitatively well reproduces the SDSS measurements: the spectra of BLRG and

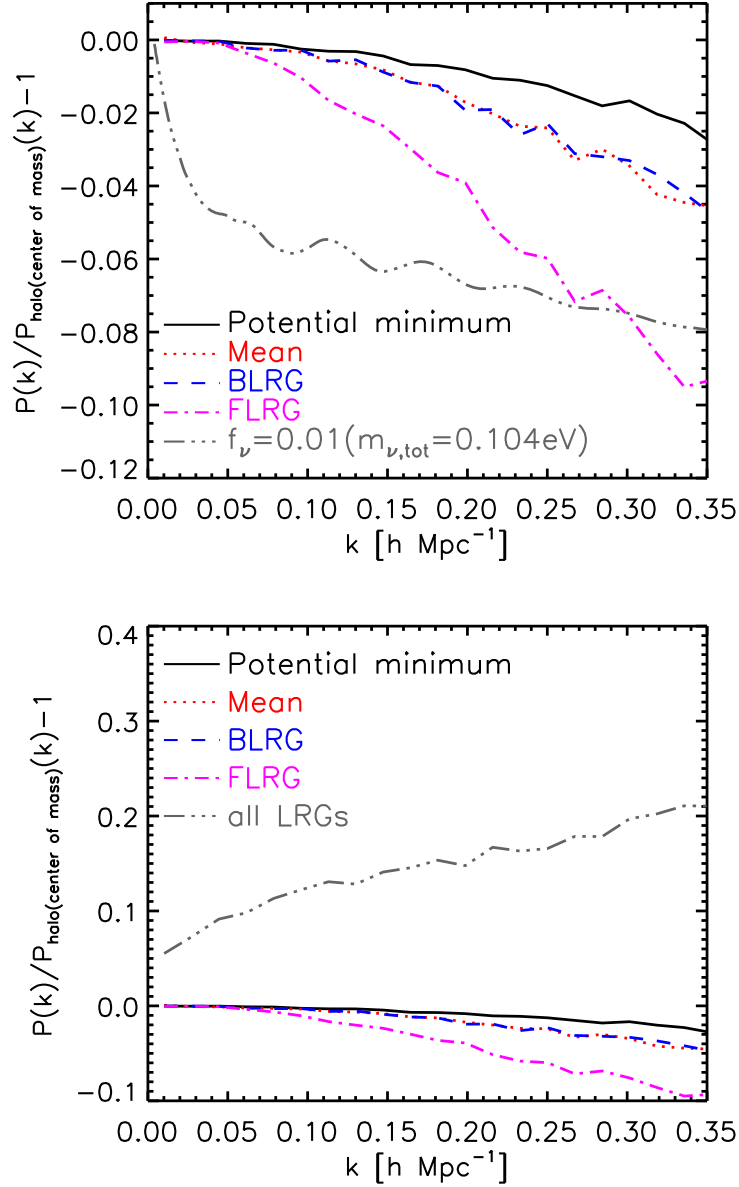


Figure 5.11: The angle-averaged redshift-space power spectra for the LRG-host halos at $z = 0.3$, computed from the L1000 run. The different curves show the fractional differences of the power spectra using different proxies of each LRG-host halo position in the power spectrum estimation, relative to the power spectrum for the mass center as the halo position. *Top panel:* The dotted, dashed and dot-dashed curves are the results when using different halo center proxies for each multiple-LRG system; the arithmetic mean position of the member LRGs in redshift space (Mean), BLRG or FLRG as in Figure 5.6. We also show the power spectrum measured using the potential minimum of each LRG-host halo by the solid line. For comparison, the three dots-dashed curve shows the effect caused by massive neutrinos assuming the total neutrino mass $m_{\nu, \text{tot}} = 0.104 \text{ eV}$. *Bottom panel:* Similar to the top panel, but the power spectrum using all the LRGs is added (the three dots-dashed curve). The shot noise contamination due to the different number densities of the LRG-host halos and the LRG-host subhalos is properly subtracted to have a fair comparison.

Mean centers are similar, and the spectrum for FLRG shows the stronger FoG suppression.

Figure 5.11 also shows the spectrum when taking the potential minimum as the center of each halo, where the potential minimum is the mass density peak of smooth component, i.e. the central subhalo position, in each LRG-host halo. This corresponds to the case that the power spectrum is measured by using the position of a central galaxy in each host halo. (BLRG is not necessarily a central galaxy as shown in Figure 5.8). The power spectrum for the potential minimum has a smaller amplitude than that of the mass center of host halo, implying that the potential minimum has a random motion around the mass center in each halo. Comparing the spectra for the potential minimum and the BLRG center shows that the BLRG spectrum has a smaller amplitude than the spectra for the potential minimum or the mass center by a few % in the fractional amplitude up to $k \simeq 0.3 h \text{ Mpc}^{-1}$. The few %-level FoG contamination would be okay for a current accuracy of the power spectrum measurement, but will need to be carefully taken into account for a higher-precision measurement of upcoming redshift surveys. For comparison, the three dots-dashed curve shows the effect on the power spectrum caused by massive neutrinos, where we assumed $m_{\nu, \text{tot}} \simeq 0.1 \text{ eV}$ for the total mass of neutrinos, close to the lower limit on the neutrino mass for the inverted mass hierarchy. For the normal mass hierarchy, the lower limit on the total mass is about 0.05 eV, and the amount of the suppression is about half of the result of 0.1 eV in Figure 5.11.

In the bottom panel of Figure 5.11, we also show the redshift-space power spectrum if using all the LRGs in the catalog. Note that we properly subtracted the shot noise contamination from the measured power spectra by using the number densities of LRGs or LRG-host halos. In this case, the power spectrum ratio shows greater amplitudes with increasing wavenumber rather than the FoG suppression. That is, the LRG power spectrum shows a greater clustering power or greater bias than in the LRG-host halo spectrum. The scales shown here, the scales greater than a few tens Mpc, are much larger than a virial radius of most massive host-halos and the one-halo term arising from clustering between two LRGs in the same host-halo should not be significant at these scales. Hence, the greater amplitudes in the LRG power spectrum would be due to a more weight on more massive halos, because satellite LRGs preferentially reside in more massive halos that have larger biases. Since the effect of different linear bias should cause only a scale-independent change in the power spectrum ratio, the change in the LRG power spectrum should be from a stronger nonlinear bias of such massive halos, even though the FoG suppression should be more significant for such halos. In fact, a combination of the perturbation theory of structure formation and halo bias model seems to reproduce such a non-trivial behavior in the power spectrum amplitudes (Nishizawa et al., in prep.). The results in the figure imply that including satellite LRGs in the power spectrum analysis complicates the interpretation of the measured power spectrum, thereby causing a bias in cosmological parameters.

In Figure 5.12, we study how the residual FoG effect varies with masses of LRG-host halos. To study this, we divide the LRG halos into two sub-samples by masses of the LRG-halos smaller and larger than the median, and measured the fractional power spectra for each sub-sample relative to the halo sample. As expected, the FoG effect is larger for the sub-sample containing more massive halos, because of the higher fraction of satellite BLRGs as well as the larger velocity dispersion (larger halo mass). The bottom panel shows the similar results, but obtained only by using the single-LRG halos. First of all, the single LRG systems have a smaller FoG effect, because of the smaller fraction of satellite BLRGs (Figure 5.8 and Table 5.1) as well as the smaller velocity dispersions for the lower-mass host-halos. Among the single-LRG halos, more massive halos have relatively a larger FoG contamination, but only by a few percent at $k \lesssim 0.35 \ h \text{ Mpc}^{-1}$ in the amplitude. Thus, the use of single-LRG systems may allow a cleaner interpretation of the measured power spectrum, yielding a more robust, unbiased constraint on cosmological parameters.

5.5 Discussion and conclusion

In this chapter, we developed a new abundance-matching based method to generate a mock catalog of the SDSS LRGs, using catalogs of halos and subhalos in N -body simulations. A brief summary of our method is as follows: (1) identify LRG-progenitor halos at $z = 2$ down to a certain mass threshold until the comoving number density of the halos become similar to that of the SDSS LRGs at $z = 0.3$ (2) trace the merging and assembly histories of the LRG “star particles”, the 30% of the halo member particles that lie closest to the center of each LRG-progenitor halo, and (3) at $z = 0.3$, identify the subhalos and halos hosting the LRG “star particles”. If a subhalo at $z = 0.3$ contains more than 50 % of the innermost particle of the progenitor halo, we assigned the halo at $z = 2$ and the subhalo at $z = 0.3$ as the LRG-progenitor halo and the LRG-host subhalo, respectively. We should emphasize that our method does not employ *any* free parameter to adjust in order for the model to match the measurements, once the mass threshold of the LRG-progenitor halos is determined to match the number density of SDSS LRGs. Thus, by assuming that a majority of stellar components of LRG is formed at $z = 2$, we can trace the assembly and merging histories of LRGs over a range of redshift, $z = [0.3, 2]$; for example, we can directly trace which LRGs become central or satellite galaxies in the LRG-host halos at $z = 0.3$. The novel aspect of our approach is that the abundance matching of halos to a particular type of galaxies (LRGs in this chapter) is done by connecting the halos and subhalos at different redshifts ($z = 2$ and $z = 0.3$ in our case), while the standard method is done for the same or similar redshift to the redshift of target galaxies. In addition, central and satellite subhalos are populated with galaxies under a single criterion: if a subhalo at $z = 0.3$ is a descendant of the $z=2$ -halos, the subhalo is included. The standard abundance matching uses different quantities for central and satellite subhalos.

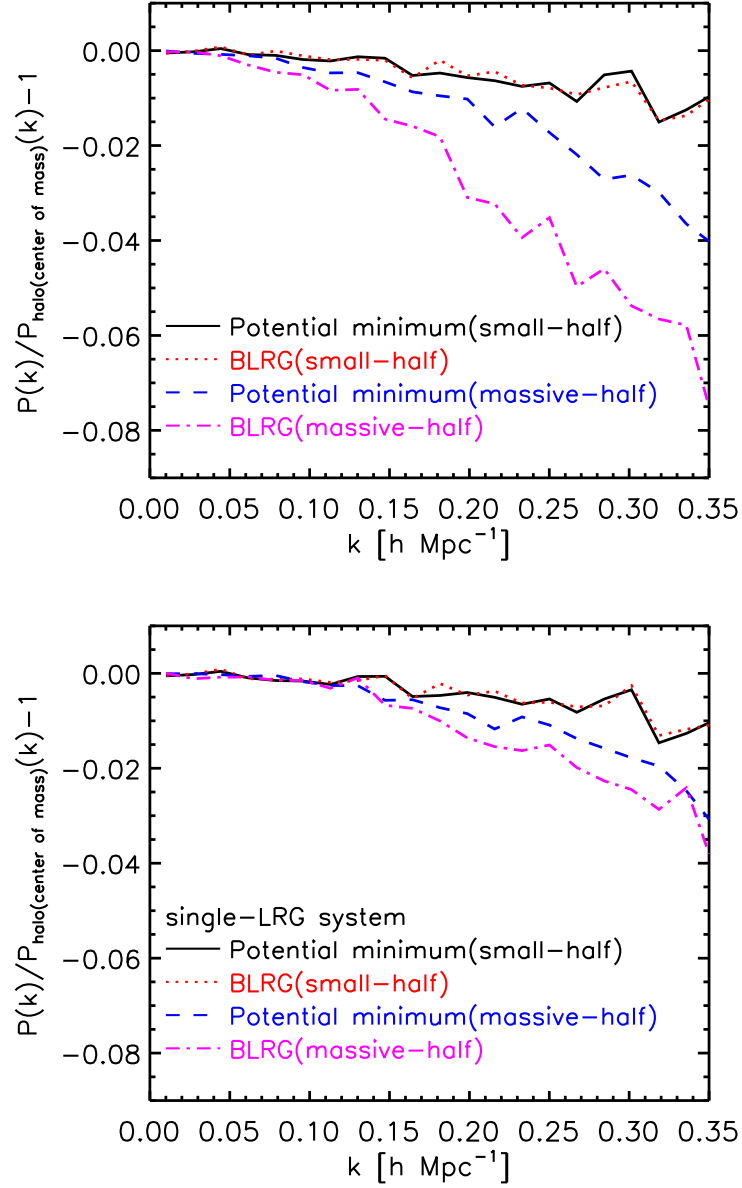


Figure 5.12: Similarly to the previous figure, but for the halved samples of LRG-host halos. *Top panel:* The LRG-halos are divided into two halved samples by the halo masses; one sub-sample is defined by halos which have masses smaller than the median mass (“small-half”), while the other is by halos with masses larger than the median (“massive-half”). The massive halo sub-sample shows a stronger FoG effect. *Bottom panel:* Similar plot, but using only the single-LRG halos.

Using the mock catalog, we computed various statistical quantities: the halo occupation distribution, the projected correlation function of LRGs, the mean surface mass density profile around LRGs (which is an observable of the LRG-galaxy weak lensing), and the redshift-space power spectrum of LRGs. We showed that the mock catalog predictions are in a good agreement with the measurements from the SDSS LRG catalog (Figures 5.4, 5.5 and 5.6). Thus our method seems to capture an essential feature of LRG formation in terms of a hierarchical structure formation scenario of Λ CDM model.

In the SDSS sample, only 6.4% of the halos contain multiple LRGs. In our simulation, 8% of the halos contain multiple LRGs. This modest deviation may be due to one of our many simple assumptions. First, we assumed that LRG progenitors are formed at a single epoch, $z = 2$. This is too simplified assumption, and a formation of LRGs should have some duration. Including some duration of formation of LRG-progenitor halos may improve the model predictions. Second, although LRGs are observationally selected by the well-designed magnitude and color cuts and not necessarily a mass-selected sample in terms of the stellar masses, our definition of the LRG-progenitor halos at $z = 2$ is solely based on their masses. The agreements between our mock catalog and the SDSS measurements support that the matching based on the LRG-progenitor halo masses seems fairly reasonable to mimic a population of LRGs. However, the model may be further refined by combining masses of the progenitor halos with other indicators when matching to LRGs. For instance, using the maximum circular velocity of each halo instead of its mass may improve the model accuracy. Third, we did not use satellite subhalos in the parent halo at $z = 2$ in making the abundance matching. We naively expect that subhalos at $z = 2$ merge into central subhalos from $z = 2$ to $z = 0.3$ due to dynamical friction, so we used the simplest method as the first attempt. However, including the subhalos at $z = 2$ for the abundance matching may improve an accuracy of the mock catalog. These would be worth exploring. Our mock catalog or more generally our abundance matching method offers several applications to measurements. First, Masjedi et al. (2008) showed that, by using the small-scale clustering signal and the pair counting statistics, LRGs are growing by about 1.7 % per Gyr, on average from merger activity from $z = 1$ to $z \sim 0.3$. Our method allows us to directly trace how each LRG-progenitor halo acquires the mass from other LRG-progenitor halos by major or minor mergers from $z = 2$ to $z = 0.3$. Hence, we can compare the prediction of our mock catalog with the measurement for the mass growth rate of LRGs. By using the constraint, we may be able to further improve the mock catalog.

Second, our method can predict how the distribution of LRG-progenitor evolves in relative to dark matter distribution as a function of redshift. Thus, our mock catalog can be used to predict various cross-correlations of LRG positions with other tracers of large-scale structure. As one such example, in this chapter, we studied the LRG-galaxy weak lensing measured via cross-correlation of LRGs with shapes of background galaxies, and showed a remarkably good agreement between our model

and the SDSS measurements. Another cross-correlation that has been studied in the literature is a cross-correlation of LRGs with a map of cosmic microwave background (CMB) anisotropies, which probes the stacked Sunyaev-Zel'dovich (SZ) effect (Hand et al. 2011; Sehgal et al. 2012) or the lensing effect on the CMB. Since every massive halos always host at least one LRG (100 % of halos with $M_{\text{vir}} \geq 2 \times 10^{14} h^{-1} M_{\odot}$ in our mock catalog), the cross-correlation is a powerful cross-check of the SZ signals. Our mock catalog can predict how the stacked SZ signals change for different catalogs of LRGs such as an inclusion of satellite LRGs and multiple-LRG systems, which may be able to resolve some tension between the observed LRG-CMB cross-correlation signal and the theoretical expectation (Sehgal et al. 2012).

Third is an application of our method to LRGs or massive red galaxies at higher redshift than $z = 0.3$. The SDSS-III BOSS survey is now carrying out an even more massive redshift survey of SDSS imaging galaxies. The magnitude and color cuts used for the BOSS survey are designed to efficiently select galaxies at $0.4 < z < 0.7$, and are different from the SDSS-I/II LRG selection. The BOSS galaxies are called the “constant mass” (CMASS) galaxies. The majority of CMASS galaxies are early-type galaxies, but are not exactly the same population as LRGs. In addition, the comoving number density of CMASS galaxies is higher than that of LRGs by a factor of 3. Hence, it would be interesting to apply the method developed in this chapter to the CMASS galaxies. Figure 5.1 shows an interesting indication of our mock catalog: more LRG-progenitor halos survive in the $z = 0.5$ output than at $z = 0.3$, because the halos do not have enough time to experience merging due to the shorter time duration from $z = 2$. Hence, our mock catalog naturally predicts a higher number density of LRG-progenitor halos at higher redshift than at $z = 0.3$, and may be able to match some of the BOSS galaxies without any fine tuning. Since the BOSS survey will provide us with a higher-precision clustering measurement and therefore has the potential to achieve tighter cosmological constraints, it is critically important to use an accurate mock catalog of the CMASS galaxies in order to remove or calibrate various systematic errors inherent in an unknown relation between the CMASS galaxies and dark matter. We hope that our method is useful for this purpose and can be used to attain the full potential of the BOSS survey or more generally upcoming redshift surveys for precision cosmology. This is our future study and will be presented elsewhere.

Chapter 6

Concluding Remarks

6.1 Summary

In this thesis, we studied the relations between observed galaxies and simulated dark matter structures through various aspects in the standard Λ -dominated cold dark matter (Λ CDM) cosmology.

In the first part of this thesis, we studied distributions of material around galaxies. In chapter 2, we explored the mass distribution around galaxies. We showed that cosmological N -body simulations well reproduce the average surface mass density profiles around galaxies measured through lensing magnification. We also showed that lensing measurements can be used to estimate the typical halo mass of sample galaxies. We decomposed the simulated mass profiles into two components, contributions from bound particles in the pseudo-virialized halos and from unbound particles. We found that unbound particles have substantial contributions to the lensing measurements. Motivated this finding, we explored the mass distribution beyond the virial radius to address the “missing dark matter problem”. We showed that the missed half of total matter is located in outer regions of halos. We also found that the mass structures beyond the virial radius is continuous from halos. It means that dark matter halos have no definite edges of the matter distributions.

In chapter 3, we studied the dust distribution around galaxies. We developed a simple formulation based on the halo model approach, and two halo-dust mass ratio models to predict the average surface dust density profiles around galaxies. We showed that the observed dust profile obtained through quasar reddening is well fitted by our models. From comparisons of the two-halo terms of the observed and model-predicted profiles, we also showed that the total amount of the intergalactic dust is estimated to be $\sim 10^{-6}$ in units of the critical density of the Universe. In the model, we employed a fitting parameter which denotes the extent of dust around galaxies. By fitting the model predictions to the observed profile, we found that dust extends up to a few times of the typical galactic halo virial radius, i.e., a few 100 kpc from galaxies.

In the latter part of this thesis, we developed methods to generate realistic mock

galaxy catalogs. In chapter 4, we extended the subhalo abundance matching method to develop a method to assign simulated subhalos with galaxy color in addition to galaxy luminosity. We discussed what subhalo property can be a physically suitable proxy for galaxy color. We ranked subhalos by such proxy property to divide subhalo catalogs into two groups, red and blue galaxy samples. Using simulation outputs directly, we calculated the projected correlation functions and the lensing profiles. We found that the model with the local mass density around subhalos, in which subhalos with higher (lower) local density host redder (bluer) galaxies, reproduces the observed color dependences of correlation functions and lensing measurements, simultaneously. Hence it is implied that local environment around galaxies are important for galaxy color. We found that, on the other hand, the model with the formation epoch of subhalos, in which older (younger) subhalos host redder (bluer) galaxies, reproduces the observed color-dependent correlation functions very well but not the lensing measurements. Therefore we argued that one needs to consider multiple measurements to test mock catalogs and to develop accurate methods.

In chapter 5, we developed a novel abundance matching method to construct mock catalogs of a particular population of galaxies, luminous red galaxies (LRGs). Motivated by observational suggestions, LRGs are passively-evolving, massive early-type galaxies with a typical age $\gtrsim 5\text{Gyr}$, we assumed that simulated most massive halos at $z = 2$ are the progenitors of LRGs at $z = 0.3$. Within cosmological N -body simulations, we tracked the fates of such progenitor halos at lower- z and defined their descendant subhalos at $z = 0.3$ as LRG-host subhalos where the abundance of LRG-host subhalos is matched to that of observed LRGs. We compared the model predictions with the observational results, the projected correlation function and the lensing measurements, to test our method. We showed that our method reproduces the observational results very well. Hence our method probably broadly correct to capture the nature of LRGs although the method can be refined further. We also studied the properties of satellite LRGs, which are hosted by satellite subhalos in their parent halos. Then we examined impacts of satellite LRGs on the redshift space power spectrum of LRG host halos which are found as suppression of power in the small scales. Our method can be used to remove or calibrate the systematic uncertainty induced by the Finger-of-God effect due to the internal motion of LRGs in their parent halos.

6.2 Future prospects

Here we would like to describe future prospects for cosmology from personal point of view. As shown throughout this thesis, the standard ΛCDM cosmology works very well to describe the formation of the large-scale structure of the Universe. The standard model has been constructed by various observations, e.g., the cosmic microwave background measurements, the supernovae surveys and the galaxy surveys, and theoretical interpretations for them. They have leaded us to the *precision cosmology*

era. In galaxy redshift surveys, however, the relationships between observed galaxies and simulated halos are still unclear. Inaccurate modeling of the relations should cause a bias in cosmological parameter estimations. The future galaxy surveys including the Subaru SuMIRe project will provide us with chances to construct more detailed picture of the Universe. To face more precise and even larger data from such upcoming projects and to make maximum use of their potential, galaxy-halo relationships *clearly* should be studied in more detail. Also, thanks to increasing computing power and the well-established cosmological model, today is suitable for cosmologists to carry out cosmological simulations to examine more accurate and physically-motivated galaxy-halo relation models. We expect that such successful models play a role of a bridge between theories and observations, and a key to push ourself to the next stage, the *accurate cosmology era* which should be more convincing.

We also expect that accurate modeling for galaxy-halo relations has large impacts on the galaxy evolution/formation studies. In principle, one can not *connect* individual galaxies at different epochs with galaxy redshift surveys data alone although galaxy evolution trends through the cosmic time can be inferred. As shown in chapters 4 and 5 in this thesis, it is now possible not only to assign multiple galactic properties with simulated (sub)halos but also to construct mock catalogs of a particular type of galaxies in physically-motivated ways. It means that one can create an universe of galaxy in computers. Thus one can easily study the evolution path of individual galaxies within cosmological simulations and ask interesting questions like, *what is the fate at $z = 0$ of a blue galaxy at $z = 1$?*

At the end of this thesis, we would like to hope that tensions between observations and theories are found in the near future although the current structure formation theory works well broadly to explain the observed universe. Because such problems are not only the driving force to brush up our understanding for the Universe but also fuel for cosmologists.

Acknowledgement

First of all, I am deeply grateful for Prof. Naoki Yoshida of the University of Tokyo. I am very lucky that I have been practically supervised for the past six years by Yoshida-san. I would like to thank him for his patience for long time and for providing me with various opportunities. He taught me a number of important things, from numerical techniques to how to deal with problems and to forward discussions. I never forget his every single word.

I would like to acknowledge my supervisor Prof. Naoshi Sugiyama for always encouraging me, especially. He made our cosmology group not only a homey but also a strict place. That is a nice situation for students. Thanks to Sugiyama-san, I spent really precious time at our group.

Very fortunately, I had chances to work with many collaborators, Prof. Masataka Fukugita, Prof. Chiaki Hikage, Prof. Yen-Ting Lin, Prof. Yoshiki Matsuoka, Prof. David N. Spergel and Prof. Masahiro Takada. I learned a lot from them. I would like to thank all of them very much and be proud of having worked with them.

Prof. Tsutomu T. Takeuchi of Ω -lab. kindly provided me with PC resources. I also acknowledge Takeuchi-san for reading this thesis very carefully and giving me a number of valuable suggestions. I enjoyed discussions with him.

I would like to thank Prof. Ryuichi Takahashi, Dr. Issha Kayo, Dr. Tomoaki Ishiyama, Dr. Takahiro Nishimichi, Dr. Ikkoh Shimizu and Mr. Ayuki Kamada for kindly providing me with N -body simulation data and analysis codes. These were very helpful for me.

I would like to acknowledge present and past faculty members and postdoctoral fellows of C-lab., Prof. Takahiko Matsubara, Prof. Kiyotomo Ichiki, Prof. Keitaro Takahashi, Prof. Kenji Kadota, Dr. Shuichiro Yokoyama, Dr. Daisuke Nitta and Dr. Toyokazu Sekiguchi. In our group seminars, they always asked me very critical questions and gave me valuable suggestions.

My friends at C-lab., Maresuke Shiraishi and Masanori Sato, always inspire me. I enjoyed my undergraduate and PhD days with them. I also thank all present and past members in astrophysics theory groups for fun time.

I have been supported by the Japan Society for the Promotion of Science fellowship program. Works in this thesis have been supported in part by Grant-in-Aid for Scientific Research on Priority Areas No. 467 “*Probing the Dark Energy through an Extremely Wide and Deep Survey with Subaru Telescope*”, and Grant-in-Aid for Nagoya University Global COE Program “*Quest for Fundamental Principles in the*

Universe: from Particles to the Solar System and the Cosmos”, from the Ministry of Education, Culture, Sports, Science and Technology of Japan. I also acknowledge the Kobayashi-Maskawa Institute for the Origin of Particles and the Universe, Nagoya University, for providing computing resources useful in conducting the researches reported in this thesis.

My vaunty family, Miyo, Hajime, Etsuko, Jiro, Keiko, Shingo, Mao, Yuta, Mami, Atsuro, Yuto and Charlie, has been providing me with emotional support. I also thank all friends in Nagoya, Nirayama, Kawazu and all over the world so much.

Finally, Maki-san, I thank you from the bottom of my heart. You always motivate me amazingly. I’m sure that I couldn’t go through my PhD days without you.

Bibliography

- Abazajian K. N. et al., *The Seventh Data Release of the Sloan Digital Sky Survey*, 2009, ApJS, 182, 543
- Aguirre A., Hernquist L., Katz N., Gardner J., Weinberg D., *Enrichment of the Intergalactic Medium by Radiation Pressure-driven Dust Efflux*, 2001, ApJ, 556, L11
- Allgood B. A., *Shapes and orientations of dark matter halos*, 2005, PhD thesis, University of California, Santa Cruz, California, USA
- Amblard A. et al., *Submillimetre galaxies reside in dark matter haloes with masses greater than 3×10^{11} solar masses*, 2011, Nature, 470, 510
- Anderson L. et al., *The clustering of galaxies in the SDSS-III Baryon Oscillation Spectroscopic Survey: Baryon Acoustic Oscillations in the Data Release 9 Spectroscopic Galaxy Sample*, 2012, ArXiv e-prints
- Balogh M. L., Baldry I. K., Nichol R., Miller C., Bower R., Glazebrook K., *The Bimodal Galaxy Color Distribution: Dependence on Luminosity and Environment*, 2004, ApJ, 615, L101
- Bamford S. P. et al., *Galaxy Zoo: the dependence of morphology and colour on environment*, 2009, MNRAS, 393, 1324
- Bartelmann M., Schneider P., *Weak gravitational lensing*, 2001, Physics Report, 340, 291
- Behroozi P. S., Conroy C., Wechsler R. H., *A Comprehensive Analysis of Uncertainties Affecting the Stellar Mass-Halo Mass Relation for $0 < z < 4$* , 2010, ApJ, 717, 379
- Bhattacharya S., Heitmann K., White M., Lukić Z., Wagner C., Habib S., *Mass Function Predictions Beyond Λ CDM*, 2011, ApJ, 732, 122
- Bianchi S., Ferrara A., *Intergalactic medium metal enrichment through dust sputtering*, 2005, MNRAS, 358, 379

- Blake C., Collister A., Lahav O., *Halo-model signatures from 380000 Sloan Digital Sky Survey luminous red galaxies with photometric redshifts*, 2008, MNRAS, 385, 1257
- Blake C., et al., *The WiggleZ Dark Energy Survey: the growth rate of cosmic structure since redshift $z=0.9$* , 2011, ArXiv e-prints
- Blanton M. R. et al., *The Luminosity Function of Galaxies in SDSS Commissioning Data*, 2001, AJ, 121, 2358
- Blanton M. R. et al., *The Galaxy Luminosity Function and Luminosity Density at Redshift $z = 0.1$* , 2003, ApJ, 592, 819
- Boylan-Kolchin M., Springel V., White S. D. M., Jenkins A., *There's no place like home? Statistics of Milky Way-mass dark matter haloes*, 2010, MNRAS, 406, 896
- Bryan G. L., Norman M. L., *Statistical Properties of X-Ray Clusters: Analytic and Numerical Comparisons*, 1998, ApJ, 495, 80
- Bullock J. S., Kolatt T. S., Sigad Y., Somerville R. S., Kravtsov A. V., Klypin A. A., Primack J. R., Dekel A., *Profiles of dark haloes: evolution, scatter and environment*, 2001, MNRAS, 321, 559
- Carson D. P., Nichol R. C., *The age-redshift relation for luminous red galaxies in the Sloan Digital Sky Survey*, 2010, MNRAS, 408, 213
- Chelouche D., Koester B. P., Bowen D. V., *The Dust Content of Galaxy Clusters*, 2007, ApJ, 671, L97
- Cole S., et al., *The 2dF Galaxy Redshift Survey: power-spectrum analysis of the final data set and cosmological implications*, 2005, ApJ, 362, 505
- Conroy C., Shapley A. E., Tinker J. L., Santos M. R., Lemson G., *The Varied Fates of $z \sim 2$ Star-forming Galaxies*, 2008, ApJ, 679, 1192
- Conroy C., Wechsler R. H., Kravtsov A. V., *Modeling Luminosity-dependent Galaxy Clustering through Cosmic Time*, 2006, ApJ, 647, 201
- Cooray A., *Halo model at its best: constraints on conditional luminosity functions from measured galaxy statistics*, 2006, MNRAS, 365, 842
- Cooray A., Sheth R., *Halo models of large scale structure*, 2002, Physics Report, 372, 1
- Coupon J. et al., *Galaxy clustering in the CFHTLS-Wide: the changing relationship between galaxies and haloes since $z \sim 1.2$* , 2012, A&A, 542, A5
- Crocce M., Fosalba P., Castander F. J., Gaztañaga E., *Simulating the Universe with MICE: the abundance of massive clusters*, 2010, MNRAS, 403, 1353

- Crocce M., Pueblas S., Scoccimarro R., *Transients from initial conditions in cosmological simulations*, 2006, MNRAS, 373, 369
- Croton D. J., Gao L., White S. D. M., *Halo assembly bias and its effects on galaxy clustering*, 2007, MNRAS, 374, 1303
- Davis M., Efstathiou G., Frenk C. S., White S. D. M., *The evolution of large-scale structure in a universe dominated by cold dark matter*, 1985, ApJ, 292, 371
- Davis M., Huchra J., *A survey of galaxy redshifts. III - The density field and the induced gravity field*, 1982, ApJ, 254, 437
- Dawson K. S. et al., *The Baryon Oscillation Spectroscopic Survey of SDSS-III*, 2012, ArXiv e-prints
- De Bernardis F., Cooray A., *A Conditional Luminosity Function Model of the Cosmic Far-Infrared Background Anisotropy Power Spectrum*, 2012, ArXiv e-prints
- de Lapparent V., Geller M. J., Huchra J. P., *A slice of the universe*, 1986, ApJ, 302, L1
- Duffy A. R., Schaye J., Kay S. T., Dalla Vecchia C., *Dark matter halo concentrations in the Wilkinson Microwave Anisotropy Probe year 5 cosmology*, 2008, MNRAS, 390, L64
- Eisenstein D. J. et al., *Spectroscopic Target Selection for the Sloan Digital Sky Survey: The Luminous Red Galaxy Sample*, 2001, AJ, 122, 2267
- Eisenstein D. J., Hu W., Tegmark M., *Cosmic Complementarity: Joint Parameter Estimation from Cosmic Microwave Background Experiments and Redshift Surveys*, 1999, ApJ, 518, 2
- Eisenstein D. J., et al., *Detection of the Baryon Acoustic Peak in the Large-Scale Correlation Function of SDSS Luminous Red Galaxies*, 2005, ApJ, 633, 560
- Ellis R. et al., *Extragalactic Science and Cosmology with the Subaru Prime Focus Spectrograph (PFS)*, 2012, ArXiv e-prints: arXiv:1206.0737
- Fukugita M., *Global amount of dust in the universe*, 2011, ArXiv e-prints
- Fukugita M., Peebles P. J. E., *The Cosmic Energy Inventory*, 2004, ApJ, 616, 643
- Gao L., Navarro J. F., Frenk C. S., Jenkins A., Springel V., White S. D. M., *The Phoenix Project: the dark side of rich Galaxy clusters*, 2012, MNRAS, 425, 2169
- Gao L., Springel V., White S. D. M., *The age dependence of halo clustering*, 2005, MNRAS, 363, L66

- Gao L., White S. D. M., *Assembly bias in the clustering of dark matter haloes*, 2007, MNRAS, 377, L5
- Gerke B. F., Wechsler R. H., Behroozi P. S., Cooper M. C., Yan R., Coil A. L., *Improved Mock Galaxy Catalogs for the DEEP2 Galaxy Redshift Survey from Subhalo Abundance and Environment Matching*, 2012, ArXiv e-prints
- Guo Q., White S., Li C., Boylan-Kolchin M., *How do galaxies populate dark matter haloes?*, 2010, MNRAS, 404, 1111
- Hamana T., Takada M., Yoshida N., *Searching for massive clusters in weak lensing surveys*, 2004, MNRAS, 350, 893
- Hand N. et al., *The Atacama Cosmology Telescope: Detection of Sunyaev-Zel'Dovich Decrement in Groups and Clusters Associated with Luminous Red Galaxies*, 2011, ApJ, 736, 39
- Hayashi E., White S. D. M., *Understanding the halo-mass and galaxy-mass cross-correlation functions*, 2008, MNRAS, 388, 2
- Hikage C., Mandelbaum R., Takada M., Spergel D. N., *Where are the Luminous Red Galaxies (LRGs)? Using correlation measurements and lensing to relate LRGs to dark matter halos*, 2012a, ArXiv e-prints
- Hikage C., Takada M., Spergel D. N., *Using galaxy-galaxy weak lensing measurements to correct the finger of God*, 2012b, MNRAS, 419, 3457
- Hogg D. W. et al., *The Dependence on Environment of the Color-Magnitude Relation of Galaxies*, 2004, ApJ, 601, L29
- Hopkins A. M., Beacom J. F., *On the Normalization of the Cosmic Star Formation History*, 2006, ApJ, 651, 142
- Hu W., Kravtsov A. V., *Sample Variance Considerations for Cluster Surveys*, 2003, ApJ, 584, 702
- Inoue A. K., Kamaya H., *Constraint on intergalactic dust from thermal history of intergalactic medium*, 2003, MNRAS, 341, L7
- Jenkins A., *Second-order Lagrangian perturbation theory initial conditions for resimulations*, 2010, MNRAS, 403, 1859
- Jenkins A., Frenk C. S., White S. D. M., Colberg J. M., Cole S., Evrard A. E., Couchman H. M. P., Yoshida N., *The mass function of dark matter haloes*, 2001, MNRAS, 321, 372
- Kauffmann G., *The age of elliptical galaxies and bulges in a merger model*, 1996, MNRAS, 281, 487

- Kirshner R. P., Oemler, Jr. A., Schechter P. L., Sackett P. A., *A survey of the Bootes void*, 1987, ApJ, 314, 493
- Komatsu E. et al., *Five-Year Wilkinson Microwave Anisotropy Probe Observations: Cosmological Interpretation*, 2009, ApJS, 180, 330
- Komatsu E. et al., *Seven-year Wilkinson Microwave Anisotropy Probe (WMAP) Observations: Cosmological Interpretation*, 2011, ApJS, 192, 18
- Kravtsov A. V., Berlind A. A., Wechsler R. H., Klypin A. A., Gottlöber S., Allgood B., Primack J. R., *The Dark Side of the Halo Occupation Distribution*, 2004, ApJ, 609, 35
- Lacerna I., Padilla N., *The nature of assembly bias - I. Clues from a Λ CDM cosmology*, 2011, MNRAS, 412, 1283
- Lacerna I., Padilla N., *The nature of assembly bias - II. Halo spin*, 2012, MNRAS, 426, L26
- Leauthaud A. et al., *New Constraints on the Evolution of the Stellar-to-dark Matter Connection: A Combined Analysis of Galaxy-Galaxy Lensing, Clustering, and Stellar Mass Functions from $z = 0.2$ to $z = 1$* , 2012, ApJ, 744, 159
- Lewis A., Challinor A., Lasenby A., *Efficient Computation of Cosmic Microwave Background Anisotropies in Closed Friedmann-Robertson-Walker Models*, 2000, ApJ, 538, 473
- Li C., Kauffmann G., Jing Y. P., White S. D. M., Börner G., Cheng F. Z., *The dependence of clustering on galaxy properties*, 2006, MNRAS, 368, 21
- Lukić Z., Heitmann K., Habib S., Bashinsky S., Ricker P. M., *The Halo Mass Function: High-Redshift Evolution and Universality*, 2007, ApJ, 671, 1160
- Mandelbaum R., Seljak U., Cool R. J., Blanton M., Hirata C. M., Brinkmann J., *Density profiles of galaxy groups and clusters from SDSS galaxy-galaxy weak lensing*, 2006a, MNRAS, 372, 758
- Mandelbaum R., Seljak U., Kauffmann G., Hirata C. M., Brinkmann J., *Galaxy halo masses and satellite fractions from galaxy-galaxy lensing in the Sloan Digital Sky Survey: stellar mass, luminosity, morphology and environment dependencies*, 2006b, MNRAS, 368, 715
- Mandelbaum R., Slosar A., Baldauf T., Seljak U., Hirata C. M., Nakajima R., Reyes R., Smith R. E., *Cosmological parameter constraints from galaxy-galaxy lensing and galaxy clustering with the SDSS DR7*, 2012, ArXiv e-prints

- Mandelbaum R., Tasitsiomi A., Seljak U., Kravtsov A. V., Wechsler R. H., *Galaxy-galaxy lensing: dissipationless simulations versus the halo model*, 2005, MNRAS, 362, 1451
- Masaki S., Fukugita M., Yoshida N., *Matter Distribution around Galaxies*, 2012a, ApJ, 746, 38
- Masaki S., Hikage C., Takada M., Spergel D. N., Sugiyama N., *Understanding the nature of luminous red galaxies (LRGs): Connecting LRGs to central and satellite subhalos*, 2012b, arXiv:1211.7077, submitted to MNRAS
- Masaki S., Lin Y.-T., Yoshida N., *Modeling color-dependent galaxy clustering in cosmological simulations*, 2012c, submitted to MNRAS
- Masaki S., Yoshida N., *Distribution of dust around galaxies: an analytic model*, 2012, MNRAS, 423, L117
- Masjedi M., Hogg D. W., Blanton M. R., *The Growth of Luminous Red Galaxies by Merging*, 2008, ApJ, 679, 260
- Masjedi M. et al., *Very Small Scale Clustering and Merger Rate of Luminous Red Galaxies*, 2006, ApJ, 644, 54
- Matsuoka Y., Masaki S., Kawara K., Sugiyama N., *Halo occupation distribution of massive galaxies since $z=1$* , 2011, MNRAS, 410, 548
- McGee S. L., Balogh M. L., *Dust accretion and destruction in galaxy groups and clusters*, 2010, MNRAS, 405, 2069
- McKay T. A. et al., *Galaxy Mass and Luminosity Scaling Laws Determined by Weak Gravitational Lensing*, 2001, ArXiv Astrophysics e-prints
- Ménard B., Hamana T., Bartelmann M., Yoshida N., *Improving the accuracy of cosmic magnification statistics*, 2003, A&A, 403, 817
- Ménard B., Kilbinger M., Scranton R., *On the impact of intergalactic dust on cosmology with Type Ia supernovae*, 2010a, MNRAS, 406, 1815
- Ménard B., Scranton R., Fukugita M., Richards G., *Measuring the galaxy-mass and galaxy-dust correlations through magnification and reddening*, 2010b, MNRAS, 405, 1025
- Miralda-Escude J., *Gravitational lensing by clusters of galaxies - Constraining the mass distribution*, 1991, ApJ, 370, 1
- Moore B., Ghigna S., Governato F., Lake G., Quinn T., Stadel J., Tozzi P., *Dark Matter Substructure within Galactic Halos*, 1999, ApJ, 524, L19

- Moster B. P., Somerville R. S., Maubetsch C., van den Bosch F. C., Macciò A. V., Naab T., Oser L., *Constraints on the Relationship between Stellar Mass and Halo Mass at Low and High Redshift*, 2010, ApJ, 710, 903
- Narayan R., Bartelmann M., *Lectures on Gravitational Lensing*, 1996, ArXiv Astrophysics e-prints
- Navarro J. F., Frenk C. S., White S. D. M., *A Universal Density Profile from Hierarchical Clustering*, 1997, ApJ, 490, 493
- Neistein E., Khochfar S., *Looking at the relation between haloes and galaxies under the lens*, 2012, ArXiv e-prints
- Neistein E., Li C., Khochfar S., Weinmann S. M., Shankar F., Boylan-Kolchin M., *A tale of two populations: the stellar mass of central and satellite galaxies*, 2011, MNRAS, 416, 1486
- Nishimichi T. et al., *Modeling Nonlinear Evolution of Baryon Acoustic Oscillations: Convergence Regime of N-body Simulations and Analytic Models*, 2009, PASJ, 61, 321
- Nuza S. E. et al., *The clustering of galaxies at $z \sim 0.5$ in the SDSS-III Data Release 9 BOSS-CMASS sample: a test for the Λ CDM cosmology*, 2012, ArXiv e-prints
- Oguri M., Takada M., *Combining cluster observables and stacked weak lensing to probe dark energy: Self-calibration of systematic uncertainties*, 2011, Phys. Rev. D, 83, 023008
- Peacock J. A., Smith R. E., *Halo occupation numbers and galaxy bias*, 2000, MNRAS, 318, 1144
- Peacock J. A., et al., *A measurement of the cosmological mass density from clustering in the 2dF Galaxy Redshift Survey*, 2001, Nature, 410, 169
- Percival W. J., et al., *Measuring the Matter Density Using Baryon Oscillations in the SDSS*, 2007, ApJ, 657, 51
- Press W. H., Schechter P., *Formation of Galaxies and Clusters of Galaxies by Self-Similar Gravitational Condensation*, 1974, ApJ, 187, 425
- Quadri R. F., Williams R. J., Lee K.-S., Franx M., van Dokkum P., Brammer G. B., *A Confirmation of the Strong Clustering of Distant Red Galaxies at $2 < z < 3$* , 2008, ApJ, 685, L1
- Reddick R. M., Wechsler R. H., Tinker J. L., Behroozi P. S., *The Connection between Galaxies and Dark Matter Structures in the Local Universe*, 2012, ArXiv e-prints

- Reed D. S., Governato F., Quinn T., Stadel J., Lake G., *The age dependence of galaxy clustering*, 2007, MNRAS, 378, 777
- Reid B. A., Spergel D. N., *Constraining the Luminous Red Galaxy Halo Occupation Distribution Using Counts-In-Cylinders*, 2009, ApJ, 698, 143
- Reid B. A., et al., *Cosmological constraints from the clustering of the Sloan Digital Sky Survey DR7*, 2010, ApJ, 404, 60
- Reyes R., Mandelbaum R., Seljak U., Baldauf T., Gunn J. E., Lombriser L., Smith R. E., *Confirmation of general relativity on large scales from weak lensing and galaxy velocities*, 2010, Nature, 464, 256
- Rodríguez-Puebla A., Drory N., Avila-Reese V., *The Stellar-Subhalo Mass Relation of Satellite Galaxies*, 2012, ApJ, 756, 2
- Ross A. J., Brunner R. J., *Halo-model analysis of the clustering of photometrically selected galaxies from SDSS*, 2009, MNRAS, 399, 878
- Saito S., Takada M., Taruya A., *Neutrino mass constraint from the Sloan Digital Sky Survey power spectrum of luminous red galaxies and perturbation theory*, 2011, Phys. Rev. D, 83, 043529
- Schlegel D. J., et al., *BigBOSS: The Ground-Based Stage IV Dark Energy Experiment*, 2009, ArXiv e-prints
- Scoccimarro R., *Transients from initial conditions: a perturbative analysis*, 1998, MNRAS, 299, 1097
- Scoccimarro R., Sheth R. K., Hui L., Jain B., *How Many Galaxies Fit in a Halo? Constraints on Galaxy Formation Efficiency from Spatial Clustering*, 2001, ApJ, 546, 20
- Sehgal N. et al., *The Atacama Cosmology Telescope: Relation Between Galaxy Cluster Optical Richness and Sunyaev-Zel'dovich Effect*, 2012, ArXiv e-prints
- Seljak U., *Analytic model for galaxy and dark matter clustering*, 2000, MNRAS, 318, 203
- Seo H.-J., Eisenstein D. J., Zehavi I., *Passive Evolution of Galaxy Clustering*, 2008, ApJ, 681, 998
- Sheldon E. S. et al., *The Galaxy-Mass Correlation Function Measured from Weak Lensing in the Sloan Digital Sky Survey*, 2004, AJ, 127, 2544
- Sheth R. K., Tormen G., *Large-scale bias and the peak background split*, 1999, MNRAS, 308, 119

- Silk J., Mamon G. A., *The current status of galaxy formation*, 2012, *Research in Astronomy and Astrophysics*, 12, 917
- Simon P., Hettterscheidt M., Wolf C., Meisenheimer K., Hildebrandt H., Schneider P., Schirmer M., Erben T., *Relative clustering and the joint halo occupation distribution of red sequence and blue-cloud galaxies in COMBO-17*, 2009, *MNRAS*, 398, 807
- Skibba R. A., Sheth R. K., *A halo model of galaxy colours and clustering in the Sloan Digital Sky Survey*, 2009, *MNRAS*, 392, 1080
- Springel V., *The cosmological simulation code GADGET-2*, 2005, *MNRAS*, 364, 1105
- Springel V. et al., *The Aquarius Project: the subhaloes of galactic haloes*, 2008, *MNRAS*, 391, 1685
- Springel V., White S. D. M., Tormen G., Kauffmann G., *Populating a cluster of galaxies - I. Results at $z=0$* , 2001a, *MNRAS*, 328, 726
- Springel V., Yoshida N., White S. D. M., *GADGET: a code for collisionless and gasdynamical cosmological simulations*, 2001b, *NewA*, 6, 79
- Takeuchi T. T., Buat V., Heinis S., Giovannoli E., Yuan F.-T., Iglesias-Páramo J., Murata K. L., Burgarella D., *Star formation and dust extinction properties of local galaxies from the AKARI-GALEX all-sky surveys . First results from the most secure multiband sample from the far-ultraviolet to the far-infrared*, 2010, *A&A*, 514, A4
- Tasitsiomi A., Kravtsov A. V., Wechsler R. H., Primack J. R., *Modeling Galaxy-Mass Correlations in Dissipationless Simulations*, 2004, *ApJ*, 614, 533
- Tegmark M., et al., *The Three-Dimensional Power Spectrum of Galaxies from the Sloan Digital Sky Survey*, 2004, *ApJ*, 606, 702
- Tinker J., Wetzel A., Conroy C., *Are Halo and Galaxy Formation Histories Correlated?*, 2011, *ArXiv e-prints*
- Tinker J. L., Conroy C., Norberg P., Patiri S. G., Weinberg D. H., Warren M. S., *Void Statistics in Large Galaxy Redshift Surveys: Does Halo Occupation of Field Galaxies Depend on Environment?*, 2008, *ApJ*, 686, 53
- Tinker J. L., Weinberg D. H., Zheng Z., Zehavi I., *On the Mass-to-Light Ratio of Large-Scale Structure*, 2005, *ApJ*, 631, 41
- Tojeiro R. et al., *The progenitors of present-day massive red galaxies up to $z \sim 0.7$ - finding passive galaxies using SDSS-I/II and SDSS-III*, 2012, *MNRAS*, 424, 136

- Trujillo-Gomez S., Klypin A., Primack J., Romanowsky A. J., *Galaxies in Λ CDM with Halo Abundance Matching: Luminosity-Velocity Relation, Baryonic Mass-Velocity Relation, Velocity Function, and Clustering*, 2011, ApJ, 742, 16
- van den Bosch F., More S., Cacciato M., Mo H., Yang X., *Cosmological Constraints from a Combination of Galaxy Clustering and Lensing – I. Theoretical Framework*, 2012, ArXiv e-prints
- van den Bosch F. C., Yang X., Mo H. J., *Linking early- and late-type galaxies to their dark matter haloes*, 2003, MNRAS, 340, 771
- Viero M. P. et al., *BLAST: Correlations in the Cosmic Far-Infrared Background at 250, 350, and 500 μ m Reveal Clustering of Star-forming Galaxies*, 2009, ApJ, 707, 1766
- Wake D. A. et al., *The 2df SDSS LRG and QSO survey: evolution of the luminosity function of luminous red galaxies to $z = 0.6$* , 2006, MNRAS, 372, 537
- Wake D. A. et al., *The 2dF-SDSS LRG and QSO Survey: evolution of the clustering of luminous red galaxies since $z = 0.6$* , 2008, MNRAS, 387, 1045
- Wake D. A. et al., *Galaxy Clustering in the NEWFIRM Medium Band Survey: The Relationship Between Stellar Mass and Dark Matter Halo Mass at $1 < z < 2$* , 2011, ApJ, 728, 46
- Wang Y., Spergel D. N., Strauss M. A., *Cosmology in the Next Millennium: Combining Microwave Anisotropy Probe and Sloan Digital Sky Survey Data to Constrain Inflationary Models*, 1999, ApJ, 510, 20
- Wechsler R. H., Bullock J. S., Primack J. R., Kravtsov A. V., Dekel A., *Concentrations of Dark Halos from Their Assembly Histories*, 2002, ApJ, 568, 52
- Wechsler R. H., Zentner A. R., Bullock J. S., Kravtsov A. V., Allgood B., *The Dependence of Halo Clustering on Halo Formation History, Concentration, and Occupation*, 2006, ApJ, 652, 71
- Wetzel A. R., White M., *What determines satellite galaxy disruption?*, 2010, MNRAS, 403, 1072
- White M. et al., *The Clustering of Massive Galaxies at $z \sim 0.5$ from the First Semester of BOSS Data*, 2011, ApJ, 728, 126
- York D. G. et al., *The Sloan Digital Sky Survey: Technical Summary*, 2000, AJ, 120, 1579
- Zehavi I. et al., *The Intermediate-Scale Clustering of Luminous Red Galaxies*, 2005, ApJ, 621, 22

- Zehavi I. et al., *Galaxy Clustering in the Completed SDSS Redshift Survey: The Dependence on Color and Luminosity*, 2011, ApJ, 736, 59
- Zel'dovich Y. B., *Gravitational instability: An approximate theory for large density perturbations.*, 1970, A&A, 5, 84
- Zheng Z. et al., *Theoretical Models of the Halo Occupation Distribution: Separating Central and Satellite Galaxies*, 2005, ApJ, 633, 791
- Zheng Z., Coil A. L., Zehavi I., *Galaxy Evolution from Halo Occupation Distribution Modeling of DEEP2 and SDSS Galaxy Clustering*, 2007, ApJ, 667, 760
- Zu Y., Weinberg D. H., Davé R., Fardal M., Katz N., Kereš D., Oppenheimer B. D., *Intergalactic dust extinction in hydrodynamic cosmological simulations*, 2011, MNRAS, 412, 1059